DISSERTATION

SUBMITTED TO THE

COMBINED FACULTIES FOR THE NATURAL SCIENCES AND FOR MATHEMATICS

OF THE RUPERTO-CAROLA UNIVERSITY OF HEIDELBERG, GERMANY

FOR THE DEGREE OF

DOCTOR OF NATURAL SCIENCES

PRESENTED BY

DIPLOM-PHYSIKER FRANCESCO PACE

BORN IN TURIN, ITALY

ORAL EXAMINATION: OCTOBER 31, 2007

ON THE DETECTION

OF

GALAXY CLUSTERS

REFEREES: PROF. DR. MATTHIAS BARTELMANN

PROF. DR. JOACHIM WAMBSGANß

Über den Nachweis von Galaxienhaufen

Zusammenfassung

In dieser Arbeit präsentieren wir eine Studie über statistische Eigenschaften von Galaxienhaufen, die wir mit verschiedenen Filtern in kosmologischen Simulationen detektiert haben. Als Signal wurde sowohl die Scherung, hervorgerufen durch den schwachen Gravitationslinseneffekt, benutzt, als auch simulierte Beobachtungen des Sunyaev-Zel'dovich-Effektes (SZ) und von Röntgenemmissionen.

Wir testeten verschiedene Filter zur Verwendung mit dem schwachen Gravitationslinseneffekt und untersuchten ihre Leistung mit Hilfe von simulierten Scherungskarten, auf denen die Positionen der Halos genau bekannt waren. Wir entdeckten, dass großräumige Strukturen eine wichtige Kontaminationsquelle darstellen. Dies ist insbesondere der Fall für räumlich tiefe Beobachtungen. Wir sind überzeugt, dass sie die Quelle für viele Scherungsmaxima sein können, die keine Entsprechung im optischen oder Röntgenbereich haben. Wir bestätigten, dass Filter, die dazu konstruiert sind, um große räumliche Strukturen zu unterdrücken, ein besseres Ergebnis erzielen.

Wir untersuchten die statistischen Eigenschaften von SZ- und Röntgendetektionen und ihre Korrelationen. Zu diesem Zweck verwendeten wir eine kosmologische hydrodynamische Simulation. Wir stellten fest, dass SZ-Multibandfilter die Vollständigkeit von Detektionen verbessern und den Grad an Kontamination, verglichen mit Einzelbandfiltern, deutlich verringern. Röntgenkataloge sind im Vergleich zu SZ-Katalogen vollständiger, und die korrelierten Detektionen zeigen Eigenschaften, die ähnlich denen der Multibandbeobachtungen sind.

On the Detection of Galaxy Clusters

Abstract

In this Thesis we present the study of statistical properties of galaxy clusters detected via filtering techniques in cosmological simulations, using lensing shear maps or Sunyaev-Zel'dovich (SZ) and X-ray simulated observations.

We tested different weak-lensing filters and studied their performance on simulated shear maps where the positions of the halos were known precisely. We found that large-scale structures are an important contaminant to be taken into account especially for deep surveys. We suggest that they can be the origin of many shear peaks that do not have an optical or X-ray counterpart. We confirmed that filters constructing to suppress large scale structures (LSS) contribution perform better.

We studied the statistical properties of SZ and X-ray detections in maps simulating observations and the correlation between SZ and X-ray detections. To this purpose, we used a hydrodynamical cosmological simulation. We found that the SZ multi-band filter improves the completeness of the detections and decreases the contamination compared to the single-band filter. X-ray catalogues are more complete than SZ catalogues and the correlated detections show properties analogous to the multi-band filter detections.

I've seen things you people wouldn't believe.
Attack ships on fire off the shoulder of Orion.
I watched C-beams glitter in the dark near the Tannhauser gate.
All those moments will be lost in time, like tears in rain.
Time to die.

Blade Runner

Contents

List of Figures

List of Tables

Introduction

In the last few years observational techniques improved enormously allowing the scientific community to define a ”standard model” for cosmology: we live in a low density Friedmann universe whose evolution is now driven by a dark component that makes the expansion accelerate. The simplest hypothesis is that it is the cosmological constant (in other words the vacuum energy) or a scalar field, in analogy with the inflationary phase.

Indications in this sense come from observations and precise measurements of high-redshift supernova spectra (Perlmutter et al., 1999; Riess et al., 1998) and these predictions were spectacularly confirmed by the observations of the anisotropies in the CMB pattern (Spergel et al., 2007).

Owing to space-based telescopes, many new objects were observed at high-redshift and deep optical surveys provided the three-dimensional distribution of matter in the universe (Hawkins et al., 2003), either the luminous one (baryonic matter) or the dark matter component, detectable only via its gravitational effects. It is thus possible to measure correlations and mass functions.

A wealth of information on baryonic matter distribution comes from radio (SZ effect for example) and X-ray observations. Combining them permits astronomers to determine the density of the object observed and its content in terms of electron density.

Nevertheless, observations in a single band are not enough, as there is a strong degeneracy in the parameter space (see e.g. Tegmark et al., 2004), only combining different observations together it is possible to obtain reliable constraints on the cosmological parameters.

The most massive objects, and therefore the youngest ones according to the hierar-

chical model for structure formation, are galaxy clusters. They play an important role in cosmology, in particular for gravitational lensing. As they are very massive, they are likely to behave as *strong lenses* producing tangential and radial arcs, whose shape depends on the internal structure of the cluster. In this way it is possible to obtain information on the density profile or on the mass of the core regions. If the distances between the cluster and the sources are large, then we are in the *weak lensing* regime, whose main effect is to slightly distort the image of background sources. In this case, as the distortion is tiny, only a statistical study over many sources is possible.

Galaxy clusters are also a good indicator for the underlying cosmological model, as they form earlier in a low-density universe than in an high-density universe. Their evolution and characteristics depend also on the particular dark energy model considered: in particular they are more concentrated in an early dark energy (EDE) universe (see e.g. Bartelmann et al., 2006), where also in very early times the contribution of dark energy is not negligible but of the order of few percent (Wetterich, 2004; Doran & Robbers, 2006). This has the consequence for example of producing more gravitational arcs (Fedeli & Bartelmann, 2007).

Many authors showed that in weak-lensing surveys, several massive peaks in the shear field appear and it is not possible to identify them with optical or X counterparts (see e.g. Erben et al., 2000, 2003). A similar situation occurs for observations of the hydrogen 21-cm line, but the peaks correspond to halos with mass of the order of $10^{11}\ M_{\odot}/h$, much smaller than for the weak lensing case (Minchin et al., 2005). This is not surprising because the lensing signal, besides geometrical effects determined by the distances of the objects involved, depends on the mass of the lens. It is expected to observe through weak gravitational lensing only halos with mass at least $10^{13}\ M_{\odot}/h$.

The question whether these peaks originate from dark halos or LSS is of fundamental importance as with the growth of the fields observed an automatic analysis is required and it is important to know with which reliability they represent real structures to then use them for studies based on shear-selected clusters.

Previous studies (see e.g. Reblinsky & Bartelmann, 1999; White et al., 2002) showed that the LSS is an important contaminant for weak-lensing surveys and that it can affect weak-lensing mass determinations (Hoekstra, 2001). With the evolution of the techniques, this problem can be partially overcome using the benefits of tomography, where also redshift information are taken into account. This was shown to improve the reliability of the peaks observed.
Due to the enormous amount of data made available by present and future weak-lensing surveys, an automatic search for the structures in the field observed is strongly required. It is thus necessary to know what surveys are expected to find.

Nowadays, many observations are multiband, so it is possible to gain more information from the same object. This is also useful because from observing the same area of the sky in different bands it is possible to improve the identifications of objects. With the orbiting satellites that do not suffer from the influence of the atmosphere, it is possible to make deep observations to study distant objects. There is a rich literature on simulations of the SZ effect and many linear matched filters were developed to detect clusters using this effect. Simulations carried out to develop the filters reach a high level of realism and accuracy and are required for planning pipelines for satellites observations.
On the other hand, most of the studies on the detection of X-ray sources from simulations were based on idealized semi-analytical models for the gas physics involved. Also the angular distribution and abundance of the halos on the sky were based on analytical estimations.
Even if these kinds of studies prove to be really useful as it is possible to cover quite rapidly a very broad range in the parameter space, they are somehow too simplified and they do not take into account many elements that are possible to study in the framework of cosmological simulations. As several studies showed that halo properties are modified by the inclusion of baryonic physics, we performed a realistic simulation of the X-ray sky and of the SZ effect using a large hydrodynamical cosmological simulation where several phenomena related to gas physics were included.

This thesis is structured as follows. In Chapter 1 we introduce the basics concepts of cosmology that are important for the following discussion of weak lensing and dark energy models. As already said before, galaxy clusters are an important tool in modern cosmology and we therefore review theories about structure formation and evolution in Chapter 2. In Chapter 3 we briefly discuss properties of galaxy clusters, like density profiles and X-ray emission and SZ effect. All these aspects are important for the discussion on the detectability of clusters due to thermal emission.

In Chapter 4 we review the theory of gravitational lensing and we focus on those quantities, like gravitational potential, deflection angle, shear, effective convergence and flexion that will turn out to be useful for further discussions on several aspects connected to gravitational lensing.

In Chapter 5 we compare different lensing filters used in the literature to detect galaxy clusters out of shear maps using realistic raytracing simulation maps and afterwards we compare our results with observations currently done. The results are also published in Pace et al. (2007).

In Chapter 6 we study the detections of galaxy clusters combining a matched filter using X-rays emission and the SZ effect. We also compare the filter for the detection of X-ray sources with what it is found with real observations.

Finally in the appendix we briefly summarize the main characteristics of the different types of N-body algorithms and different interpolation schemes to assign particles on a regular grid.

Chapter 1

Cosmological background

In this chapter we review some basis of cosmology which are relevant for the following discussion on weak gravitational lensing and on dark energy models.
In section 1.1 we introduce the current cosmological model based on the cosmological principle and on the theory of general relativity which allow to derive the metric describing the space-time geometry and to define the concept of gravitational redshift (section1.2). Then we describe the dynamics of the evolution of the universe by means of Friedmann's equations in section 1.3 and the parameters (section 1.4) characterizing the cosmological models (section 1.5). Section 1.6 is devoted to the definition of distance in cosmology.
Finally, in section 1.7 we introduce models characterized by the presence of the cosmological constant and dark energy. They arise because from observational evidence the universe has a flat geometry, but radiation and matter are not enough to reach the density required from the theory, moreover according to supernova data, the expansion of the universe is accelerating and these two quantities are candidates to explain these phenomena.

1.1 The Robertson-Walker metric

The basic assumption of modern cosmology is that the universe is homogeneous and isotropic on large scales, i.e. on scales larger than the visible structures of galaxy distribution. This assumption goes under the name of *Cosmological principle*.

Evidence in this sense come from observations in several spectral bands (radio, infrared, optical and X-rays): they all show that the radiation sources are distributed uniformly. The most convincing proof of the homogeneity of the universe comes from the cosmic microwave background radiation (CMBR), a photon background with a temperature of $T = 2.726$ K (Mather et al., 1999) and fluctuations $\Delta T/T \simeq 10^{-5}$.

General relativity describes space-time properties by means of a 4×4 tensor (*metric tensor* $g_{\mu\nu}$) obtained solving the field equations. This tensor is used to write the line element

$$ds^2 = g_{\mu\nu} dx^\mu dx^\nu, \tag{1.1}$$

where dx represents the space-time coordinates. The index 0 refers to the time component, $x^0 = ct$, while the x^i, with $i = 1 \div 3$ are the space components. The convention on the summation over repeated indexes is used.

Because of the synchronization of clocks, $g_{00} = c^2$ where c is the speed of light and $g_{0i} = 0$ (from the isotropy condition), using spherical coordinates (r, θ, ϕ) the most general metric can then be written as

$$ds^2 = c^2 dt^2 - a(t)^2 \left[\frac{dr^2}{1 - Kr^2} + r^2 (d\theta^2 + sin^2\theta d\phi^2) \right], \tag{1.2}$$

where r is the radial coordinate and θ and ϕ are the angular variables, t the proper time of a comoving observer, $a(t)$ the scale factor which only depends on time, K the curvature parameter with dimension of the inverse of an area. K can be scaled in such a way that it assumes, according to the different geometries, only the values 1 (closed space with spherical geometry), 0 (flat space with euclidean geometry) or -1 (open space with hyperbolic geometry).

1.2 Redshift

If the universe expands or shrinks, then the scale factor $a(t)$ will change in time and the photons emitted by a source will be redshifted or blueshifted while they propagate towards the observer.

If we consider a source at comoving distance r emitting radiation with a wavelength λ_e and this radiation is observed with a wavelength λ_0, then the redshift z is defined as

$$z = \frac{\lambda_0 - \lambda_e}{\lambda_e}. \tag{1.3}$$

As photons travel along null geodesics, $ds^2 = 0$, then from Eq. 1.2:

$$\int_{t_e}^{t_0} \frac{c\,dt}{a(t)} = \int_0^r \frac{dr}{\sqrt{1-Kr^2}} = f(r), \tag{1.4}$$

$f(r)$ is constant in time because expressed in comoving coordinates, therefore the derivative of Eq. 1.4 brings to the following relation:

$$\frac{dt_0}{dt_e} = \frac{a(t_0)}{a(t_e)}. \tag{1.5}$$

In particular, if $dt_{e,0} = 1/\nu_{e,0}$, where ν_0 and ν_e represent the frequencies of the observed and of the emitted light, one can write

$$\left(\frac{\nu_0}{\nu_e}\right)^{-1} = \frac{a_e}{\lambda_e} = \frac{a_0}{\lambda_0}, \tag{1.6}$$

and the relation between the redshift and the scale factor is

$$1 + z = \frac{a_0}{a_e}. \tag{1.7}$$

1.3 Friedmann Equations

The metric tensor introduced in the previous section obeys the following Einstein's field equations:

$$G_{\mu\nu} = R_{\mu\nu} - \frac{1}{2}Rg_{\mu\nu} = \frac{8\pi G}{c^4}T_{\mu\nu} + \Lambda g_{\mu\nu}, \tag{1.8}$$

where $G_{\mu\nu}$ is the Einstein tensor, $R_{\mu\nu}$ and R are the Ricci tensor and the Ricci scalar, G the Newtonian gravitational constant, Λ the cosmological constant, a term introduced by Einstein to generalize his equations and to allow static solutions.

$T_{\mu\nu}$ is the stress-energy tensor and represents the source of the field. For a perfect fluid characterized by pressure $P(t)$, energy density $\rho(t)$ and four-velocity u(t), $T_{\mu\nu}$ reads as

$$T_{\mu\nu} = (P + \rho c^2) u_\mu u_\nu - P g_{\mu\nu}, \tag{1.9}$$

where the four-velocity is defined as $u_\mu = g_{\mu\nu} \frac{dx^\nu}{ds}$.

Using the metric 1.2, Einstein's equations 1.8 reduce to the following set of ordinary differential equations:

$$\left(\frac{\dot{a}}{a}\right)^2 = \frac{8\pi G}{3}\rho - \frac{Kc^2}{a^2} + \frac{\Lambda c^2}{3}\,, \tag{1.10}$$

$$\frac{\ddot{a}}{a} = -\frac{4\pi G}{3}\left(\rho + \frac{3P}{c^2}\right) + \frac{\Lambda c^2}{3} \tag{1.11}$$

These two equations go under the name of *Friedmann equations* (Friedmann, 1922, 1924); the scale factor is uniquely determined once an initial condition is specified. We choose $a(t_0) = 1$, where t_0 is the present epoch.

Friedmann's equations can be combined to yield the adiabatic equation stating energy conservation:

$$\frac{d}{dt}(a^3 \rho c^2) + P\frac{d}{dt}(a^3) = 0. \tag{1.12}$$

1.4 Cosmological parameters

A cosmological model is characterized by several parameters, in this section we describe the most relevant for the following discussion.

The relative expansion rate of the universe $H(t)$ is called *Hubble function* and it is defined as $H = \dot{a}/a$, its value at the present time, $H(t = t_0) \equiv H_0$ is the *Hubble constant*. As its value is not known precisely, usually the Hubble constant is parametrized as $H_0 = 100h$ km/s/Mpc. The most recent measurements, done by the *HST Key Project* team using Cepheids for calibration and secondary methods like supernovae and the Tully-Fisher relation give $h = 0.72 \pm 0.08$ (Freedman et al., 2001). The Hubble constant was

also inferred analyzing *WMAP* data ($h = 0.732^{+0.031}_{-0.032}$, see Spergel et al. (2007)) and from lensing ($h = 0.61 \div 0.65$, Fassnacht et al. (2002)) or with the SZ effect (Udomprasert et al. (2004) give a value of $h = 0.68^{+0.21}_{-0.14}$).

The Hubble parameter is very important because it allows to establish a distance scale $l_H = c/H_0 \approx 3000\ h^{-1}\ Mpc$, and a time scale for the expansion of the universe $t_H = 1/H_0 \approx 9.8\ h^{-1}\ Gyr$.

The density required to close the universe is called *critical density* and it is defined as

$$\rho_{cr,0} = \frac{3H_0^2}{8\pi G} \approx 2.7722 \times 10^{11}\ h^2 M_\odot / Mpc^3. \tag{1.13}$$

There are several contributions to the density of the universe: radiation, vacuum (for example the cosmological constant) and matter (either baryonic or non-baryonic). The density parameter of a given component i is defined as $\Omega_{i,0} = \rho_{i,0}/\rho_{cr,0}$.

In cosmology the *matter density parameter* $\Omega_{m,0} = \rho_{m,0}/\rho_{cr,0}$ is very important as we will see later. The density parameter for the cosmological constant is defined as $\Omega_{\Lambda,0} = \Lambda c^2/(3H_0^2)$, from this definition it is possible to derive an expression relating the density parameters to the spatial curvature:

$$H_0^2(1 - \Omega_{m,0} - \Omega_{\Lambda,0}) = -Kc^2, \tag{1.14}$$

if $K = 0$, the universe has a flat geometry and $\Omega_0 = \Omega_{m,0} + \Omega_{\Lambda,0} = 1$, K is positive or negative according to $\Omega_0 > 1$ or $\Omega_0 < 1$.

Another important parameter is the *deceleration parameter*, defined as:

$$q(t = t_0) \equiv q_0 = -\frac{\ddot{a}a}{\dot{a}^2}, \tag{1.15}$$

if $q > 0$ then the expansion rate of the universe is slowing down, otherwise it increases.

1.4.1 Parameter values

According to the most recent measurements, CMB in particular (Spergel et al., 2007), the geometry of the universe is flat, as is also expected from inflationary models. From

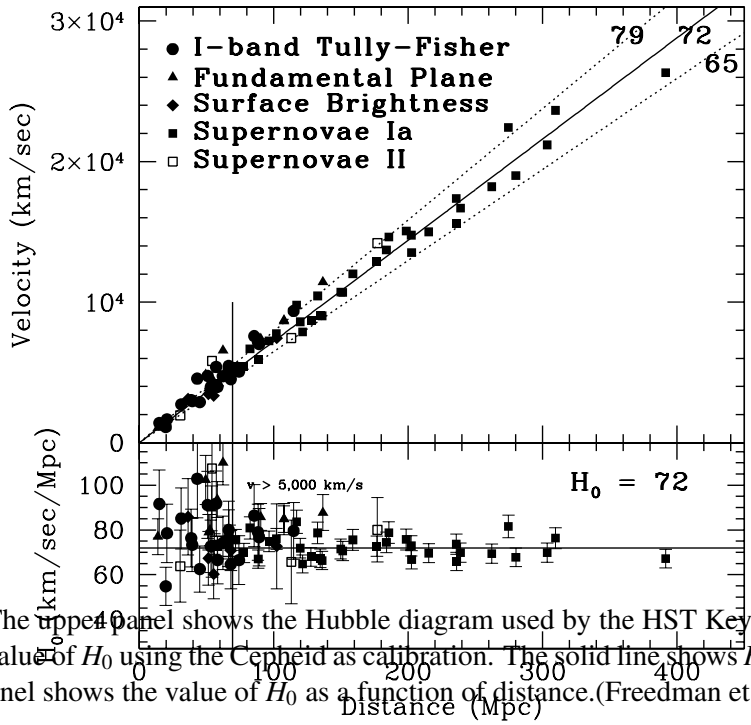

Figure 1.1: The upper panel shows the Hubble diagram used by the HST Key Project team to determine the value of H_0 using the Cepheid as calibration. The solid line shows $H_0 = 72\ km/s/Mpc$. The lower panel shows the value of H_0 as a function of distance.(Freedman et al., 2001)

primordial nucleosynthesis baryonic matter can account for $\Omega_b = 0.04$, while the total matter density (including baryonic and dark matter) is $\Omega_{m,0} \approx 0.3$. This implies that there should be another component covering the remaining 70% of the energy density of the universe, this additional component is parametrized as cosmological constant or as dark energy. We will discuss these models more in detail in section 1.7.

In table 1.1 we summarize the values of the cosmological parameters together with the values used in the following, unless otherwise stated.

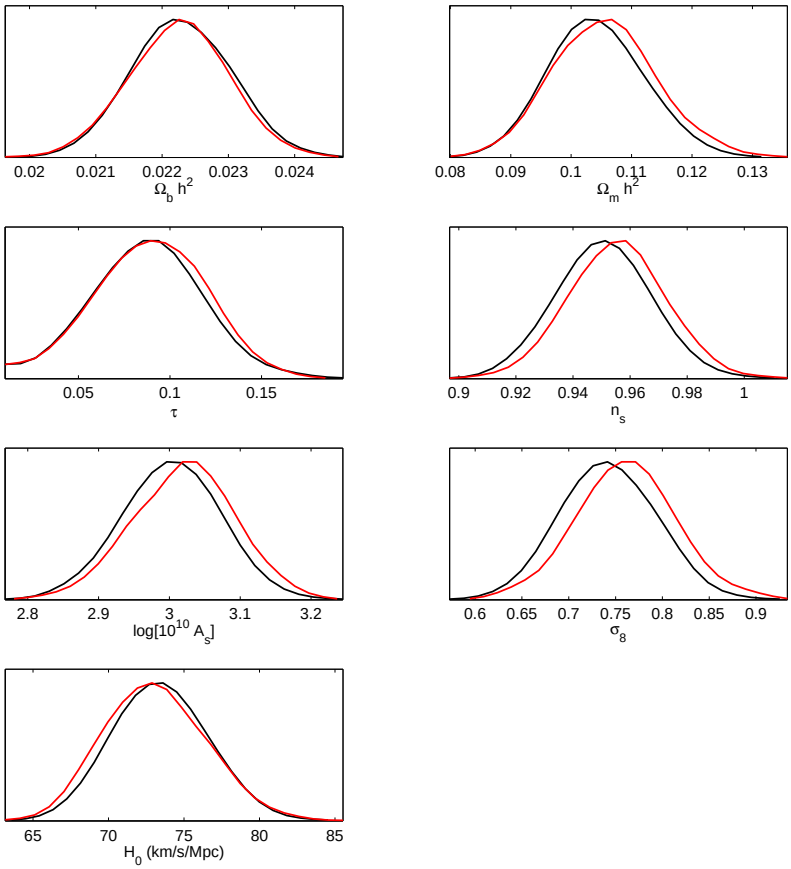

Figure 1.2: Marginalized likelihood functions for several cosmological parameters from three years of *WMAP* data. The red (black) curve is without (with) the SZ amplitude taken into account. The model is assumed to be spatially flat (Spergel et al., 2007).

1.5 Friedmann models

We now describe the cosmological models associated with equations 1.10 and 1.11. These models are based on the assumptions that the universe can be approximated as a perfect fluid with density ρ and pressure P and that these two quantities are related by the equation of state $P = w\rho c^2$ where w is a parameter (depending on time or not) characterizing the equation of state.

The use of a perfect fluid is justified by the fact that a real fluid can be considered as perfect in many situations of cosmological interest, for example if the collision length scale is much smaller than the physical scale of interest. It is also worth noting that the

Parameter	Symbol	Value	Determination	Used value
Hubble constant	h	0.73 ± 0.02 0.72 ± 0.08	WMAP3+2dFGRS HST Key Project	0.7
Matter density	$\Omega_{m,0}$	0.24 ± 0.02 0.26 ± 0.02	assuming $\Omega_K = 0$ free Ω_K	0.3
Cosmological constant	$\Omega_{\Lambda,0}$	0.76 ± 0.02 0.76 ± 0.02	assuming $\Omega_K = 0$ free Ω_K	0.7
Baryon density	$\Omega_{b,0}$	0.042 ± 0.002		0.042
Curvature	Ω_K	-0.09 ± 0.1	free Ω_K	0
Radiation density	$\Omega_{r,0}$	$(4.67 \pm 0.26) \cdot 10^{-5}$	CMB temperature	$2.494 \cdot 10^{-5}$

Table 1.1: Summary table with the measured and adopted values for the different cosmological parameters. The first column refers to the parameter, the second column the symbol used to indicate the parameter, the third column shows the measured value and the fourth column the method used to determine the given value. In the last column we report the adopted value.

form of the stress-energy tensor in equation 1.9 is necessary for compatibility with the cosmological principle.

To solve equation 1.12 it is necessary to specify the equation of state and thus finding the value of the parameter w. Normally it lies in the interval $0 \leq w \leq 1$, an exception are the cosmological constant or the dark energy, whose values are negative, in particular for a cosmological constant term $w = -1$. We will discuss this aspect in more detail in section 1.7.

For a pressureless material, usually called *dust*, $w = 0$. This approximation is good also for non-relativistic matter. Even if gas exerts pressure due to its temperature T, this would be negligible as $P \propto \frac{k_B T}{m_p c^2} \approx 0$.

Relativistic matter and radiation as neutrinos and photons (*radiative fluid*) have $w = 1/3$.

For ordinary matter, it is not possible to have $w > 1$ or $w < 0$, because in this case the sound speed of the fluid v_s will exceed the speed of light or be imaginary, this happens because

$$v_s = \left(\frac{\partial P}{\partial \rho} \right)_S^{1/2}, \tag{1.16}$$

where S is the entropy.

Inserting these relations into equation 1.12, we can solve it to find the time evolution of the different components, in general we will have

$$\rho = \rho_0 \left(\frac{a_0}{a}\right)^{3(1+w)}, \tag{1.17}$$

if w is constant. So for dust $\rho_m = \rho_{m,0}(1+z)^3$, for radiation $\rho_r = \rho_{r,0}(1+z)^4$ and for cosmological constant $\rho_\Lambda = constant$. The difference in the time evolution is explained as follows: for dust, the only relevant quantity is density and if the universe expands, it will change proportionally to the volume, so like the third power of the scale factor; for radiation, the number density of particles decreases as a^3, but their energy is also diluted by a factor a as the energy is inversely proportional to the wavelength. Due to the different time evolution, there is an epoch in the past when radiation dominates matter, the time when the two energy densities are equal is called equivalence time $a_{eq} = \Omega_{r,0}/\Omega_{m,0} \approx 3.2 \times 10^{-5}\ h^{-2}\Omega_{m,0}^{-1}$.
Assuming that either dust or radiation are perfect fluids, it is possible to derive their thermal evolution as a function of the scale factor, in particular for dust $T_m = T_{m,0}/a^2$ (if the adiabatic index is $\gamma = 5/3$) and for relativistic matter $T_r = T_{r,0}/a$, before the equivalence time these two temperatures had the same value, indicating a common evolution for dust and radiation.

Using the time evolution for all the cosmological components, equation 1.10 becomes

$$\left(\frac{\dot{a}}{a}\right)^2 = H(t)^2 = H_0^2 E(a)^2, \tag{1.18}$$

where

$$E(a) = \sqrt{\frac{\Omega_{r,0}}{a^4} + \frac{\Omega_{m,0}}{a^3} + \frac{\Omega_{K,0}}{a^2} + \Omega_{\Lambda,0}}. \tag{1.19}$$

Equation 1.18 has generally not an analytical solution, qualitatively it shows that there is an early phase dominated by radiation, followed by a matter-dominated period and at the end an era dominated by the cosmological constant.

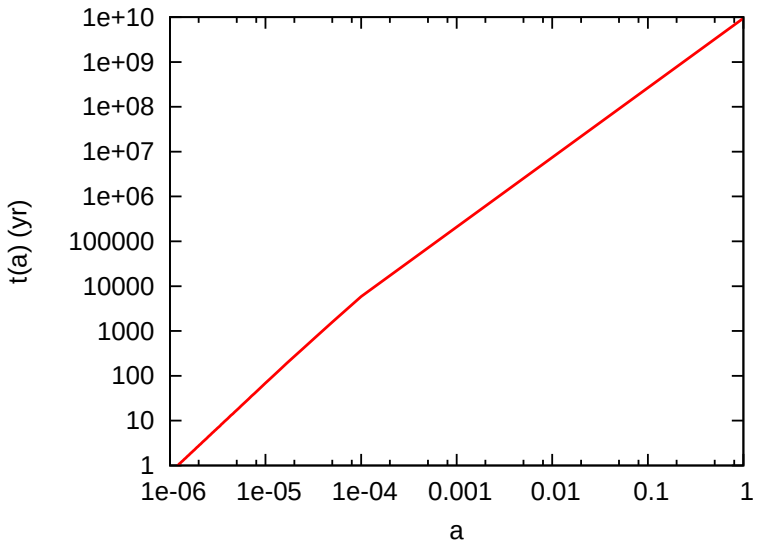

Figure 1.3: Time as a function of the scale factor for a flat model with $\Omega_m = 0.3$ and $\Omega_\Lambda = 0.7$.

From equation 1.18 it is easy to derive a relation between the scale factor and the cosmic time, solving the differential equation one gets

$$t = \frac{1}{H_0} \int_0^a \frac{da'}{a' E(a')} \tag{1.20}$$

In figure 1.3 we plot the evolution of the cosmic time as a function of the scale factor for a flat model dominated by the cosmological constant term.

A Friedmann model without any cosmological constant term and made of fluids with $w > -1/3$ has a point in time where $a = 0$, this is the so-called *Big Bang* and it represents a singularity of the model that is unavoidable if $w > -1/3$ and it is not a consequence of the symmetries of the system. It is possible to show that this also holds for more general conditions.

1.6 Distances in cosmology

Since in general relativity the space-time is not necessarily flat, there is not anymore a unique definition of distance, this implies that there will be different definitions of distances according to different measurement prescriptions.

In this section we will describe five different distance scales, namely the proper distance, the absorption distance, the comoving distance, the angular diameter distance and the luminosity distance. We suppose that the observer is placed at the origin of the coordinate system.

The *proper distance* is defined as the distance covered by a light beam propagating from a source at z_2 to an observer at z_1, with $z_1 < z_2$, from Eq. 1.2 the expression of the proper distance is

$$d_{pr} = \int_0^r \frac{a(t)dr'}{\sqrt{1-Kr'^2}} = a(t)f(r) = \frac{c}{H_0}\int_{a_2}^{a_1} \frac{da}{aE(a)}, \tag{1.21}$$

where $f(r)$ is

$$f(r) = \begin{cases} \arcsin r & K = 1 \\ r & K = 0 \\ \text{arcsinh} r & K = -1 \end{cases}. \tag{1.22}$$

As $a(t)$ changes in time, also d_{pr} will change in time, therefore the radial velocity of the object will be

$$v_r = \dot{a}(t)f(r) = \frac{\dot{a}(t)}{a(t)}f(r) = H(t)d_{pr}, \tag{1.23}$$

which represents the *Hubble Law*.

The *absorption distance* is a modified redshift distance used to remove the redshift dependence in a sample and put everything on a comoving coordinate scale. Therefore if the population of absorbers is not evolving (in other words if their space density times their cross section does not change with redshift), they have a constant number density per unit absorption distance. The relation between the absorption distance and the scale factor is

$$d_{ab} = \frac{c}{H_0}\int_{a_2}^{a_1} \frac{da}{a^4E(a)}. \tag{1.24}$$

The *comoving distance* is the distance on the spatial hypersurface at a constant time t between two points following the cosmic expansion flow.

It is the coordinate distance between the two points, or in other words the proper distance normalized over the scale factor:

$$d_c = \frac{d_{pr}}{a} = f(r) = \frac{c}{H_0}\int_{a_2}^{a_1} \frac{da}{a^2 E(a)}. \tag{1.25}$$

The *angular diameter distance* is defined in such a way that the relation $\Delta\theta d_A = \Delta A$ where $\Delta\theta$ is the angle subtended by the object and ΔA its proper length, valid for a Euclidean space, holds also for a curved space. As from equation 1.2 $\Delta A = af(r)\Delta\theta$, then the angular diameter distance is

$$d_A = ar, \tag{1.26}$$

where r is the radial coordinate distance, in general the angular diameter distance can be written as $d_A = af(r)$.

The *luminosity distance* is the distance preserving the Euclidean relation between the luminosity L and the flux F of an object. The photons emitted by the source are redshifted due to the expansion of the universe by a factor a and their time arrival is also delayed by a factor a, so

$$F = \frac{L}{4\pi r^2}a^2, \tag{1.27}$$

which implies

$$d_L = \left(\frac{a_0}{a_e}\right)^2 d_A. \tag{1.28}$$

where a_0 and a_e are the scale factors at receiving time and emission time.
This relation goes under the name of *Etherington relation* (Etherington, 1933) and is valid in any arbitrary space-time.

Other measures of distance, less often used are the *parallax distance* $d_\mu = a_0 r/\sqrt{1-Kr^2}$ and the *proper motion distance* $d_M = a_0 r$.

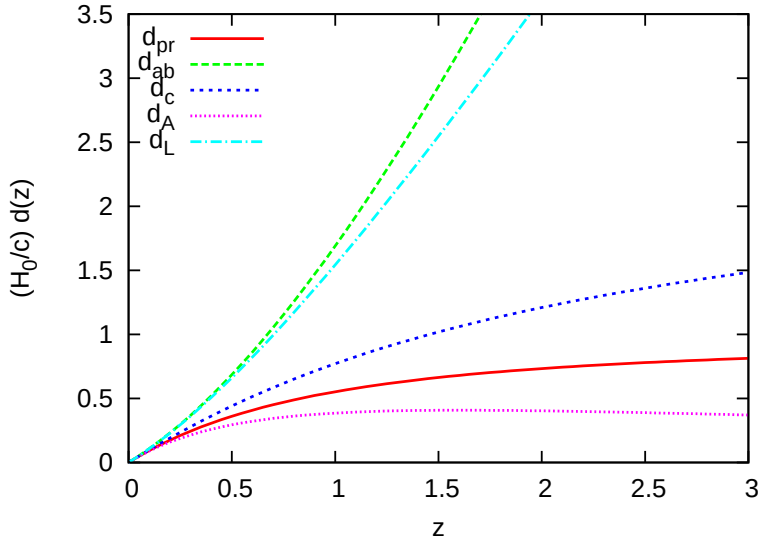

Figure 1.4: The five distance measures discussed are shown as a function of redshift for a cosmological model with $\Omega_m = 0.3$ and $\Omega_\Lambda = 0.7$. The red curve is the proper distance, the green curve is the absorption distance, the blue curve the comoving distance, the violet curve the angular-diameter distance and the cyan curve the luminosity distance. The distances shown are dimensionless, i.e. in units of the present Hubble radius ($c/H_0 \approx 3000$ Mpc/h).

For $z \ll 1$ all distances follow the Hubble law and will coincide in an euclidean geometry:

$$d = \frac{cz}{H_0} + O(z^2). \tag{1.29}$$

In figure 1.4 we show the main five distances defined above as a function of redshift for a spatially-flat universe.

1.7 Quintessence models

According to the standard model on the origin and evolution of the universe, after the *Big Bang*, the singularity from which everything probably originated, the universe underwent a period of exponentially accelerated expansion, phase usually called *inflation*. This model explains why the universe is so uniform on large scales and one of its predictions is that the spatial geometry should be flat. As we saw before, (see upper right panel in Fig

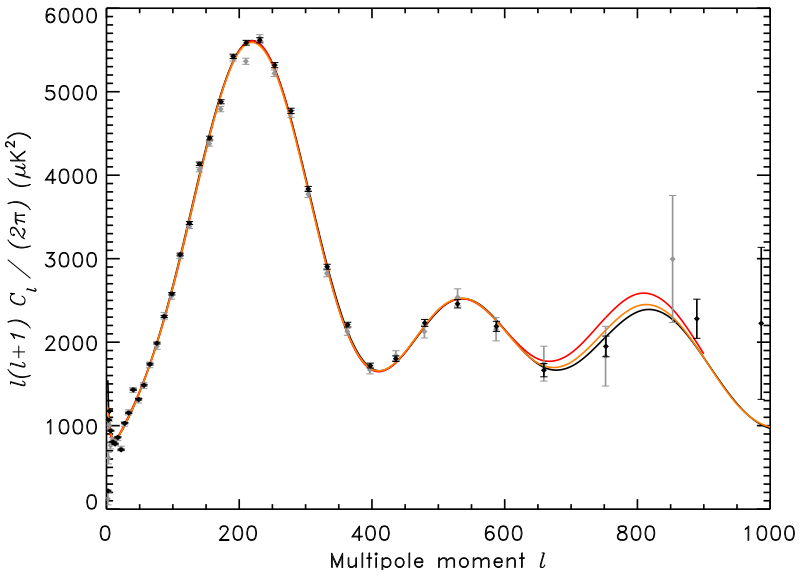

Figure 1.5: Best fit of the CMB temperature angular power spectrum for a ΛCDM model ($\Omega_m + \Omega_\Lambda = 1$). Different lines refer to WMAP three-years data (black line), one-year data (red line) and a combination of WMAP one-year data, CBI and ACBAR. From (Spergel et al., 2007)

1.2), matter can only account for about 30% of the total density of the universe. Moreover, starting from supernova observations (Riess et al., 1998; Perlmutter et al., 1999) which show an acceleration in the expansion of the Universe, up to the three-year data from the satellite WMAP (Spergel et al., 2007) for the observed CMB temperature power spectrum (see Fig 1.5), it is clear that the geometry of the Universe can be flat because of the presence of a contribution given by the cosmological constant or dark energy whose energy density is comparable to that of the matter today.

1.7.1 The cosmological constant

The cosmological constant Λ was first introduced by Einstein into his fields equations to allow static solutions.

It has an equation of state with $w = -1$, $P_\Lambda = -\rho_\Lambda c^2$ where

$$\rho_\Lambda = \frac{\Lambda c^2}{8\pi G}, \tag{1.30}$$

with Λ positive.

From elementary particle physics it is possible to relate the cosmological constant to the vacuum pressure and density, and the related stress-energy tensor is

$$T_{\mu\nu} = \frac{\Lambda c^4}{8\pi G} g_{\mu\nu}. \tag{1.31}$$

Observational constraints on the cosmological constant come from the curvature parameter K and from the measurements of the deceleration parameter that in presence of the cosmological constant assumes the form

$$q_0 = \frac{1}{2}\Omega_{m,0} - \Omega_{\Lambda,0}, \tag{1.32}$$

The upper limits are $|\Lambda| < 10^{-55}\ cm^2$ and $m_\Lambda < 10^{-42}$ GeV. Such small values are difficult to explain in the framework of the current physical theories. A possible solution are the dark energy models, treated in the next section.

1.7.2 Dark energy

In this section we give a basic introduction to the dark energy models, a more complete description can be found in the reviews by Peebles & Ratra (2003); Wetterich (2002); Sahni (2005).

A possible solution to the fact that the value of cosmological constant is so small, even if its energy density is constant in time comes from the *dark energy models* which represent a generalization of it with a time varying equation of state. Also for dark energy models, the time evolution is of the type a^n, where in this case $n = \exp\left(3\int_a^{a_0}(1+w(a))d\ln a\right)$.

Usually the dynamical evolution of dark energy is studied modelling it with a scalar field ϕ, whose kinetic energy is $T_{kin} = \frac{1}{2}\dot{\phi}^2$ and the potential is $V(\phi)$.

In the rest frame in which an observer moves in such a way that the universe appears isotropic, the stress-energy tensor of the scalar field ϕ is diagonal and the time-component and the space-components are associated respectively to the density and the pressure of

the field, whose expression in terms of the field is

$$P_\phi = \frac{1}{2}\dot{\phi}^2 - V(\phi),\ \rho_\phi = \frac{1}{2}\dot{\phi}^2 + V(\phi), \tag{1.33}$$

and the equation of state parameter becomes

$$w = \frac{\frac{1}{2}\dot{\phi}^2 - V(\phi)}{\frac{1}{2}\dot{\phi}^2 + V(\phi)}. \tag{1.34}$$

If $\dot{\phi}^2 \ll V(\phi)$ (*slow-rolling condition*) then $w \simeq -1$ and the dark energy reduces to the cosmological constant, in any case, whatever w is, it must be $w < -1/3$ to have an accelerated expansion.
Dark energy can recover the cosmological constant during the inflationary phase (accelerated expansion phase), when the slow rolling condition is satisfied.

The dynamics of the scalar field is governed by the following equation of motion, valid if the curvature is negligible:

$$\ddot{\phi} + 3H\dot{\phi} - \nabla^2\phi + \frac{dV(\phi)}{d\phi} = 0, \tag{1.35}$$

the term $\nabla^2\phi$ is zero if the scalar field is spatially homogeneous.
The mass of the field is related to the potential: $m_\phi = V''(\phi)$.

The interaction between the scalar field and the gravity can be studied either in the *Jordan frame* with a Lagrangian of the type $L = -f(\phi)R + L_m(m)$ or in the *Einstein frame* with a Lagrangian of the type $L = -R + L_m(m,\phi)$; both approaches lead to the same modification of the original metric.

If the scalar field interacts with matter, then dark energy can be considered as a dark force, this implies that matter is not conserved anymore and the matter feels an additional contribution to gravity that can be parametrized modifying the gravitational constant with the expression

$$G(r) = G(1 + \beta e^{-r/\lambda}). \tag{1.36}$$

Different behaviours of the scalar field correspond to different choices of the potential. In the literature many different potentials were suggested, like power laws (Lucchin & Matarrese, 1985; Peebles & Ratra, 1988), inverse power laws (Ratra & Peebles, 1988), exponential (Ratra & Peebles, 1988; Wetterich, 1988; Ferreira & Joyce, 1998).

A common characteristic of quintessence models is that they can be attractors (Ratra & Peebles, 1988) or trackers (Steinhardt et al., 1999), this implies that they are the asymptotic solutions of a wide range of initial conditions at high redshifts. The tracker behaviour is a very desirable feature because it can alleviate the coincidence problem.

We saw that $w = -1$ for a cosmological constant term, as observations allow slightly more negative values for this parameter, a wealth of phantom (or ghost) models are also under investigation. Their characteristic is to have today $w < -1$, this is possible only having a negative definite kinetic energy. We do not enter into details, but we remand to the papers Caldwell (2002); Johri (2004); Faraoni (2005); Kujat et al. (2006) for an overview.

Recently, great attention has been devoted to a class of models called *early dark energy* models, in which the contribution of dark energy at early times is not negligible.
While usually the time evolution of quintessence models is given with the parametrization of $w(a)$, for early dark energy models is more convenient to give explicitly $\Omega_d(a)$, where Ω_d represents the amount of dark energy at early times.
A possible parametrization is (see Doran & Robbers, 2006)

$$\Omega_d(a) = \frac{\Omega_d^0 - \Omega_d^e(1-a^{-3w_0})}{\Omega_d^0 + \Omega_m^0 a^{3w_0}} + \Omega_d^e(1-a^{-3w_0}), \tag{1.37}$$

where Ω_d^0 and Ω_m^0 are the fractional densities of dark energy and dark matter today, Ω_d^e is the amount of early dark energy and $w_0 = w(a=1)$ is the equation of state parameter today. The amount of early dark energy is a few per cent. Direct consequences of these models are a decrease of the distance measurements and of the age of the universe compared to a ΛCDM model, halos are more concentrated so strong lensing is enhanced, as well as the weak lensing on small scales.

Early dark energy affects also non-linear structure growth. In particular, as the linear density contrast is lowered compared to a ΛCDM model, than the mass function will increase as it depends exponentially on it (as shown in section 2.3.2). Therefore it is expected to find more halos in a early dark energy cosmologies than in a ΛCDM model. For the same reason also the number of major mergers will be enhanced in these kind of models.
More quantitative details and observational constraints on early dark energy models can be found in Wetterich (2004); Doran et al. (2005); Doran & Robbers (2006); Bartelmann et al. (2006).

Chapter 2

Structure formation

In the previous chapter we considered the universe as homogeneous and isotropic on scales larger than 100 Mpc/h, on smaller scales this condition does not apply anymore and it is populated by galaxies, clusters and superclusters. It is believed that these structures originated from *gravitational instability* of primordial fluctuation seeds whose origin is still uncertain. A possible explanation might come from inflationary theories. It is believed that these fluctuations have a random Gaussian distribution and it is on this assumption that all the theory on structure formation and perturbation growth is based.

Density perturbation growth undergoes two different regimes, that can be classified into *linear regime* and *non-linear regime*. The two phases differ by the value of the *density contrast* $\delta(\vec{x},t) = (\rho(\vec{x},t) - \bar{\rho}(t))/\bar{\rho}(t)$: for $\delta(\vec{x},t) < 1$ the perturbations can be studied in the framework of the linear regime, for $\delta(\vec{x},t) > 1$ the regime becomes non-linear and an analytical treatment is generally not possible and usually numerical techniques are employed. Linear evolution holds just for a limited period of time, followed by the non-linear evolution.

The evolution of cosmological structures takes place in a scenario where the dominant matter component is *cold dark matter* (*CDM*), a non-relativistic fluid interacting only gravitationally, a small fraction of baryonic matter, whose main contribution comes from diffuse gas, a quintessence component driving the accelerated expansion of the universe and that in the simplest case interacts only gravitationally with other components. The spatial geometry of the universe is flat (as supported also by inflationary theories) and

the amplitude of primordial fluctuations at recombination are of the order of $\delta(\vec{x}) \approx 10^{-3}$. Due to the collisional nature of baryonic matter, CDM will collapse first, followed then by baryons. In section 2.1 and 2.3 we describe respectively the linear and non-linear theory with their consequences. The linear evolution of the density power spectrum is introduced in section 2.2. In section 2.4 we briefly report the consequences when a small contribution of early dark energy is taken into account.

2.1 Linear theory

To study the evolution of density perturbations, taking into account also the Hubble expansion, can be done coherently with a full relativistic analysis. In order to do so, one has to consider the perturbed Einstein's field equations:

$$\delta G_{\mu\nu} = \frac{8\pi G}{c^4}\delta T_{\mu\nu} + \Lambda \delta g_{\mu\nu}, \tag{2.1}$$

where $\delta G_{\mu\nu}$, $\delta g_{\mu\nu}$ and $\delta T_{\mu\nu}$ are the perturbed quantities. The solutions of this equation will provide a complete description of scalar, vectorial and tensor perturbations. For our future discussions only the evolution of scalar quantities will be relevant, in this case the perturbed metric can be written as

$$\delta g_{\mu\nu} = a(t)^2 \begin{pmatrix} 2\psi(\vec{x},t) & \nabla w_s \\ \nabla w_s & 2\Phi(\vec{x})\delta_{i,j} \end{pmatrix}, \tag{2.2}$$

where ψ, w_s and Φ represent the perturbations (with a modulus smaller than unity) and the off-diagonal terms can be removed after a gauge transformation. In general the two potentials ψ and Φ will be different. In a weak field approximation, justified by the fact that also for the most massive structures $\Phi/c^2 \ll 1$, the two potentials are equal and it is possible to recover the same equations of the Newtonian approach.

In a classical study of the evolution of the perturbations, the relevant quantities are the density ρ, the pressure P, the entropy S, the velocity $\vec{u}$ and the potential Φ. They are related to each other through a system of equations

$$\begin{aligned} \frac{\partial \rho}{\partial t} + \nabla_{\vec{r}} \cdot (\rho \vec{u}) &= 0, \\ \frac{\partial \vec{u}}{\partial \vec{t}} + (\vec{u} \cdot \nabla_{\vec{x}})\vec{u} + \frac{\nabla_{\vec{r}} P}{\rho} + \nabla \Phi_{\vec{r}} &= 0, \\ \nabla^2 \Phi - 4\pi G \rho &= 0, \\ \frac{\partial S}{\partial t} + \vec{u} \cdot \nabla_{\vec{r}} S &= 0, \end{aligned} \tag{2.3}$$

that in this order represent the *continuity equation*, the *Euler equation*, the *Poisson equation* and the *entropy conservation equation*, $\vec{r}$ is the physical coordinate. In an expanding universe, the previous equations become

$$\begin{aligned} \frac{\partial \rho}{\partial t} + 3\frac{\dot{a}}{a}\rho + \frac{1}{a}\nabla_{\vec{x}} \cdot (\rho \vec{u}) &= 0, \\ \frac{\partial \vec{u}}{\partial \vec{t}} + \frac{1}{a}(\vec{u} \cdot \nabla_{\vec{x}})\vec{u} + \frac{\dot{a}}{a}\vec{u} + \frac{\nabla P}{a\rho} + \frac{1}{a}\nabla_{\vec{x}} \Phi &= 0, \\ \nabla^2_{\vec{x}} \Phi - 4\pi G a^2 (\rho - \rho_b) &= 0, \\ \frac{\partial S}{\partial t} + \frac{1}{a}\vec{u} \cdot \nabla_{\vec{x}} S &= 0, \end{aligned} \tag{2.4}$$

where $\vec{x}$ is the comoving coordinate of the fluid ($\vec{r} = a\vec{x}$) and ρ_b the average density of the universe. The velocity is expressed as

$$\vec{u} = \dot{\vec{r}} = \dot{a}\vec{x} + a\dot{\vec{x}} = H\vec{r} + \vec{v}, \tag{2.5}$$

where $\vec{v}$ is the peculiar velocity of the fluid.

We suppose that all the processes are adiabatic and we consider small perturbations as we want to study the evolution of the perturbations in the linear regime. Using the substitution for the perturbed solutions

$$
\begin{aligned}
\rho &= \rho_b(1+\delta), \\
P &= P_b + \delta P, \\
\vec{u} &= H\vec{r} + \vec{v}, \\
\Phi &= \phi + \delta\phi, \\
S &= S_b + \delta S
\end{aligned}
\tag{2.6}
$$

in the previous set of equations, we obtain the equations describing the evolution of the perturbations:

$$
\begin{aligned}
\frac{\partial \delta}{\partial t} + 3H\delta + \rho_b \nabla_{\vec{x}} \cdot \vec{v} &= 0, \\
\frac{\partial \vec{v}}{\partial t} + H\vec{v} + \frac{\nabla_{\vec{x}} P}{\rho} + \nabla_{\vec{x}}\delta\phi &= 0, \\
\nabla^2_{\vec{x}}\delta\phi - 4\pi G a^2 \rho_b \delta &= 0, \\
\frac{\partial \delta S}{\partial t} &= 0.
\end{aligned}
\tag{2.7}
$$

The solution to these equations can be decomposed into plane waves, $\delta_i(\vec{x},t) = \sum_{k=1}^{\infty} \delta_k(t) exp(i\vec{k}\vec{x})$, because all the modes are decoupled and the gaussianity of the field is preserved. Inserting the plane waves into equation 2.7 and combining them together leads to the equation describing the linear evolution of the density perturbation:

$$
\ddot{\delta}_k + 2\frac{\dot{a}}{a}\dot{\delta}_k + \left[v_s^2 \frac{k^2}{a^2} - 4\pi G \rho_b \right] \delta_k = 0, \tag{2.8}
$$

where k is the comoving wave number, $v_s = \sqrt{\delta P / \delta \rho}$ the sound speed. It is valid for a single non-relativistic matter component on scales $\lambda < R_H$, where R_H indicates the cosmological horizon.

In case of a multi-fluid system, equation 2.8 becomes

$$
\ddot{\delta}_{k,i} + 2\frac{\dot{a}}{a}\dot{\delta}_{k,i} + \delta_{k,i} v_{s,i}^2 \frac{k^2}{a^2} - 4\pi G \sum_j \rho_{b,j} \delta_{k,j} = 0, \tag{2.9}
$$

Epoch	δ_R	δ_{DM}	δ_B
$a < a_{eq}$			
$\lambda > R_H$	$\propto a^2$	$\propto a^2$	$\propto a^2$
$\lambda < R_H$	oscillation	oscillation	stagnation
$a_{eq} < a_{rec}$			
$\lambda > R_H$	$\propto a$	$\propto a$	$\propto a$
$\lambda < R_H$	oscillation	$\propto a$	oscillation
$a > a_{rec}$			
$\lambda > R_H$	$\propto a$	$\propto a$	$\propto a$
$\lambda < R_H$	oscillation	$\propto a$	$\delta_{DM}(1+\frac{a_{eq}}{a})$ (before catch-up)
			δ_{DM} (after catch-up)

Table 2.1: Summary of the solutions for the perturbation growth for radiation, dark matter and baryons (δ_R, δ_{DM} and δ_B respectively). The first column refers to the epoch and the perturbation scale λ considered, the second, the third and the fourth column show the quantity under investigation.

where the index *i* refers to the different components. Similar equations apply to relativistic matter and scales larger than the cosmological horizon.

Applying equation 2.9 to baryons after decoupling and on scales where pressure terms can be neglected, we find the following relation:

$$\ddot{\delta}_{k,b} + 2\frac{\dot{a}}{a}\dot{\delta}_{k,b} - 4\pi G\rho_{k,DM}\delta_{k,DM} = 0, \tag{2.10}$$

since radiation and baryons densities are much smaller than the dark matter density, and the solution is

$$\delta_{k,b} = \delta_{k,DM}\left(1 - \frac{a_{dec}}{a}\right). \tag{2.11}$$

Equation 2.11 shows that after the decoupling baryon fluctuations grow faster than the dark matter fluctuations because they fall in the potential well already formed by dark matter, this effect is called *baryonic catch-up*.

In table 2.1 we give a summary of the time evolution of the perturbations relevant for structure growth.

From the density contrast it is possible to study peculiar velocities and accelerations.

Defining the quantity

$$f(\Omega) = \frac{d\ln\delta}{d\ln a}, \tag{2.12}$$

the solution for the peculiar velocity field is

$$\vec{v}(t) = \frac{2f(\Omega)}{3aH\Omega}\nabla\delta\phi. \tag{2.13}$$

For models with $\Lambda = 0$, an excellent approximation for $f(\Omega)$ is $f(\Omega) = \Omega^{0.6}$ (Peebles, 1980), for a model with cosmological constant a better fit is $f(\Omega) = \Omega^{0.6} + \frac{\Omega_\Lambda}{70}(1 + \frac{1}{2}\Omega)$.

The *Jeans wavelength* is defined as

$$\lambda_J = \sqrt{\frac{\pi v_s^2}{G\rho}}, \tag{2.14}$$

perturbations with $\lambda > \lambda_J$ are unstable and their growth depends on the geometry of the universe, the others behave as sound waves. To the Jeans length is associated the *Jeans mass* $M_J = \frac{4\pi}{3}\rho\lambda_J^3$, as before, perturbations with $M > M_J$ will growth.

As equation 2.8 is a second-order differential equation, there will be two solutions, a growing and a decaying one. We will consider only the growing solution.

In an Einstein-de Sitter (EdS) model, linear theory shows that before the equivalence time $\delta(a) \propto a^2$ and after $\delta(a) \propto a$; when this limit does not hold anymore, the linear evolution of density contrast follows

$$\delta(a) = \delta_0 D(a), \tag{2.15}$$

where $D(a)$ is the *growth factor* and for an EdS universe $D(a) = a$ and for other models it is expressed as a function of the relative growth factor $g(a)$, $D(a) = ag(a)/g(a=1)$. In the case of non-dynamical dark energy, the expression giving the relative growth factor is

$$g(a) = \frac{5}{2}\Omega_m(a)E(a)\int_0^a \frac{da'}{(a'E(a'))^3}, \tag{2.16}$$

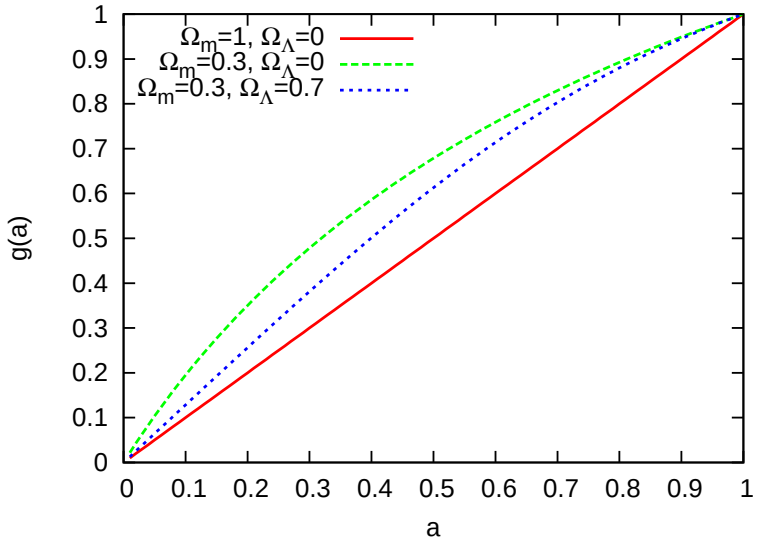

Figure 2.1: The growth function $ag(a)$ for different cosmological models. The red curve shows an EdS model ($\Omega_m = 1$ and $\Omega_\Lambda = 0$), the blue curve on open model with $\Omega_m = 0.3$ and $\Omega_\Lambda = 0$, the green curve a flat model with cosmological constant.

it could be expressed in terms of elliptical functions (Eisenstein, 1997), but it is more convenient giving an approximate parametrization (Carroll et al., 1992):

$$g(a) \approx \frac{5}{2}\frac{\Omega_m(a)}{\Omega_m(a)^{4/7} - \Omega_\Lambda(a) + (1+\frac{\Omega_m(a)}{2})(1+\frac{\Omega_\Lambda(a)}{70})}. \tag{2.17}$$

This expression is valid for open or Λ-dominated flat universes.

In figure 2.1 we show the evolution of $g(a)$ for different cosmological models

The relative growth factor is constant for an EdS model, while for small Ω_m it is higher for $a \ll 1$ and smaller for $a \approx 1$. This implies that in a low-density universe structures form earlier than in high-density universe and at late times the expansion is faster and it reduces the speed of structure formation. For a flat universe with cosmological constant, the epoch where the cosmological constant starts to dominate is $a \approx (\Omega_m/\Omega_\Lambda)^{1/3}$.

The scales of density perturbations can exceed the size of causally connected regions; this size goes under the name of *cosmological horizon* $R_H = c/H(a)$. The mass enclosed in a sphere of radius R_H, $M_H = 4/3\pi\rho R_H^3$ is called *horizon mass*. Perturbations with $M < M_H$ can experience dissipation processes, that are briefly described in the next section.

2.1.1 Dissipation processes

Till this point, the cosmological fluids were considered as ideal, if this approximation breaks down, the energy is drained away by dissipative processes. They have different origins in dark matter and baryons because dark matter feels only gravitational effects, while baryons are a collisional fluid that can couple to other species, such as radiation.

For $a < a_{eq}$ the evolution of the universe is dominated by radiation and non-relativistic matter perturbations do not growth until a_{eq} even if $\lambda \gg \lambda_J$. This effect of freezing-in or stagnation in perturbations goes under the name of *Meszaros effect* (Meszaros, 1974) and it is very important in models of galaxies formation originating from primordial fluctuations in an universe dominated by cold dark matter. In this scenario, the free-fall time is larger than the expansion, this means that perturbations can not grow because the expansion is too fast. The solution to equation 2.8 for the growing mode is $\delta = 1 + \frac{3}{2}\frac{a}{a_{eq}}$.

Radiation drag is due to the coupling between baryonic matter and radiation after the recombination: perturbations are frozen because of the viscous friction of baryons with photons. This effect is relevant if the viscous friction force dominates the self-gravitating force. Solving equation 2.8 shows that the perturbations remain practically constant till recombination. Radiation drag is different from the Meszaros effect as this last effect is purely kinematic and does not require any collisional interaction between the two fluids.

Before recombination, the cosmological fluid can be considered as a plasma of photons, electrons and protons that experiences dissipative effects due to the diffusion of photons. The region affected by photon diffusion changes in time as $R_D \propto (c^2 \tau_{\gamma_e} t)^{1/2}$ where τ_{γ_e} is the time scale for the collisions between photons and electron-proton pairs. The *dissipation mass* or *Silk mass* (Silk, 1967) is the mass of a sphere of radius R_D, perturbations with $M < M_S$ will not grow. This effect lasts till recombination.

Dark matter perturbations can undergo a dissipation effect called *free-streaming* which consists in the diffusion of particles from overdense to underdense regions. Perturbations are completely washed out when their mass is equal to the *free-streaming mass* $M_{FS} =$

$4/3\pi\rho R_{FS}^3$ where

$$R_{FS} = a\int_0^t \frac{v(t')}{a(t')}dt'. \tag{2.18}$$

For cold dark matter $M_J \approx M_{FS} \approx 10^3 M_\odot/h$ at recombination, this means that structures with low mass will form first.

2.2 Density power spectrum

As said in the previous section, it is convenient to express the solution of the equation describing the time evolution of the density contrast as superposition of plane waves. Assuming that the perturbation field follows a Gaussian statistics, then its statistical aspects are completely described by the *power spectrum*, a second order moment related to the variance of the field.

The density contrast is defined as

$$\delta(\vec{x}) = \frac{\rho(\vec{x}) - \rho_b}{\rho_b}, \tag{2.19}$$

where ρ_b is the background density, from the definition is clear that $\langle\delta\rangle = 0$. Defining the Fourier transform as

$$\hat{\delta}(\vec{k}) = \int_{-\infty}^{+\infty} d^3x\, \delta(\vec{x})\, e^{\imath\vec{k}\vec{x}}, \tag{2.20}$$

the variance of δ in Fourier space defines the power spectrum:

$$\langle\hat{\delta}(\vec{k})\hat{\delta}(\vec{k'})^*\rangle = (2\pi)^3 P(k)\delta_D(\vec{k}-\vec{k'}), \tag{2.21}$$

where the asterisk * denotes the complex conjugate and $\delta_D(\vec{k}-\vec{k'})$ the Dirac's delta function. The variance of the field is related to the power spectrum by the equation

$$\sigma^2 = \frac{1}{2\pi^2}\int_0^\infty P(k)k^2 dk. \tag{2.22}$$

With this definition, the variance contains no information on the relative contributions of the different modes, and there is no guarantee that the integral in equation 2.22 converges. For this reason it is useful to define a variance that depends on the scale considered and that will represent the variance of a filtered power spectrum. Usually this quantity is called *mass variance* and it is defined as

$$\sigma_M^2 = \frac{1}{2\pi^2} \int_0^\infty P(k)\, k^2\, W_F^2(kR)\, dk, \tag{2.23}$$

where R is the scale under consideration, $W_F(kR)$ the Fourier transform of the filter. The most commonly used filter windows are the *top-hat* filter and the *Gaussian* filter. Most recent estimates for σ_8 (the variance in a radius of 8 Mpc/h) give (even if with a large scatter) $\sigma_8 \approx 0.8$ (Spergel et al., 2007).

Inflation predicts an almost scale-free initial power spectrum $P(k) = Ak^n$, where A is a normalization constant that can be inferred from observations of the local abundance of galaxy clusters (White et al., 1993; Eke et al., 1996b; Viana & Liddle, 1996; Tegmark & Zaldarriaga, 2002) and n is the spectral index $n \approx 0.95$ (Spergel et al., 2007), very close to $n = 1$ as predicted by inflationary models. If $n = 1$, then the primordial spectrum is called *Harrison-Zel'dovich spectrum* (Harrison, 1970; Zel'dovich, 1970; Peebles & Yu, 1970).

As explained in section 2.1.1, the growth of density fluctuations is affected by several dissipative processes that ultimately change the shape of the primordial power spectrum. The power spectrum at a generic time a is then given by

$$P(k,a) = P(k,a_i)T^2(k)D(a)^2, \tag{2.24}$$

where $D(a)$ is the growth factor, $P(k,a)$ and $P(k,a_i)$ are the power spectrum at a generic time a and the power spectrum at an initial time a_i and $T(k)$ is the transfer function and, taking into account all the physical dissipative processes, shows how much the initial power spectrum is suppressed. It is defined as

$$T(k) = \frac{\delta_k(a_f)D(a_i)}{\delta_k(a_i)D(a_f)}, \tag{2.25}$$

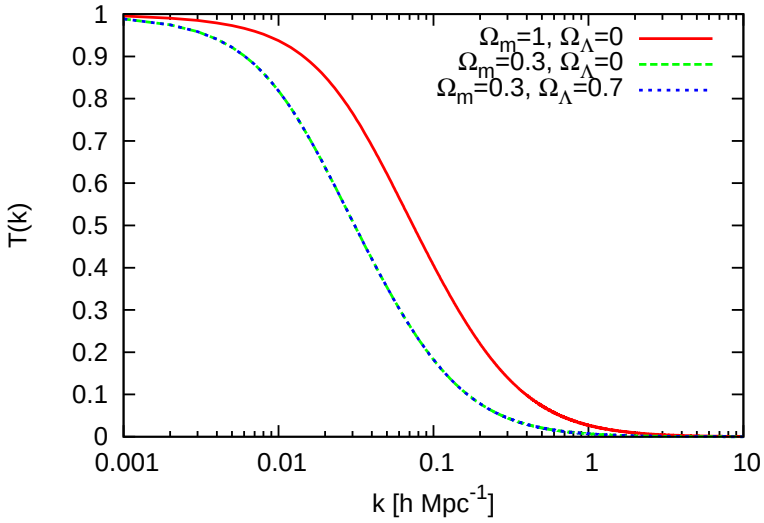

Figure 2.2: The transfer function $T(q)$ for different cosmological models. The red curve shows an EdS model ($\Omega_m = 1$ and $\Omega_\Lambda = 0$), the blue curve an open model with $\Omega_m = 0.3$ and $\Omega_\Lambda = 0$, the green curve a flat model with cosmological constant.

where i and f stand for initial and final. A common parametrization used for cold dark matter models is given by Bardeen et al. (1986):

$$T(q) = \frac{\ln(1+2.34q)}{2.34q}[1+3.89q+(16.1q)^2+(5.46q)^3+(6.71q)^4]^{-0.25}, \qquad (2.26)$$

where $q \equiv k/\Gamma\ h/Mpc$ and the shape parameter Γ is defined as (Sugiyama, 1995)

$$\Gamma = \Omega_{m,0}\ h\ \exp(-\Omega_{B,0}\ (1+\sqrt{2h}/\Omega_{m,0})). \qquad (2.27)$$

As shown in figure 2.2 the transfer function is unity for large scales where the fluctuation evolution is not affected by local phenomena, and zero for small scales where the local and suppression phenomena are most relevant.

2.3 Non-linear theory

As said before, the linear theory holds only as long as $\delta < 1$, after this value it breaks down and a non-linear analysis is needed. Typical examples for the non-linear density

fluctuations are galaxy clusters, for which $\delta \approx 10^3$. Once the field enters into the non-linear regime, it becomes non-Gaussian and its probability distribution assumes a skewed shape towards high values of δ.

To find analytical results in this section of the theory, it is necessary to study systems with a particularly simple symmetry, like a system with spherical or ellipsoidal symmetry. The collapse of such systems is described in the next section.

2.3.1 Spherical and elliptical collapse model

In these models it is assumed the existence of an overdense perturbation (with spherical or elliptical symmetry) that disentangles itself from the general expansion of the universe. The expansion rate of the overdense region will be smaller than the expansion rate of the rest of the universe and if it is dense enough the expansion will stop reaching a maximum size (*turn-around*) after which it will start to collapse and eventually form a bounded object. As the theory only includes gravitational interactions, the collapse ends in a singularity; in reality, because of scattering and the pressure of gas the overdense region will stop its contraction before reaching the singularity and it will be considered virialized when the *virial theorem* holds.

Even if the geometries taken into account are really easy and quite idealistic (in general the collapsing structures have an irregular shape), the equations describing the evolution of the infalling object can not be solved analytically for a generic cosmological model. Moreover, the contribution of quintessence in the equations of motions is still under debate. If quintessence reduces to the cosmological constant, then it does not affect the treatment of the system considered without it, otherwise if quintessence is a dynamical scalar field, it enters directly into the equations and two cases must be distinguished. Caldwell et al. (1998) showed that quintessence cannot be perfectly smooth, but it is generally believed that the clustering of the field should be negligible for scales smaller than ≈ 100 Mpc/h and Maor (2006) argued that including the quintessence explicitly in the equations could lead to a non-conservation of energy. So including or not including quintessence clustering will lead to different results.

To sketch the basis of the spherical collapse, we will refer to an EdS model for scales smaller than the cosmological horizon. Of other models we shall give fitting formulae. The equation of motion for the radius R that a spherical infalling mass shell satisfies is

$$\ddot{R} = -\frac{GM}{R^2} = -\frac{4\pi}{3}\rho R^3 \frac{G}{R^2}, \tag{2.28}$$

(if dark energy is included then ρ represents the total density of the system) and an integral of motion (energy conservation) is

$$\frac{1}{2}\dot{R}^2 - \frac{GM}{R} = E, \tag{2.29}$$

where E is the total energy of the system. If $E < 0$ then the mass shell will collapse. The object reaches $R = R_{max}$ with a density $\rho \approx 5.5\rho_{back}$ (where ρ_{back} is the density of the unperturbed background) and then collapses. The virialization condition gives $R_{vir} = R_{max}/2$ and the overdensity is $\Delta_v = 18\pi^2 \approx 178$. At the same time, an extrapolation from the linear theory would give a density contrast $\delta_c = \frac{3}{5}\left(\frac{3\pi}{2}\right)^{2/3} \approx 1.68$.
Approximate formulae for an open model and a model with cosmological constant are:

$$\delta_c = \frac{3}{5}\left(\frac{3\pi}{2}\right)^{2/3} \begin{cases} (1+0.0406\log_{10}\Omega_m) & \Omega_{\Lambda,0} = 0 \\ (1+0.0123\log_{10}\Omega_m) & \Omega_{m,0}+\Omega_{\Lambda,0} = 1 \end{cases} \tag{2.30}$$

and

$$\Delta_v = 18\pi^2 \begin{cases} (1+0.1210(\Omega_m-1)+\Omega_m^{0.6756}) & \Omega_{\Lambda,0} = 0 \\ (1+0.7076(\Omega_m-1)+\Omega_m^{0.4403}) & \Omega_{m,0}+\Omega_{\Lambda,0} = 1 \end{cases} \tag{2.31}$$

where Ω_m is the matter density parameter at the redshift of the halo collapse.

More technical details on the spherical collapse model can be found in several articles, (see e.g. Lahav et al., 1991; Wang & Steinhardt, 1998; Mota & van de Bruck, 2004; Horellou & Berge, 2005; Maor & Lahav, 2005).

As we will see in the next section, if instead of assuming a spherical collapse model one uses an ellipsoidal collapse model, the mass function is closer to what is found in the numerical simulations. Therefore we briefly sketch the framework of the ellipsoidal

collapse. More details can be found in Peebles (1980), Eisenstein & Loeb (1995), Bond & Myers (1996).

While in the spherical collapse model the evolution of the perturbations is described by the initial density field, for the aspherical model it is better described by the initial shear field and virialization is defined as the time of the third axis collapse. The collapse along each axis is stopped after it has shrunk by some critical factor and it is chosen in such a way that at the virialization the density contrast has the same value as in the spherical model.

The collapse is described by the three eigenvalues of the deformation tensor or equivalently by the initial ellipticity e, the prolateness p and the density contrast δ. In general virialization takes place later as e increases and fixing e, if p decreases and $\delta_{ec} > \delta_{sc}$ where *ec* and *sc* mean respectively ellipsoidal and spherical collapse.

It is possible to relate the two density contrasts through the relation (Sheth et al., 2001)

$$\delta_{ec}(\sigma, z) = \delta_{sc} \left\{ 1 + \beta \left[\frac{\sigma^2}{\sigma_*^2} \right]^{\gamma} \right\}, \tag{2.32}$$

where $\sigma_* \equiv \delta_{sc}(z)$, σ is the variance of the field, $\beta \approx 0.47$ and $\gamma \approx 0.615$. This expression is approximately valid for EdS, open and flat models with cosmological constant. For massive objects, as $\sigma \ll \sigma_*$, $\delta_{ec} \approx \delta_{sc}$. The utility of this relation can be understood noticing that δ_{ec} can be used instead of δ_{sc} in the excursion sets theory (discussed in section 2.3.2).

In figure 2.3 we show the behaviour of δ_c and Δ_v as a function of redshift for different cosmologies, namely an EdS model, an open model and a ΛCDM model for a collapsing sphere.

In section 2.2 we studied the evolution of the linear power spectrum. The power spectrum is affected by the non-linear evolution of the structures and computing the non-linear evolution of the spectrum is really hard. Normally numerical methods are required and it is possible to fit the non-linear power spectrum from cosmological simulations. Analytical formulae are obtained under simplifying assumptions. Supposing that the two-point

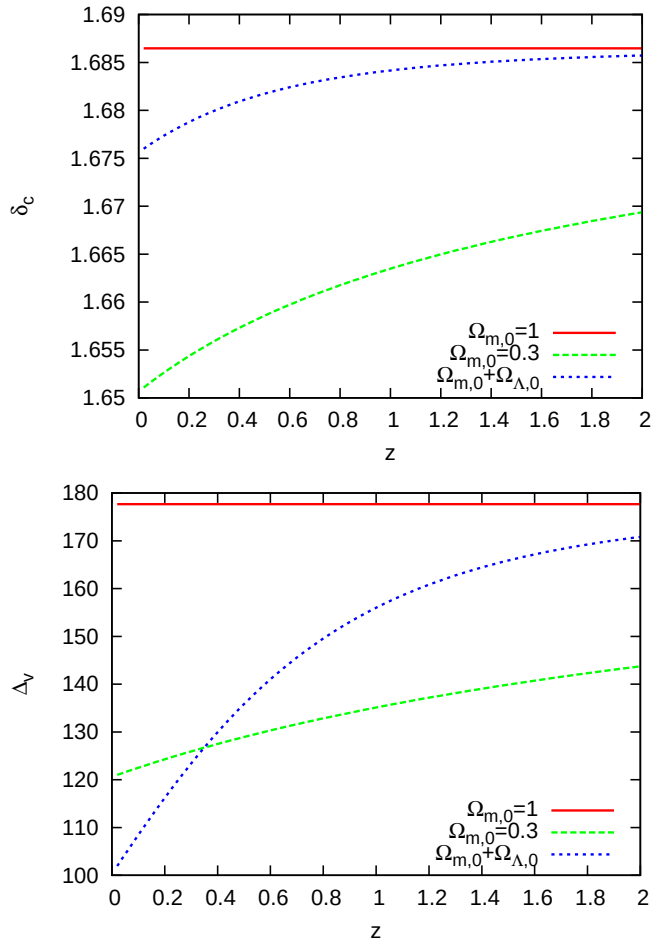

Figure 2.3: Virial overdensity as a function of redshift (upper panel) and density contrast at the collapse time t_c for three different cosmological models. In red we show the EdS model, in green an open model and in red a flat model with cosmological constant.

correlation functions for the linear and non-linear regimes are related by a scaling relation (Hamilton et al., 1991) allows to find analytical formulae for the non-linear evolution of the power spectrum (see e.g. Jain et al., 1995; Peacock & Dodds, 1996; Smith et al., 2003).

In figure 2.4 we show the linear (red line) and non-linear matter (green line) power spectrum at $z = 0$ for a ΛCDM model. The non-linearity affects the small scales (large k) because the small structures are the first to enter into the non-linear regime.

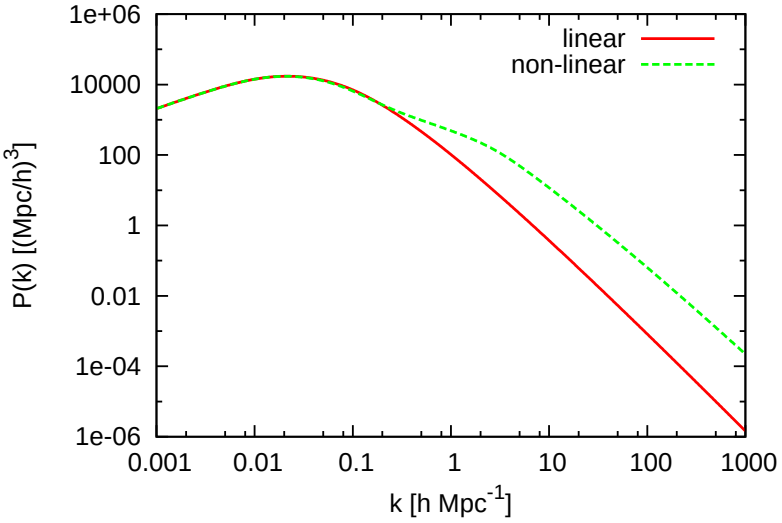

Figure 2.4: Linear (red curve) and non-linear (green curve) dark matter power spectrum for a ΛCDM model with $\Omega_m = 0.3$, $\Omega_\Lambda = 0.7$ and $h = 0.7$ at redshift $z = 0$.

2.3.2 Mass function

Much information on the distribution of the halos are contained in the *mass function*, a quantity representing the number of halos per mass interval at a given redshift.

The first attempt of computing the halos mass function traces back to the work of Press & Schechter (1974). Press-Schechter theory asserts that after smoothing the linear theory density field on some mass scale M (corresponding to a certain scale R) the fraction of space in which the smoothed density field exceeds a given threshold δ_c is in collapsed objects whose mass exceeds the smoothing mass M; assuming a density field following a Gaussian statistics it is easily possible to compute this quantity.

For a Gaussian field, the distribution of fluctuations is

$$P(\delta_M)d\delta_M = \frac{1}{(2\pi\sigma_M^2)^{1/2}} \exp\left(-\frac{\delta_M^2}{2\sigma_M^2}\right) d\delta_M, \tag{2.33}$$

where σ_M is the variance on a mass scale M. The probability that the fluctuation δ_M exceeds the threshold δ_c is given by

$$P(M) = \int_{\delta_c}^{\infty} P(\delta_M)\, d\delta_M, \tag{2.34}$$

this quantity depends on the filter mass and through the variance on time and it is proportional to the number of structures characterized by a density perturbation greater than δ_c. At this point the problem is that halos in underdense regions will not be counted. This problem, called the *cloud-in-cloud problem*, was originally solved by Press & Schechter multiplying by two to obtain the correct normalization. Then the mass function will be $N(M)MdM = 2\rho_m(P(M) - P(M+dM))dM$ that leads to the expression

$$N(M,z) = \sqrt{\frac{2}{\pi}} \frac{\rho_{crit}\Omega_{m,0}}{M} \frac{\delta_c}{D(z)\sigma_M^2} \left|\frac{d\sigma_M}{dM}\right| \exp\left[-\frac{\delta_c}{2D(z)^2\sigma_M^2}\right]. \tag{2.35}$$

The number density of objects with mass above M is then

$$N(>M,z) = \int_M^{\infty} \frac{dN(M,z)}{dM}\, dM \tag{2.36}$$

An alternative approach is the theory of density peaks proposed by Peacock & Heavens (1985) and by Bardeen et al. (1986). In this theory the objects with at least mass M are identified by the number of peaks in the smoothed density field above a given threshold and it was shown that the two theories agree very well, but they tend to differ for high masses.

Before we quoted the problem of normalization in the mass function. This problem can be overcome and fully justified in the theory of excursion sets (see e.g. Bond et al., 1991) that is based on a statistical approach according to which the evolution of dark matter halos is described by Brownian random motions in a two-dimensional space (σ^2, δ) and in this space it is considered the motion of a point $\vec{x}$ and the density field is filtered with a filter of scale R; a halo is formed at $\vec{x}$ if $\delta(\vec{x}) > \delta_c$ for some radius R.

The Brownian motion is described by the diffusion equation

$$\frac{\partial P}{\partial \sigma^2} = \frac{1}{2}\frac{\partial^2 P}{\partial \delta^2}, \tag{2.37}$$

where P is the probability distribution for a point having a density contrast $\delta_c < \delta < \delta_c + d\delta$ and for a Gaussian random field coincides with the expression given in equation 2.33 and then, including all the trajectories leading to the formation of a halo, the mass function, as given in equation 2.35, is recovered. In terms of the random walk, we introduce an *absorbing barrier* at δ_c such that points with trajectories $\delta(\vec{x})$ hitting the barrier are removed from counting them as not being part of halos.

Equation 2.35 is in good agreement with mass functions from numerical simulations, but for small and large masses it is inaccurate. A better agreement with simulations was found by Sheth & Tormen (1999):

$$N(M,z) = \sqrt{\frac{2aA^2}{\pi}}\frac{\rho_{crit}\Omega_{m,0}}{M}\frac{\delta_c}{D(z)\sigma_M^2}\left[1+\left(\frac{D(z)\sigma_M}{\sqrt{a}\delta_c}\right)^p\right]\left|\frac{d\sigma_M}{dM}\right| \times \exp\left[-\frac{\delta_c}{2D(z)^2\sigma_M^2}\right], \tag{2.38}$$

where $a = 0.707$, $A = 0.3222$ and $p = 0.3$. Equation 2.38 reduces to the Press-Schechter formula for $a = 1$, $A = 0.5$ and $p = 0$.

This expression can also be recovered analytically assuming an ellipsoidal collapse and a moving barrier in the excursion set frame (see Sheth et al., 2001; Sheth & Tormen, 2002).

Jenkins et al. (2001) found a fitting formula from $N-body$ simulations whose shape is almost indistinguishable from equation 2.38, their fit is

$$N(M,z) = 0.315\exp\left(-|\ln\sigma^{-1} + 0.61|^{3.8}\right). \tag{2.39}$$

In figure 2.5 we show the three different mass functions at two different redshifts. The Press-Schechter mass function overpredicts the number of small halos and underpredicts the number of massive halos. The other two differ in the very high mass tail.

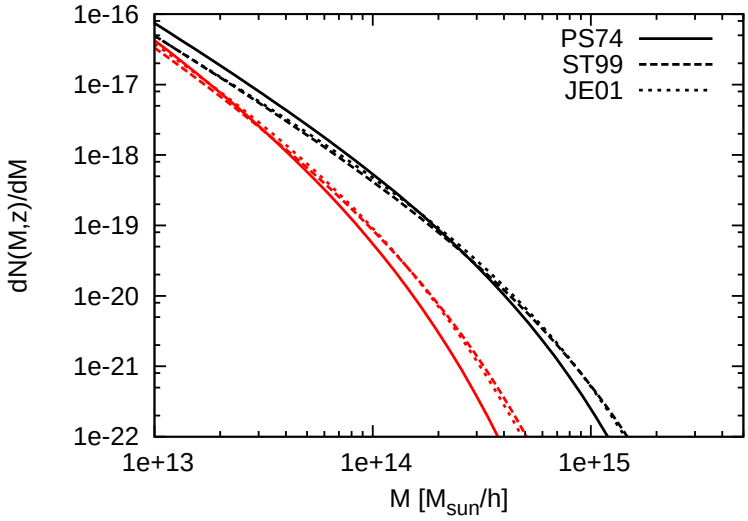

Figure 2.5: Mass function for a flat model $\Omega_m + \Omega_\Lambda = 1$ at redshift $z = 0$ (black curves) and $z = 1$ (red curves). The solid line (PS74) shows the mass function in the original prescription of Press & Schechter (1974), the dashed line the mass function of Sheth & Tormen (1999) and the dotted line is the numerical fit of Jenkins et al. (2001)

2.3.3 Merger rate

The excursion set model or *extended Press-Schechter theory* allows to compute several quantities describing the merging properties of the halos, the halo-survival times and so on.

In the theory the relevant quantity appearing is the ratio δ_c/σ_M, thus we can consider the barrier moving towards zero as time passes; this can be interpreted with the fact that the halo collapse becomes more probable as the halo evolves.

The conditional probability that a halo of mass M_1 at a time t_1 creates a halo of mass $M_2 > M_1$ at the time $t_2 > t_1$ is given by

$$P(\sigma_1^2(M_1), \delta_c(t_1) | \sigma_2^2(M_2), \delta_c(t_2)) = \frac{(\delta_c(t_1) - \delta_c(t_2))}{\sqrt{2\pi}(\sigma_1^2(M_1) - \sigma_2^2(M_2))^{3/2}} \times \exp\left[-\frac{(\delta_c(t_1) - \delta_c(t_2))^2}{2(\sigma_1^2(M_1) - \sigma_2^2(M_2))} \right], \tag{2.40}$$

with $\sigma_1^2(M_1) > \sigma_2^2(M_2)$ e $\delta_c(t_1) > \delta_c(t_2)$.

Taking the limit of equation 2.40 for $t_2 \to t_1$ leads to the *merger rate*, this expression can be interpreted as the probability that in time interval dt a halo of mass M_1 merges with a halo of mass $\Delta M = M_2 - M_1$ to form a halo of mass M_2:

$$\frac{d^2P}{d\ln\Delta M d\ln t}(M_1 \to M_2|t) = \left(\frac{2}{\pi}\right)^{1/2} \left|\frac{d\ln\delta_c(t)}{d\ln t}\right| \left(\frac{\Delta M}{M_2}\right) \left|\frac{d\ln\sigma(M_2)}{d\ln M_2}\right| \frac{\delta_c(t)}{\sigma(M_2)} \frac{1}{(1-\sigma^2(M_2)/\sigma^2(M_1))^{3/2}} \times \exp\left[-\frac{\delta_c(t)^2}{2}\left(\frac{1}{\sigma^2(M_2)} - \frac{1}{\sigma^2(M_1)}\right)\right]. \tag{2.41}$$

This expression was found by Lacey & Cole (1993) and then used to compute the halo-survival times in Lacey & Cole (1994).

2.4 Structure formation in early dark energy models

Up to now, all the models were assumed with the implicit condition that at early times, after the radiation-dominated era, the only important contribution comes from the matter density. In early dark energy models this condition breaks down and all the previous calculations should be done taking into account the early dark energy density.

If early dark energy is included then all the quantities involved in the calculations explicitly depend on the dark energy equation of state. One consequence of considering early dark energy models is an increasing of the expansion rate at early times and therefore a decrease in the linear growth factor. This implies for example that the linear density contrast δ_c is lower than in a ΛCDM model.

As δ_c appears in the mass function, this quantity will be largely affected by the behaviour of the early dark energy; in particular Bartelmann et al. (2006) found that, compared to a ΛCDM model, these models predict more massive halos. This effect occurs when the merger events are studied. Also for the merger rates a similar result is found, due to earlier structure growth, mergers start earlier and are more frequent at higher redshifts than for a cosmological constant model.

The fact that halos form earlier, reflects also on the concentration that will be higher than for a ΛCDM model.
For more detail we refer to Bartelmann et al. (2006).

Chapter 3

Galaxy clusters and their emission

Galaxy clusters are the largest gravitationally bound structures in the universe and therefore, according to the bottom-up model of structure formation, also the last to form. They have masses in the range $10^{14} - 10^{15}\ M_{\odot}$ and a dimension of some Mpc. Approximately $10^{13}\ M_{\odot}$ are in stars, $10^{14}\ M_{\odot}$ in galaxies (including dark matter). Diffuse, hot and ionized baryons are about $10^{14}\ M_{\odot}$ and they constitute the *intracluster medium* (ICM) which emits in the X-ray band via thermal bremsstrahlung with a temperature of the order of $10^{7} \div 10^{8}\ K$. The rest, about 90 %, is dark matter, that interacts only gravitationally with the other forms of matter and it can be considered as non-collisional. Also the motion of the galaxies can be considered non-collisional in the gravitational potential of the cold dark matter, excluding the very central regions.

As said before, galaxy clusters form late ($z \leq 1$), so they could be used to distinguish between different cosmological models. In fact all the models tend to approximate an EdS universe at high redshifts, while they differ substantially at lower and intermediate redshifts. They can also be useful to study the non-linear structure formation, the nature of dark matter, the behaviour of dark energy, the thermal evolution of the universe.

To first approximation, the dynamics of galaxy clusters is ruled by gravity, a powerful tool to study their evolution is the analysis of the density profiles that are the subject of section 3.1, the properties of the ICM and its emission are briefly discussed in section 3.2.

3.1 Density profiles

In this section we briefly describe some of the most common density profiles used to parametrize the mass distribution in clusters.

Clusters can be considered as self-gravitating systems, but they are intrinsically unstable (according to the virial theorem), so any density profile just reflects a long-lived transient period in the life of the galaxy cluster. Due to the high number of objects forming a cluster, it is not possible to study analytically its time evolution, so for a complete description one needs N-body simulations. Nevertheless it is possible to use a statistical approach based on Boltzmann equation or more precisely on the Vlasov equation that represents the collisionless variant of the Boltzmann equation:

$$\frac{\partial f}{\partial t} + \vec{v} \cdot \vec{\nabla}_{\vec{x}} f - \vec{\Phi} \cdot \vec{\nabla}_{\vec{v}} f = 0, \tag{3.1}$$

where f is the particle distribution function in phase space, Φ the gravitational potential and $\vec{v}$ the particle velocity. It is easier to study this equation through its moments, for example the first moment corresponds to the continuity equation, while the second moment leads to the Jeans equation.

Supposing the system is static and with spherical symmetry, the potential has a dependence only on the radial coordinate and the mass enclosed in a sphere of radius r is

$$M(r) = -\frac{r\sigma_r^2(r)}{G}\left[\frac{d\ln\rho(r)}{d\ln r} + \frac{d\ln\sigma_r^2(r)}{d\ln r} + 2\beta(r)\right], \tag{3.2}$$

where $\sigma_r(r)$ is the radial velocity dispersion, $\rho(r)$ the density and $\beta(r) = 1 - \sigma_r^2(r)/\sigma_t^2(r)$ is the ratio between the radial and the tangential velocity dispersion $\sigma_t(r)$. For a purely radial motion $\beta = -\infty$ and for a pure tangential motion $\beta = 1$.

If in equation 3.2 the motion is considered isotropic and isothermal, i.e. $\beta = 0$ and $\sigma_r = const$, then one solution of the resulting differential equation is the singular isothermal

sphere (*SIS*) profile

$$\rho(r) = \frac{\sigma^2}{2\pi G r^2}. \tag{3.3}$$

The profile is divergent in the origin and the total mass resulting from this profile diverges. Despite these problems the SIS profile is very often used to model the mass distribution in galaxy clusters also because has the advantage of reproducing the observed flat rotational curve of galaxies. A better approximate solution to equation 3.2 is the non-singular expression

$$\rho(r) = \frac{\rho_0}{1 + \left(\frac{r}{r_0}\right)^2}, \tag{3.4}$$

where ρ_0 and r_0 are constants and represent the density and the radius of the core.

A rigorous and self-consistent truncated density profile can be obtained using the phase-space density suggested by King (1966), but it is not possible to use simple analytical functions. Therefore it is often used an approximation suggested by King (1962) (*King's profile*):

$$\rho(r) = \frac{\rho_0}{\left[1 + \left(\frac{r}{r_0}\right)^2\right]^{3/2}}. \tag{3.5}$$

Also this profile gives a divergent mass, but it diverges more slowly than the SIS profile.

While the density profiles just described have a physical interpretation, the profile found by numerical simulations fitting the cluster profiles better has not. Using numerical simulated structures, Navarro et al. (1997) (NWF) found that the following profile fits quite accurately the simulated clusters:

$$\rho(r) = \frac{\rho_{crit}\delta_c}{(r/r_s)(1 + r/r_s)^2}, \tag{3.6}$$

where ρ_{crit} is the critical density of the universe at redshift z as defined in equation 1.13,

r_s the scale radius and δ_c is a dimensionless quantity defined as

$$\delta_c = \frac{\Delta_v}{3} \frac{c^3}{[\ln(1+c) - c/(1+c)]}, \tag{3.7}$$

where $c \equiv r_{200}/r_s$ is the concentration parameter and Δ_v was defined in equation 2.31; r_{200} is the radius of a sphere in which the average density is 200 times higher than the critical density. Equation 3.6 is valid in a broad range of masses $3 \times 10^{11} \lesssim M(M_\odot/h) \lesssim 3 \times 10^{15}$. The NFW profile then just depends on one parameter, the mass or the concentration. There are different prescriptions for determining the concentration parameter (see e.g. Navarro et al., 1997; Bullock et al., 2001; Eke et al., 2001). Even if different, the different ways of computing c have in common the fact that concentration increases towards lower mass as consequence of the higher collapse redshift of less massive structures.
The origin of the inner slope is still unclear and other authors suggested steeper slopes (Moore et al., 1998; Jing & Suto, 2000).

Observations of the ICM show that a good profile can be obtained assuming that the gas is relaxing in an already formed potential well. The resulting profile is called β-*profile* (Cavaliere & Fusco-Femiano, 1976, 1978)

$$\rho(r) = \frac{\rho_0}{[1 + (r/r_s)^2]^{3\beta/2}}, \tag{3.8}$$

with $\beta = \frac{\mu m_P \sigma^2}{kT}$, where μ is the mean molecular density of the gas and T the temperature. This profile has as basic assumption that both dark matter and gas follow a static and isothermal distribution and that dark matter follows a King profile. Despite the incomplete fulfillment of the hypothesis, this profile is in very good agreement with what is found via X-ray observations and hydrodynamical simulations.

3.2 Intracluster medium

Because of the baryon catch-up, baryons fall into the potential well of the already collapsed dark matter. Therefore they will be adiabatically compressed and heated also by

shocks thus emitting in the X-ray band via *free-free* emission reaching luminosities of 10^{45} erg/s that allow to find clusters also at relatively high redshifts. For the thermal history of the gas, also radiative cooling is important because it explains the formation of dense and cold gas ($T \lesssim 10^5$ K) that is at the origin of star formation regions.

3.2.1 Sunyaev-Zel'dovich effect

In this section we briefly describe the thermal and kinematic Sunyaev-Zel'dovich (SZ) effects in the non-relativistic approximation.
The thermal SZ (tSZ) effect is due to the inverse Compton scattering between the electrons of the intracluster medium and the CMB photons while the kinematic SZ (kSZ) effect is due to the peculiar motion of the cluster and usually it is an order of magnitude smaller than the tSZ effect.

The tSZ effect distorts the CMB spectrum, in particular at low frequencies the intensity decreases, while at high frequencies the intensity of the spectrum increases (see Fig. 3.1). These distortions in the spectrum intensity can be described as variation of the CMB temperature (Sunyaev & Zeldovich, 1972, 1980a,b, 1981) according to the following relations

$$\frac{\Delta T_{tSZ}}{T_{CMB}} = y\left[\frac{x}{\tanh x/2} - 4\right], \tag{3.9}$$

$$\frac{\Delta T_{kSZ}}{T_{CMB}} = -w, \tag{3.10}$$

where $x = h\nu/kT$ is the dimensionless frequency and y and w are the thermal and kinematic Comptonization parameters whose expressions are

$$y = \frac{k\sigma_T}{m_e c^2}\int dl\, n_e T_e, \tag{3.11}$$

$$w = \frac{\sigma_T}{c}\int dl\, n_e v_r \tag{3.12}$$

where σ_T is the Thomson cross section, T_e the electron temperature, n_e the electron number density and v_r the radial velocity along the line of sight. In the Rayleigh-Jeans regime

$x \ll 1$ and for the tSZ effect $\Delta T/T \approx -2y$. Due to the peculiar frequency dependence of the tSZ effect, for a frequency $\nu \approx 218$ GHz, $\Delta T/T = 0$ and the CMB spectrum is not distorted, so it is possible to study the kSZ effect on CMB.

The total amount of anisotropy induced by the SZ effect on the CMB can be quantified through the integrated SZ (ISZ) effect and it is defined as the integral of y and w over the solid angle

$$Y = \frac{k\sigma_T}{m_e c^2 D_a^2} \int dV \; n_e T_e, \tag{3.13}$$

$$W = \frac{\sigma_T}{c D_a^2} \int dV \; n_e v_r, \tag{3.14}$$

with D_a the angular diameter distance. Assuming both T_e and v_r slowly varying along the line of sight, then the kSZ effect is directly related to the y parameter through the relation

$$\frac{\Delta \, T_{kSZ}}{T} = -v_r \frac{m_e c}{kT} y. \tag{3.15}$$

According to the spherical collapse model discussed in paragraph 2.3.1, the temperature of the gas depends on the mass M and the redshift z of the cluster (Eke et al., 1996a)

$$T_{gas} = T_e = \frac{7.75}{k\beta} \left(\frac{6.8}{5X+3} \right) \left(\frac{M}{10^{15} M_\odot / h} \right)^{2/3} (1+z) \left(\frac{\Omega_{m,0}}{\Omega_m(z)} \right)^{1/3} \left(\frac{\Delta_v}{178} \right)^{1/3}. \tag{3.16}$$

Typical values for the tSZ effect are between 10^{-6} for cold and under-dense regions and 10^{-4} for clusters.

The SZ effect is very important in cosmology because it allows an estimation of the matter distribution as it depends on the electron density and it is approximately independent of redshift, so it can be studied also at early times. From the kinematic effect it is possible to study cluster peculiar velocities that are useful to understand the large scale matter distribution, the thermal effect gives an estimation of the cluster density and of the thermodynamical state of the cluster as it is related to the electron pressure. With the tSZ effect it is possible to infer also a value for H_0, even if more precise techniques are

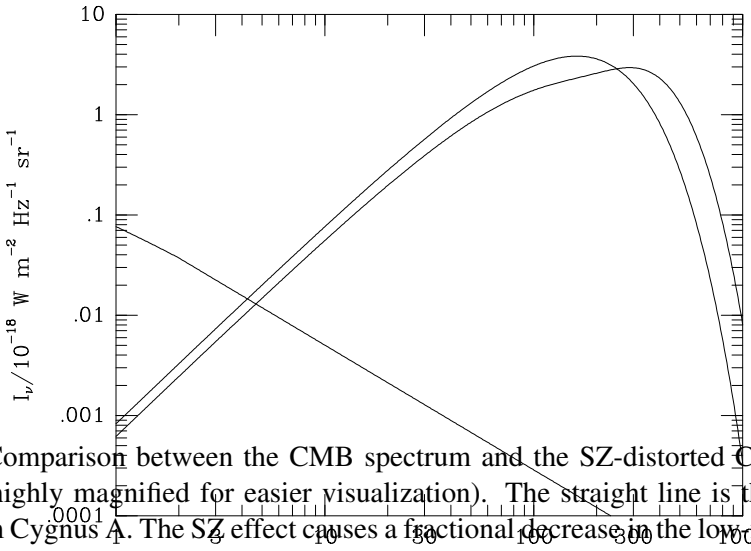

Figure 3.1: Comparison between the CMB spectrum and the SZ-distorted CMB spectrum (the distortion is highly magnified for easier visualization). The straight line is the integrated radio emission from Cygnus A. The SZ effect causes a fractional decrease in the low-frequency intensity of the CMBR that is proportional to y at an increase at high frequency. Figure from Birkinshaw (1999).

available.

More details, both theoretical and observational can be found in several reviews (see e.g. Rephaeli, 1995; Birkinshaw, 1999; Caldwell, 2002; Rephaeli et al., 2005).

3.2.2 X-ray emission

Thanks to the improvements in satellite observations (ROSAT, XMM-Newton, Chandra for X band and Compton Gamma-Ray Observatory (CGRO), SWIFT for γ-band) the diffuse and almost isotropic background radiation in X-ray and γ-bands is resolved in discrete sources.

The discrete X-ray radiation is not the only one contributing to the formation of the X-ray background, but there is also another component, characterized by a continuum emission typical of hot ionized gas given by the interaction between the free electrons and the nuclei. This emission, called *free-free emission*, has an emissivity given by (Eke et al.,

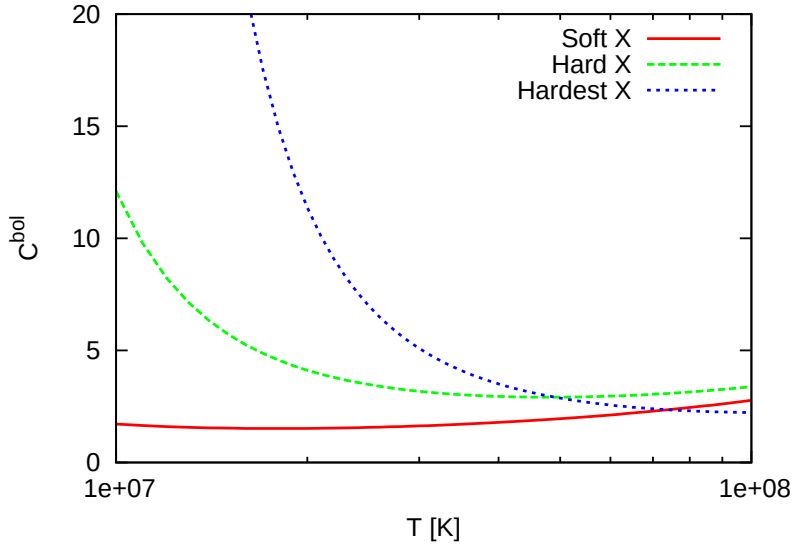

Figure 3.2: Bolometric correction for the three bands described. The red curve shows the bolometric for the soft band ($0.5\,\mathrm{keV} \div 2\,\mathrm{keV}$), the green curve for the hard band ($2\,\mathrm{keV} \div 4\,\mathrm{keV}$) and the blue curve for the hardest band ($4\,\mathrm{keV} \div 10\,\mathrm{keV}$).

1998)

$$\varepsilon_{ff} \approx 1.2 \times 10^{-24} T^{1/2} n_P^2 \; (erg/s/cm^3), \tag{3.17}$$

where T is the gas temperature in keV and n_P the proton density in $\mathrm{g/cm^3}$.

Equation 3.17 gives a value integrated over all frequencies, but to study its contribution to the X-ray band one needs to define how this energy is distributed within a given frequency interval.

For the Bremsstrahlung, the emission spectrum has a frequency dependence of

$$f(\nu) = e^{-h\nu/k_B T} g(\nu, T) \; , \tag{3.18}$$

where $g(\nu, T) = \left(\frac{h\nu}{k_B T}\right)^{-\gamma}$ is the Gaunt factor and $\gamma = Z/Z_\odot$ a parameter depending on the metallicity ($Z \approx 0.3\, Z_\odot$).

Given an energy (frequency) interval [E_1,E_2], the band-function is defined as

$$F_{band}^{[E_1,E_2]}(T) = \int_{x_{1,0}(1+z)}^{x_{2,0}(1+z)} C\, e^{-x} x^{-\gamma} dx\,, \tag{3.19}$$

where $x = E/(kT)$ ($E = h\nu$) and C is a normalization constant defined as $1 = \int_0^\infty C\, e^{-x} x^{-\gamma} dx$. The subscript 0 in the integration boundaries means that the band limits are taken at the observer rest-frame, so the $1+z$ term represents the K-correction.

Knowing the value of F_{band}, the luminosity in a given band is given by the relation $L_{band} = L_X^{bol} F_{band}$, where $L_X^{bol} = \varepsilon_{ff} V$ and V is the volume.

The K-correction is equivalent to a cooling, this implies that, together with the smaller number of dense structures, the emissivity will decrease if the redshift increases.

Usually three bands are considered: soft band ($E_1 = 0.5\,\mathrm{keV}$, $E_2 = 2\,\mathrm{keV}$), hard band ($E_1 = 2\,\mathrm{keV}$, $E_2 = 4\,\mathrm{keV}$) and hardest band ($E_1 = 4\,\mathrm{keV}$, $E_2 = 10\,\mathrm{keV}$).

In figure 3.2 we show the bolometric correction for three bands defined above for systems at redshift $z = 0$. The bolometric correction is defined as the inverse of the band function. The emission in the soft band is always higher than the hard band while the emission in the hardest band dominates only for very high temperatures.

Chapter 4

Gravitational lensing

In this chapter we review the foundations of gravitational lensing.
According to general relativity, light propagates on the null geodesics of the space-time. Solving the full equations for an arbitrary curved space-time is too complex because of the non-linearity of the relativistic equations. However, in cosmology, simplified assumptions are considered and a much simpler approximate description of photon trajectories is possible. This approximated analysis is known as *gravitational lensing theory*.
To be applied, gravitational lensing theory requires that the dimensions of the objects acting as lenses are much smaller than the line-of-sight distance between the source and the observer (*thin screen approximation*). If mass is distributed on cosmological scales along the line-of-sight, then a more general description is required. In addition to this, another assumption is considered, namely the weakness of the gravitational field of the lens $\Phi \ll c^2$ and $v_{lens} \ll c$. These assumptions are very well justified in all the cases of astrophysical interests, they break down only in proximity of compact objects.

According to gravitational lensing theory, the travel of photons can be subdivided into three parts: a first part from the source to the massive objects (*lens*) where the light rays travel in an unperturbed space-time, a second part where they are deflected by the gravitational field of the lens and the last part from the lens to the observer where they travel again in an unperturbed space-time. The amount and the direction of the deflection depend on the mass distribution of the lens and on the impact vector of the light rays.
Here we just refer to the concepts and equations relevant for the present work. A broader

and more exhaustive treatment of gravitational theory can be found in the books by Schneider et al. (1992, 2006) and in the reviews by Narayan & Bartelmann (1996), Bartelmann & Schneider (2001) and Wambsganss (1998).

4.1 Deflection angle

In presence of the gravitational field Φ of the lens, the perturbed Minkowski metric is

$$ds^2 = \left(1 + \frac{2}{c^2}\Phi\right) c^2\, dt^2 - \left(1 - \frac{2}{c^2}\Phi\right)(dx^2 + dy^2 + dz^2). \tag{4.1}$$

As light follows null geodesics, $ds^2 = 0$ and light will propagate with an effective speed

$$c' \approx c\left(1 + \frac{2}{c^2}\Phi\right), \tag{4.2}$$

this means that in a gravitational field light propagates more slowly than in an empty space because of the effect of the curvature of the space-time geometry. This effect can be expressed in terms of an optical description introducing the *diffraction index* (Schneider et al., 1992):

$$n = \frac{c}{c'} = 1 + \frac{2}{c^2}|\Phi| > 1. \tag{4.3}$$

Due to the slowing down, a time delay in the propagation of light arises as a consequence of the presence of the perturbing gravitational field. The total amount of the time delay (called *Shapiro delay* (Shapiro, 1964)) is given by

$$\Delta t = \int_o^s \frac{2}{c^3}|\Phi| dl, \tag{4.4}$$

the time delay will be larger closer to the lens because of the deeper potential well through which lights propagate.

In complete analogy with optics, light passing near a massive object will be deflected from the straight line and the amount of deflection depends on the diffraction index. The

deflection angle is given by

$$\vec{\hat{\alpha}} = -\int \nabla_{\perp} n \, dl = \frac{2}{c^2} \int \nabla_{\perp} \Phi \, dl. \tag{4.5}$$

For a point mass lens with mass M, the deflection angle is $\hat{\alpha}(\xi) = \frac{4GM}{c^2 \xi}$. This expression can be generalized to a general lens using the *thin lens approximation* according to which, considering extended object with a size small compared to the distances involved, the deflection arises only along a short section of the light path and the three-dimensional matter distribution ρ can be projected along the line of sight and the lens is approximated with a two-dimensional matter distribution, called *lens plane*. A lens with a projected mass density

$$\Sigma(\vec{\xi}) = \int \rho(\vec{\xi}, z) dz, \tag{4.6}$$

where $\vec{\xi}$ is the vector in physical units on the lens plane, will give rise to a deflection angle

$$\vec{\hat{\alpha}}(\vec{\xi}) = \frac{4G}{c^2} \int \frac{\Sigma(\vec{\xi}')(\vec{\xi} - \vec{\xi}')}{|\vec{\xi} - \vec{\xi}'|^2} d^2\xi'. \tag{4.7}$$

The geometry of a typical lensing system is shown in figure 4.1

Introducing angular coordinates on the lens plane, $\vec{\xi} = D_l \vec{\theta}$ where D_l is the angular diameter distance of the lens from the observer, and introducing the reduced deflection angle $\vec{\alpha} = \vec{\hat{\alpha}} D_{ls}/D_s$ where D_{ls} and D_s are respectively the angular diameter distance between the lens and the source and between the source and the observer, equation 4.7 becomes

$$\vec{\alpha}(\vec{\theta}) = \frac{4G}{c^2} \frac{D_l D_{ls}}{D_s} \int \frac{\Sigma(\vec{\theta}')(\vec{\theta} - \vec{\theta}')}{|\vec{\theta} - \vec{\theta}'|^2} d^2\theta'. \tag{4.8}$$

The *critical surface mass density* is defined as

$$\Sigma_{crit} \equiv \left(\frac{4G}{c^2} \frac{D_l D_{ls}}{D_s} \right)^{-1} \tag{4.9}$$

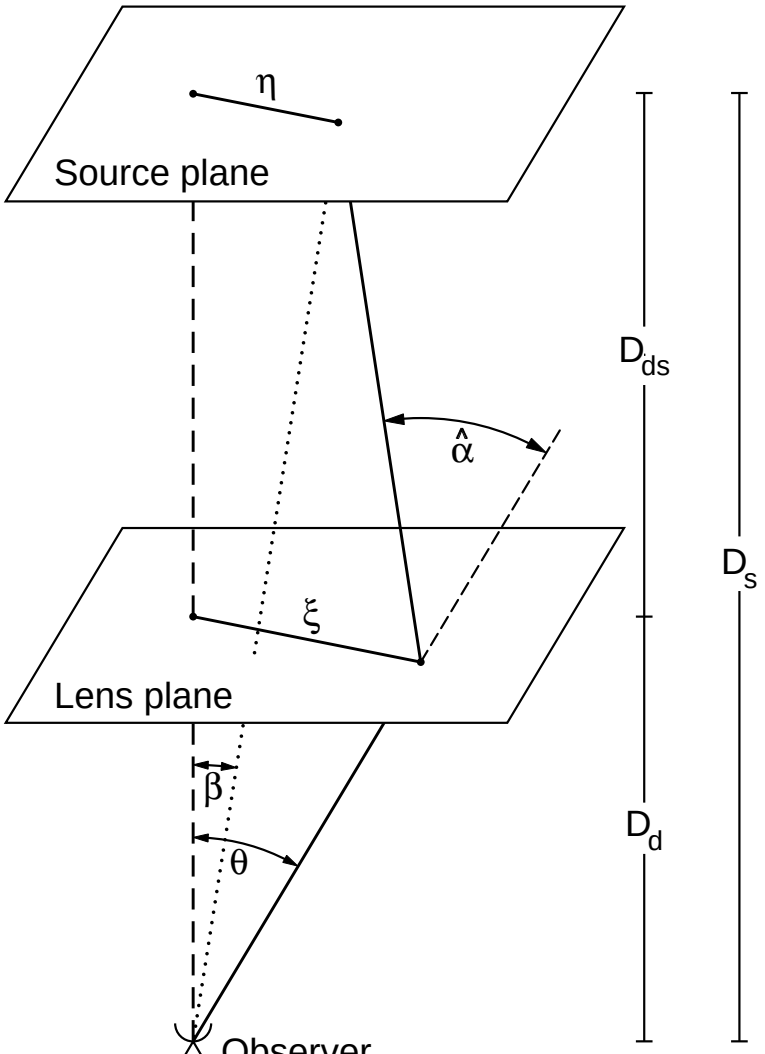

Figure 4.1: Illustration of a typical gravitational lensing system. The angles are exaggerated for better understanding. Figure taken from Bartelmann & Schneider (2001)

and the *convergence* as

$$\kappa(\vec{\theta}) \equiv \frac{\Sigma(\vec{\theta})}{\Sigma_{crit}}. \tag{4.10}$$

The distance combination $D_{eff} = D_l D_{ls}/D_s$ acts as a lensing efficiency function, approaching zero close to the source and the observer and it has a maximum roughly in the middle. The redshift dependence of the lensing effective distance $D_{eff}(z)$ is shown in

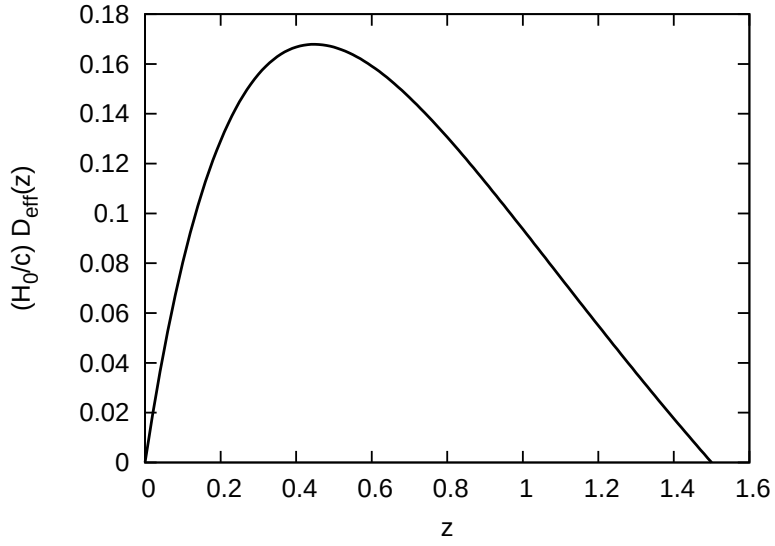

Figure 4.2: Lensing efficiency distance for a ΛCDM model as a function of redshift of the lens for a source at redshift $z_s = 1.5$.

figure 4.2.

Using equations 4.9 and 4.10, the reduced deflection angle definition reduces to

$$\vec{\alpha}(\vec{\theta}) = \frac{1}{\pi}\int \kappa(\vec{\theta}')\frac{\vec{\theta}-\vec{\theta}'}{|\vec{\theta}-\vec{\theta}'|^2}d^2\theta'. \tag{4.11}$$

4.1.1 Lens equation

From figure 4.1 it is possible to derive the fundamental equation of gravitational lensing. It is easy to see that the following relation holds (in the approximation that $\vec{\beta}$, $\vec{\theta}$, $\vec{\alpha} \ll 1$):

$$\vec{\beta} = \vec{\theta} - \frac{D_s}{D_d}\vec{\alpha}(\vec{\theta}) \equiv \vec{\theta} - \vec{\alpha}(\vec{\theta}), \tag{4.12}$$

where $\vec{\beta}$ is the angular position on the source plane, $\vec{\theta}$ the angular position on the lens plane and $\vec{\alpha}$ is the reduced deflection angle as defined above. Equation 4.12 is called *lens equation*. This equation is non linear, so it can have more than one solution, that is the lens can create multiple images of the source. For this to happen, the lens should be strong, and this is quantified by the convergence κ: if a lens has in some point $\kappa \geq 1$, then

it can produce multiple images. This a sufficient but not necessary condition.

4.2 Lensing potential

An extended lens can be characterized by the *effective lensing potential*, the projected and rescaled Newtonian potential

$$\Psi(\vec{\theta}) = \frac{2}{c^2}\frac{D_{ls}}{D_l D_s}\int \Phi(D_l\vec{\theta}, z)dz. \tag{4.13}$$

The lensing potential has the properties that its gradient is the reduced deflection angle

$$\vec{\nabla}_{\vec{\theta}}\Psi(\vec{\theta}) = \vec{\alpha}, \tag{4.14}$$

and its Laplacian is twice the convergence

$$\nabla^2\Psi(\vec{\theta}) = 2\kappa(\vec{\theta}). \tag{4.15}$$

The inversion of equation 4.15 allows to write the lensing potential as a convolution of the convergence with the Green's function of the two-dimensional Laplacian:

$$\Psi(\vec{\theta}) = \frac{1}{\pi}\int \kappa(\vec{\theta}')\ln|\vec{\theta}-\vec{\theta}'|d^2\theta \tag{4.16}$$

4.3 Magnification and distortion

Because of Liouville's theorem and the conservation of the physical number of photons, gravitational lensing conserves the surface brightness. One of the main properties of gravitational lensing is the distortion of the images that becomes evident if they are extended. If the size of the sources is smaller than the angular scale on which the physical properties of the lens change, than the lensing equation can be locally linearized

$$\vec{\beta} = \vec{\theta} - \vec{\alpha}(\vec{\theta}) \approx \vec{\beta}_0 - \frac{\partial\vec{\beta}}{\partial\vec{\theta}}(\vec{\theta}-\vec{\theta}_0). \tag{4.17}$$

The local properties of the lens mapping are described by the Jacobian matrix $\mathcal{A}$

$$\mathcal{A}(\vec{\theta}) \equiv \frac{\partial \vec{\beta}}{\partial \vec{\theta}} = \left(\delta_{i,j} - \frac{\partial^2 \Psi(\vec{\theta})}{\partial \theta_i \partial \theta_j} \right) = \mathcal{M}^{-1}, \tag{4.18}$$

where $\mathcal{M}^{-1}$ is the magnification tensor, this holds because the solid angle element $\delta\beta^2$ of the source is mapped into the solid angle element $\delta\theta^2$. From now on we indicate $\frac{\partial \Psi}{\partial \theta_i}$ as Ψ_i.

The Jacobian matrix can be written as

$$\mathcal{A} = \begin{pmatrix} 1-\kappa-\gamma_1 & -\gamma_2 \\ -\gamma_2 & 1-\kappa+\gamma_1 \end{pmatrix} \tag{4.19}$$

where κ is the convergence and

$$\gamma_1 = \frac{1}{2}(\Psi_{11} - \Psi_{22}) = \gamma \cos(2\phi) \tag{4.20}$$

$$\gamma_2 = \frac{1}{2}(\Psi_{12} + \Psi_{21}) = \gamma \sin(2\phi), \tag{4.21}$$

are the two components of the complex shear tensor $\gamma = \gamma_1 + i\gamma_2$.

The effect of the convergence is to scale the dimensions of the source and the effect of the shear is to distort the shape of the source. This is shown in figure 4.3.

The magnification μ of the source is given by the determinant of the tensor $\mathcal{M}$, $\mu = [(1-\kappa)^2 - \gamma^2]^{-1}$. Where the determinant of $\mathcal{A}$ vanishes, *critical curves* occur on the lens plane and these are mapped into *caustics* on the source plane. In real situations magnification does not diverge, but it reaches very high values and images are highly distorted.

4.4 Flexion

Up to now we just considered the effects of lensing to first order. If the convergence and the shear are not constant in the field, than it is useful to go on with the Taylor expansion up to the second order. Indicating with $\vec{\theta}'$ and $\vec{\theta}$ the unlensed and lensed coordinates, the

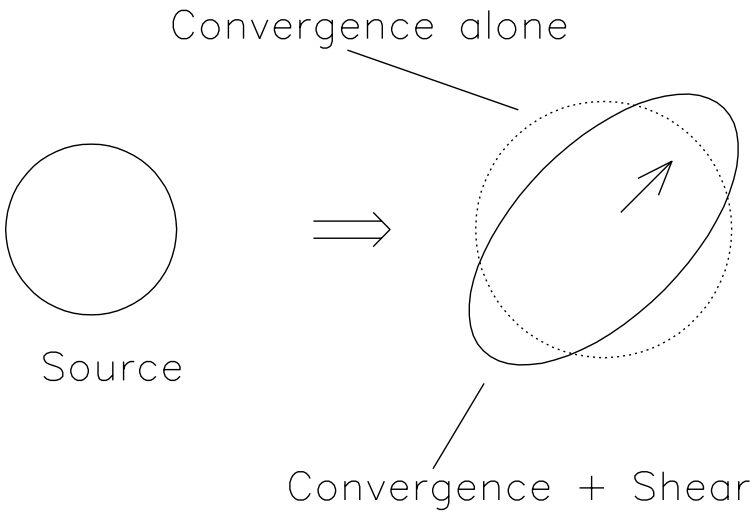

Figure 4.3: Illustration of the effect of the convergence and on the shear on a circular source. Figure taken from Narayan & Bartelmann (1996).

Jacobian can be written as $\mathcal{A} = \frac{\partial\vec{\theta}'}{\partial\vec{\theta}}$ and expanding $\vec{\theta}'$ to the second order, equation 4.17 becomes

$$\vec{\theta}' \simeq \vec{\theta}'_0 + \frac{\partial\vec{\theta}'}{\partial\vec{\theta}}(\vec{\theta}' - \vec{\theta}'_0) + \frac{1}{2}\frac{\partial^2\vec{\theta}'}{\partial\vec{\theta}^2}(\vec{\theta}' - \vec{\theta}'_0)^2 \tag{4.22}$$

Introducing the tensor $D \equiv \frac{\partial^2\vec{\theta}'}{\partial\vec{\theta}^2}$, equation 4.22 reads now

$$\theta'_i \simeq \mathcal{A}_{ij}\theta_j + \frac{1}{2}D_{ijk}\theta_j\theta_k \tag{4.23}$$

with $D_{ijk} = \partial_k\mathcal{A}_{ij}$. As the Jacobian matrix is proportional to the second derivative of the lensing potential, the tensor D will be proportional to the third derivative of the lensing

potential. Using the results of Kaiser (1995), it can be shown that

$$D_1 = \begin{pmatrix} -2\gamma_{1,1} - \gamma_{2,2} & -\gamma_{2,1} \\ -\gamma_{2,1} & -\gamma_{2,2} \end{pmatrix} \quad \text{and} \quad D_2 = \begin{pmatrix} -\gamma_{2,1} & -\gamma_{2,2} \\ -\gamma_{2,2} & 2\gamma_{1,2} - \gamma_{2,1} \end{pmatrix}. \tag{4.24}$$

From the matrices above defined, it is possible to construct two complex quantities, the *first flexion* F and the *second flexion* G:

$$F = F_1 + \mathrm{i}F_2 = (\gamma_{1,1} + \gamma_{2,2}) + \mathrm{i}(\gamma_{2,1} - \gamma_{1,2}) \tag{4.25}$$

$$G = G_1 + \mathrm{i}G_2 = (\gamma_{1,1} - \gamma_{2,2}) + \mathrm{i}(\gamma_{2,1} + \gamma_{1,2}). \tag{4.26}$$

It is also possible to show that $\vec{F} = \nabla\kappa$ and $\vec{G} = \nabla\gamma$, so the first flexion can be used to obtain the convergence field and the second flexion the shear field.

The flexion is responsible for introducing a curvature and other higher-order distortions in the images.

The effects of the convergence, the shear and the flexion on a Gaussian image are shown in figure 4.4. The convergence κ, a spin-0 field, just rescales the dimension of the image, the first flexion F, a spin-1 field, leads to a skewness, the shear γ, a spin-2 field, distorts the shape of the image and the second flexion G, a spin-3 field, leads to a threefold shape. More details on the formalism and the applications of the flexion can be found in Goldberg & Bacon (2005) and Bacon et al. (2006).

4.5 Weak cosmological lensing

Gravitational lensing shows two regimes, *strong lensing* when $\kappa > 1$ and *weak lensing* when $\kappa < 1$. Strong lensing is characterized by strong magnifications, high distortions and sometimes the formations of arcs and multiple images. In the weak lensing regime it is only possible to determine the statistical properties of the lensing system by averaging over the field of view because distortions and magnifications are tiny.

As the number density of distant galaxies is high (ranging from 10-20 galaxies per square

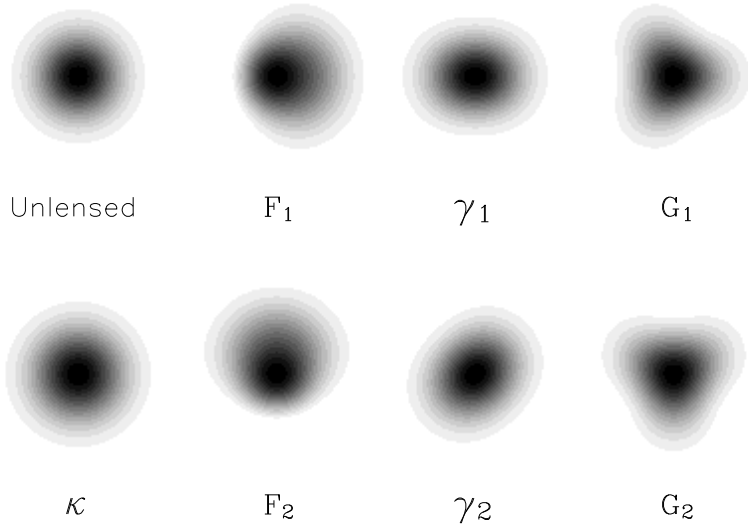

Figure 4.4: Weak lensing distortions on an unlensed gaussian galaxy with radius $\theta = 1''$ with 10% convergence/shear and 0.28 arcsec^{-1} flexion. The flexion values are high for visualization purposes. Figure from Bacon et al. (2006).

arc-minute for ground-based observations to 80-100 galaxies per square arc-minute with space-based observations galaxy clusters distort the background galaxies in a very characteristic way. This is the subject of the next section.

4.5.1 Lensing on background galaxies

Source sizes are unknown individually but it is possible to measure source shapes that, although intrinsically irregular, can be averaged due to the high number of sources. Assuming background galaxies are randomly oriented, the average over their shapes is expected to be circular. In the weak lensing regime a circular source of radius r appears to be elliptical with axes $a = \frac{r}{1-\kappa-\gamma}$ and $b = \frac{r}{1-\kappa+\gamma}$. The ellipiticity ε is defined as

$$\varepsilon = \frac{a-b}{a+b} = \frac{\gamma}{1-\kappa} = g \tag{4.27}$$

where g is the reduced shear. Equation 4.27 shows that the reduced shear is an estimator of the ellipticity and $\langle\varepsilon\rangle = \langle\gamma\rangle$ if the ellipticities are averaged over a large sample, this is

because, assuming the galaxies are randomly oriented, their averaged intrinsic ellipticity vanishes.

The intrinsic (ε_s) and observed (ε) ellipticities are related by the following relation:

$$\varepsilon = \begin{cases} \frac{\varepsilon_s + g}{1 + g^* \varepsilon_s} & |g| \leq 1 \\ \frac{1 + g \varepsilon_s^*}{\varepsilon_s^* + g^*} & |g| > 1 \end{cases} \tag{4.28}$$

where the asterisk denotes the complex conjugate.

The intrinsic ellipticities follow a distribution approximated by

$$p(|\varepsilon_s|) = \frac{\exp|(1 - |\varepsilon_s|^2)/\sigma_{\varepsilon_s}^2|}{\pi \sigma_{\varepsilon_s}^2 |\exp(1/\sigma_{\varepsilon_s}^2) - 1|}, \tag{4.29}$$

where $\sigma_{\varepsilon_s} = 0.3$.

4.5.2 Light propagation in an inhomogeneous universe

Given a homogeneous and isotropic universe, light propagates along the null geodesics, but now it is necessary to take into account that the dimensions of the lenses can be comparable with the curvature scale of the universe. Several authors, as Zel'dovich (1964), Gunn (1967), Bartelmann & Schneider (1991) and Kaiser (1992), studied light propagation in an inhomogeneous universe. Non-linear effects were included by Jain & Seljak (1997) and Bernardeau et al. (1997). For a review we refer to Bartelmann & Schneider (2001).

The equation describing the propagation of thin light bundles through arbitrary space-times is the *geodesic deviation equation*

$$\frac{d^2 \vec{\xi}}{d\lambda^2} = \mathcal{J} \vec{\xi}, \tag{4.30}$$

where $\vec{\xi}$ is the transverse physical separation and $\mathcal{J}$ is the *optical tidal matrix* which describes the influence of the space-time curvature on the propagation of light and $d\lambda = -cadt$. The optical tidal matrix

$$\mathcal{J} = \begin{pmatrix} \mathcal{R}(\lambda) + \mathbf{R}[\mathcal{F}(\lambda)] & \mathbf{I}[\mathcal{F}(\lambda)] \\ \mathbf{I}[\mathcal{F}(\lambda)] & \mathcal{R}(\lambda) - \mathbf{R}[\mathcal{F}(\lambda)] \end{pmatrix} \tag{4.31}$$

is symmetric and its components depend on the curvature of the space-time, $\mathbf{R}(z)$ and $\mathbf{I}(z)$ are the real and imaginary parts of a complex number z, $\mathcal{R}(\lambda)$ is the *source of convergence* and $\mathcal{F}(\lambda)$ is the *source of shear*. Replacing the affine parameter λ by the comoving distance, equation 4.30 becomes very simple

$$\frac{d^2\vec{x}}{dw^2} + K\vec{x} = 0, \tag{4.32}$$

where K is the spatial curvature as defined in equation 1.14 and $\vec{x} = \vec{\xi}a^{-1}$ the comoving separation vector. Solutions of equation 4.32 are trigonometric or hyperbolic functions, according to the value of K. Given the initial conditions

$$\vec{x}|_{w=0} = \vec{0}, \;\; \left.\frac{d\vec{x}}{dw}\right|_{w=0} = \vec{\theta}, \tag{4.33}$$

the solutions of equation 4.32 are

$$\vec{x}(\vec{\theta}, w) = f_K(w)\vec{\theta}, \tag{4.34}$$

and $f_K(w)$ is given by

$$f_K(w) = \begin{cases} \frac{1}{\sqrt{K}}\sin(\sqrt{K}w) & K = 1 \\ w & K = 0 \\ \frac{1}{\sqrt{-K}}\sinh(\sqrt{-K}w) & K = -1 \end{cases}. \tag{4.35}$$

Equation 4.32 holds in an unperturbed space-time, to add perturbations two assumptions are taken into consideration: the gravitational field is weak and the density perturbations are localized. This implies that the light rays are deflected according to the equation

$$\frac{d^2\vec{x}}{dw^2} = -\frac{2}{c^2}\nabla_\perp \Phi(\vec{x}, w), \tag{4.36}$$

where the right-hand term represents the contribution from the local inhomogeneity, so the geodesic deviation equation becomes

$$\frac{d^2\vec{x}}{dw^2} + K\vec{x} = -\frac{2}{c^2}\Delta\left\{\nabla_\perp \Phi\left[\vec{x}(\vec{\theta}, w), w\right]\right\}, \tag{4.37}$$

where the difference on the right-hand side has to be evaluated between two light rays having comoving separation $\vec{x}(\vec{\theta}, w)$ at comoving distance w from the observer. The solution of equation 4.37 is given by the sum of the solution of the homogeneous equation and the convolution of its Green's function with the inhomogeneous source term

$$\vec{x}(\vec{\theta}, w) = f_K(w)\vec{\theta} - \frac{2}{c^2}\int_0^w dw' f_K(w-w')\Delta\left\{\nabla_\perp \Phi\left[\vec{x}(\vec{\theta}, w), w\right]\right\}, \tag{4.38}$$

and the integral has to be evaluated along the true photon paths. To actually compute this integral, the *Born approximation* for small scattering angles is used and it is given by the relation

$$\frac{|\vec{x}(\vec{\theta}, w') - f_K(w')\vec{\theta}|}{|f_K(w')\vec{\theta}|} \ll 1, \tag{4.39}$$

and in the integrand $\vec{x}(\vec{\theta}, w')$ can be replaced by $f_K(w')\vec{\theta}$.
An important consequence of the Born approximation is that the Jacobian matrix remains symmetric also in the case of cosmological weak lensing, but in a general multiple lens-plane this is no longer true (see Schneider et al., 1992).

4.5.3 Effective deflection angle and effective convergence

The *effective deflection angle* and the *effective convergence* can be defined in analogy as before. The effective deflection angle is defined as the difference at the distance w between the separation vector of two light rays propagating through an unperturbed space-time, $\vec{x}'(\vec{\theta}, w) = f_K(w)\vec{\theta}$ and the comoving separation vector of the perturbed light rays, $\vec{x}(\vec{\theta}, w)$, divided by the angular diameter distance to w:

$$\vec{\alpha}(\vec{\theta}, w) = \frac{f_k(w)\vec{\theta} - \vec{x}(\vec{\theta}, w)}{f_K(w)} = \frac{2}{c^2}\int_0^w dw' \frac{f_K(w-w')}{f_K(w)}\nabla_\perp \Phi[f_K(w')\vec{\theta}, w']. \tag{4.40}$$

In analogy to the convergence κ, an effective convergence $\kappa_{eff}(w)$ is defined by:

$$\kappa_{eff}(\vec{\theta},w) = \frac{1}{2}\nabla_{\vec{\theta}}\cdot\vec{\alpha}(\vec{\theta},w) = \tag{4.41}$$

$$= \frac{1}{c^2}\int_0^w dw' \frac{f_K(w-w')f_K(w')}{f_K(w)}\nabla^2_{\vec{x}}\Phi[f_K(w')\vec{\theta},w'], \tag{4.42}$$

where the Laplacian is two-dimensional. Poisson's equation relates the three-dimensional Laplacian of the potential to the density contrast $\nabla^2\Phi = \frac{3H_0^2\Omega_0}{2a}\delta$ and supposing that the derivative along the third dimension ($\partial^2\Phi/\partial z^2$) averages to zero (approximation verified with numerical simualtions by White & Hu (2000)), the expression for the effective convergence becomes

$$\kappa_{eff}(\vec{\theta},w) = \frac{3H_0^2\Omega_0}{2c^2}\int_0^w dw' \frac{f_K(w-w')f_K(w')}{f_K(w)}\frac{\delta[f_K(w')\vec{\theta},w']}{a(w')}. \tag{4.43}$$

Equation 4.43 gives the effective convergence in case of a fixed source redshift placed at a comoving distance w; when the sources are distributed in comoving distance (in redshift) the effective convergence needs to be averaged over the normalized source-distance distribution $G(w)$

$$\bar{\kappa}_{eff} = \frac{3H_0^2\Omega_0}{2c^2}\int_0^{w_H} dw \bar{W}(w) f_K(w)\frac{\delta[f_K(w)\vec{\theta},w]}{a(w)}, \tag{4.44}$$

where w_H is the horizon distance and $\bar{W}(w)$ is given by

$$\bar{W}(w) \equiv \int_w^{w_H} dw' G(w')\frac{f_K(w'-w)}{f_K(w')}. \tag{4.45}$$

4.5.4 Power spectra and correlation functions

While cosmological density perturbations refer to a three-dimensional space, lensing quantities are defined in a two-dimensional space (the sky), so a relation between the three-dimensional power spectrum and its two-dimensional projection is needed. In particular we will find a relation between the density contrast power spectrum and the power spectrum of some lensing quantities.

The *two-point correlation function* or auto-correlation function of a possibly complex function $g(\vec{x})$ is defined as

$$\xi_{gg}(|\vec{x}-\vec{y}|) = \langle g(\vec{x}) g^*(\vec{y}) \rangle \tag{4.46}$$

and the Fourier transform of $g(\vec{x})$ is

$$\hat{g}(\vec{k}) = \int d^n x \; g(\vec{x}) e^{\mathrm{i}\vec{k}\vec{x}}. \tag{4.47}$$

Indicating with $g(\vec{\theta})$ the weighted projection of the three-dimensional density contrast

$$g(\vec{\theta}) = \int_0^{w_H} q(w) \delta[f_K(w)\vec{\theta}, w], \tag{4.48}$$

where $q(w)$ is the weight function and inserting its Fourier transform into the correlation function of $g(\vec{\theta})$ we find

$$\begin{aligned} \xi_{gg}(|\vec{\theta}-\vec{\theta}'|) = \int dw \, q(w) \int dw' \, q(w') \int \frac{d^3k}{(2\pi)^3} \int d^3k' (2\pi)^3 \langle \hat{\delta}(\vec{k}, w) \hat{\delta}(\vec{k}', w') \rangle \\ \exp(-\mathrm{i} f_K(w) \vec{k}_\perp \cdot \vec{\theta}) \exp(\mathrm{i} f_K(w) \vec{k}'_\perp \cdot \vec{\theta}') \exp(-\mathrm{i} k_s w) \exp(\mathrm{i} k'_s w'), \end{aligned} \tag{4.49}$$

where the vector $\vec{k}$ has been split up into a parallel component k_s and a perpendicular component $\vec{k}_\perp$ to the line of sight. Replacing the average with the power spectrum (see eq. 2.21) and carrying on the integral over k_s leads to the following expression for the correlation function

$$\xi_{gg}(\phi) = \int dw q^2(w) \int \frac{k dk}{2\pi} P_\delta(k) J_0[f_K(w)\phi k], \tag{4.50}$$

where $\phi = |\vec{\theta}-\vec{\theta}'|$ and $J_0(x)$ is the Bessel function of the first kind. So the power spectrum for the projected quantity $g(\vec{\theta})$ is

$$\begin{aligned} P_g(l) &= \int d\phi \xi_{gg} \exp(\imath \vec{l} \cdot \vec{\phi}) & (4.51) \\ &= \int dw \frac{q(w)^2}{f_K^2(w)} P_\delta \left(\frac{l}{f_K(w)}, w \right). & (4.52) \end{aligned}$$

This approximate equality goes under the name of *Limber's equation* (Limber, 1953). Using Limber's equation with the weight function

$$q(w) = \frac{3H_0^2\Omega_0}{2ac^2} W(w) f_K(w), \tag{4.53}$$

the power spectrum and the correlation function for the effective convergence are

$$P_k(l) = \frac{9H_0^4\Omega_0^2}{4c^4} \int_0^{w_s} dw \frac{W^2(w)}{a^2(w)} P_\delta \left(\frac{l}{f_K(w)}, w \right) \tag{4.54}$$

$$\xi_k(\phi) = \int_0^\infty \frac{l dl}{2\pi} P_k(l) J_0(l\phi). \tag{4.55}$$

Trasforming into the Fourier space these relations hold: $P_k(l) = P_\gamma(l)$, $P_{\vec{\alpha}} = \frac{4}{l^2} P_k(l)$, $P_F(l) = P_G(l) = l^2 P_k(l)$ and $P_\Phi(l) = \frac{4}{[l(l+1)]^2} P_k(l)$.

4.5.5 Multiple lens plane theory

All the equations relative to the light deflection by a single lens plane derived before can be easily extended to the general case in which, between the observer and the source, the matter distribution is discretized into several lens planes.

The lens planes are perpendicular to the line-of-sight and the distance between two planes is much larger than the distance of two potential wells in the planes. The approach of multiple lens planes allows a great simplifications in the calculations of gravitational lensing: as in the single lens plane case, light feels the gravitational potential only on the lens plane and before and after it, light rays propagate on a straight line. This implies that all lensing quantities can be found iterating the previous derived equations.

In the following we will consider N lens planes, $i = 1 \div N$, with angular diameter distance $D_i(a_i)$ and ordered in such a way that if $i < j$ then $a_i > a_j$. We will also assume that the sources lie on the $(N+1)$-th plane and we indicate with D_s the angular diameter distance of the source from the observer. More details can be found in Schneider et al. (1992).

Lens equation

Following Schneider et al. (1992) we define $\vec{\xi}_i$ as the position of the light ray on each single plane i, $\vec{\alpha}_i$ the deflection angle caused by the i-th lens plane and with $\vec{\eta}$ the position on the source plane.
According to figure 4.5, the following relation holds:

$$\vec{\eta} = \frac{D_s}{D_1}\vec{\xi}_1 - \sum_{i=1}^{N} D_{is}\vec{\alpha}_i(\vec{\xi}_i), \tag{4.56}$$

where D_{is} are the angular diameter distances between the lens planes i and the source plane.

The impact vectors $\vec{\xi}_i$ on each lens plane are given by

$$\vec{\xi}_i = \frac{D_i}{D_1}\vec{\xi}_1 - \sum_{k=1}^{i-1} D_{ki}\vec{\alpha}_k(\vec{\xi}_k), \tag{4.57}$$

where D_{ki} represent the angular diameter distances between the k-th and i-th lens planes. It is more convenient to work with dimensionless quantities and with the lensing potential of each lens plane.
Introducing, as before, the reduced deflection angle $\vec{\alpha} = \frac{D_{is}}{D_s}\vec{\alpha}_i$, the multiple lens plane equation 4.57 becomes

$$\vec{\theta}_i = \vec{\theta}_1 - \sum_{k=1}^{i-1} \frac{D_{ki}D_s}{D_i D_{ks}}\vec{\alpha}_i(\vec{\theta}_i), \tag{4.58}$$

where the approximation $\vec{\theta}_i = \vec{\xi}_i/D_i$ was used. A more practical expression can be obtained if, instead of the angular diameter distance, comoving distances are used (because of their additive property) and the reduced deflection angle is replaced by the effective potential. The angular diameter distance is related to the comoving distance by $D_{ang}(a,a_0) = a f_K(w(a))$ and $\vec{\alpha} = f_K(w(a))\nabla_{\vec{x}}\Psi$ where $\vec{x}$ is the comoving orthogonal distance on the lens plane and Ψ the lensing potential. With these substitutions, equation

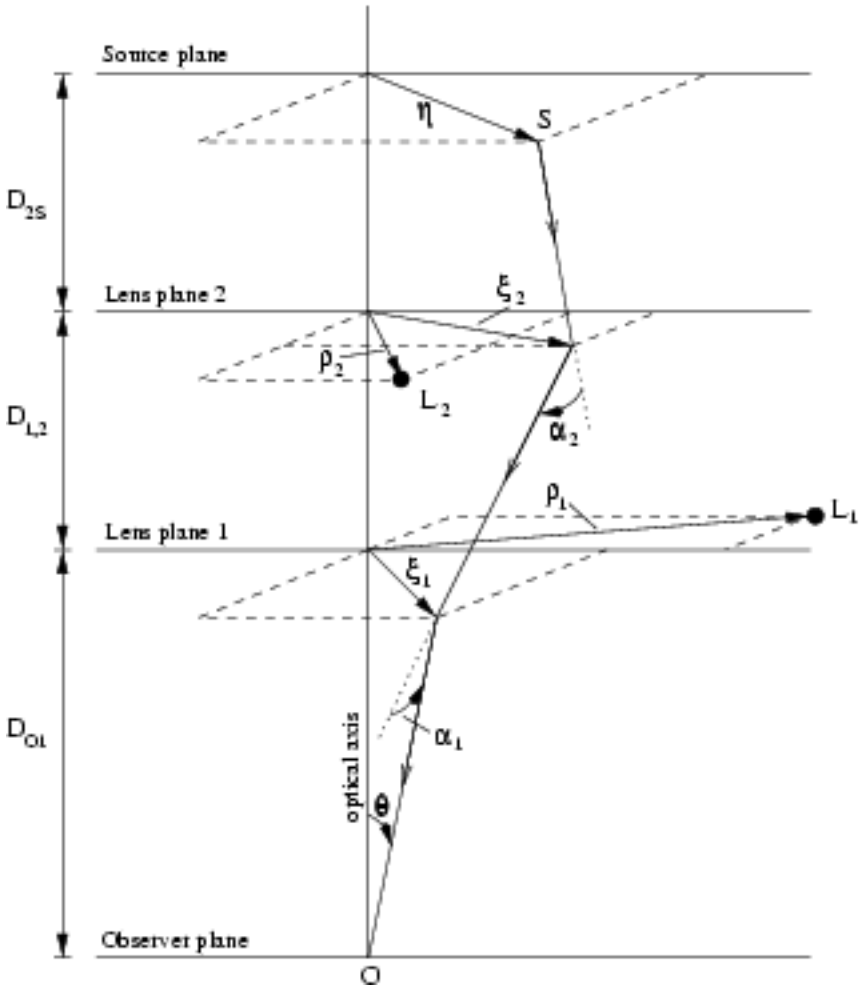

Figure 4.5: Positions and trajectories of the light rays for a two-lens-planes system. From http://www.strw.leidenuniv.nl/~rijkhors/pmwiki/index.php?n=Research.ThickGravitationalLenses.

4.58 becomes

$$\vec{\theta}_i = \vec{\theta}_1 - \sum_{k=1}^{i-1} \frac{f_K(w_i - w_k)}{f_K(w_i)a_k} \nabla_{\vec{x}} \tilde{\Psi}(\vec{x}), \tag{4.59}$$

where $\tilde{\Psi}(\vec{x})$ is the unscaled lensing potential, defined as the projection of the Newtonian potential along the line of sight.

Jacobian matrix

For each lens plane two matrices are defined, the Jacobian matrix $\mathcal{A}_i \equiv \frac{\partial\vec{\theta}_i}{\partial\vec{\theta}_1}$ and the tidal matrix $\mathcal{U}_i \equiv \frac{\partial\vec{\alpha}_i}{\partial\vec{\theta}_i}$, so from equation 4.58 the following recursive relation follows:

$$\mathcal{A}_i = I - \sum_{k=1}^{i-1} \frac{D_{ki}D_s}{D_i D_{ks}} \mathcal{U}_k \mathcal{A}_k, \tag{4.60}$$

that, using as before comoving angular diameter distances and the unscaled lensing potential, becomes

$$\mathcal{A}_i = I - \sum_{k=1}^{i-1} \frac{f_K(w_k) f_K(w_i - w_k)}{f_K(w_i) a_k} \tilde{\mathcal{U}}_k \mathcal{A}_k, \tag{4.61}$$

where

$$\tilde{\mathcal{U}}_k \equiv \begin{pmatrix} \tilde{\Psi}_{k,11}(\vec{x}) & \tilde{\Psi}_{k,12}(\vec{x}) \\ \tilde{\Psi}_{k,21}(\vec{x}) & \tilde{\Psi}_{k,22}(\vec{x}) \end{pmatrix}.$$

On the source plane, we define the Jacobian matrix $\mathcal{A}_{N+1}$ by

$$\mathcal{A}_{N+1} = \begin{pmatrix} 1-\kappa-\gamma_1 & -\gamma_2+\omega \\ -\gamma_2-\omega & 1-\kappa+\gamma_1 \end{pmatrix}. \tag{4.62}$$

This is not necessarily symmetric since it is the product of two symmetric matrices. The asymmetry is given by the rotation term ω that appears only in the multiple lens-plane theory because the Jacobian matrix is symmetric for a single lens plane. The terms κ and γ appearing in Eq. 4.62 are now the effective convergence and the effective shear, respectively.

Flexion

From the definition of the tensor D whose components give rise to the first and second flexion, differentiating equation 4.60 with respect to $\vec{\theta}$, we find a recursive relation for the flexion tensors $D_{1,i} = \frac{\partial\mathcal{A}_i}{\partial\theta_i^1}$ and $D_{2,i} = \frac{\partial\mathcal{A}_i}{\partial\theta_i^2}$:

$$D_i = \frac{\partial\mathcal{A}_i}{\partial\vec{\theta}_i} = -\sum_{k=1}^{i-1} \frac{f_K(w_i - w_k) f_K(w_k)}{f_K(w_i) a_k} \left[f_K(w_k)\, \tilde{\mathcal{G}}_U \mathcal{A}_k + \tilde{\mathcal{U}}_k D_k \right], \tag{4.63}$$

where $\tilde{\mathcal{G}}_U \equiv \nabla_{\vec{x}}\tilde{\mathcal{U}}$ is the gradient of the tidal matrix:

$$\tilde{\mathcal{G}}_U^1 = \begin{pmatrix} \tilde{\Psi}_{k,111}(\vec{x}) & \tilde{\Psi}_{k,121}(\vec{x}) \\ \tilde{\Psi}_{k,211}(\vec{x}) & \tilde{\Psi}_{k,221}(\vec{x}) \end{pmatrix} \quad \text{and} \quad \tilde{\mathcal{G}}_U^2 = \begin{pmatrix} \tilde{\Psi}_{k,112}(\vec{x}) & \tilde{\Psi}_{k,122}(\vec{x}) \\ \tilde{\Psi}_{k,212}(\vec{x}) & \tilde{\Psi}_{k,222}(\vec{x}) \end{pmatrix}.$$

As before for the Jacobian matrix $\mathcal{A}_{N+1}$ on the source plane, also $D_{N+1,1}$ and $D_{N+1,2}$ are not symmetric anymore, so now they read

$$D_{N+1,1} = \begin{pmatrix} -2\gamma_{1,1} - \gamma_{2,2} & -\gamma_{2,1} + \omega_1 \\ -\gamma_{2,1} - \omega_1 & -\gamma_{2,2} \end{pmatrix} \quad , \quad D_{N+1,2} = \begin{pmatrix} -\gamma_{2,1} & -\gamma_{2,2} + \omega_2 \\ -\gamma_{2,2} - \omega_2 & 2\gamma_{1,2} - \gamma_{2,1} \end{pmatrix}. \tag{4.64}$$

where the two terms ω_1 and ω_2 show the asymmetry of the previous matrices.

4.6 Lensing of the CMB

All the previous machinery can be applied to study the gravitational lensing of the CMB for which the source is set to $z_s \approx 1100$.

According to the lens equation, temperature fluctuations at position $\vec{\beta}$ are shifted to the new position $\vec{\theta} = \vec{\beta} + \vec{\alpha}$, so as a consequence the CMB power spectrum and the correlation function will be affected by gravitational lensing.

Indicating with $\tau(\vec{\theta}) \equiv T(\vec{\theta})/\langle T \rangle$ the relative temperature fluctuations of the CMB, where $\langle T \rangle = 2.726\ K$, the temperature autocorrelation function without lensing is $\langle \tau(\vec{\theta})\tau(\vec{\theta}+\vec{\phi}) \rangle$ and with lensing it becomes $\langle \tau(\vec{\theta} - \vec{\alpha})\tau(\vec{\theta}' - \vec{\alpha}') \rangle$, where $\vec{\alpha} = \vec{\alpha}(\vec{\theta})$, $\vec{\alpha}' = \vec{\alpha}(\vec{\theta}')$ and $\vec{\theta}' = \vec{\theta} + \vec{\phi}$.

Carrying out the calculations for the lensed autocorrelation function in sufficient approximation leads to

$$\xi_T(\phi) = \int_0^\infty \frac{l dl}{2\pi} P_T(l) \exp(\sigma^2(\phi) l^2/2) J_0(l\phi), \tag{4.65}$$

where $J_0(x)$ is the Bessel function of order zero, $\sigma^2(\phi) \equiv \frac{1}{2}\langle (\vec{\alpha} - \vec{\alpha}') \rangle$ and $P_T(l)$ the unlensed power spectrum. Equation 4.65 shows that the effect of lensing is to smooth fluctuations on scales smaller than $\sigma(\phi)$.

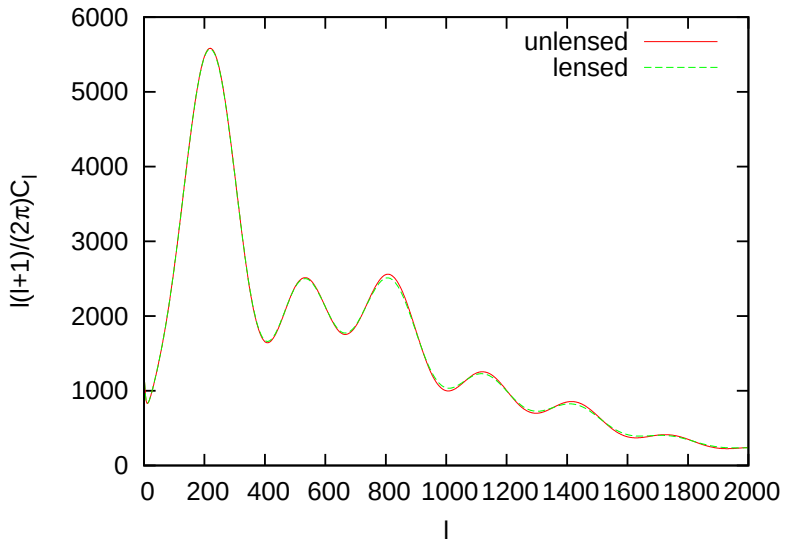

Figure 4.6: CMB angular power spectrum $l(l+1)/(2\pi)C_l$ as a function of the multipole l. The red line shows the intrinsic power spectrum, the green line shows the lensed power spectrum. They refer to a ΛCDM model. The graph is produced with the code CMBEASY, see Doran (2005).

The lensed power spectrum will be the Fourier transform of the lensed autocorrelation function, so also in this case the effect of the lensing will be that of smoothing.

In more detail, carrying out the Fourier transform of equation 4.65, the lensed CMB power spectrum $P'_T(l)$ reads as

$$P'_T(l) = \int d^2\phi \int \frac{d^2l'}{2\pi^2} P_T(l') \exp\left(-\frac{\sigma^2(\phi)l'^2}{2}\right) \exp\left[i\vec{\phi}(\vec{l}-\vec{l'})\right] \tag{4.66}$$

In figure 4.6 we show the intrinsic and the lensed CMB angular power spectra for a ΛCDM model.

Chapter 5

Testing the reliability of weak lensing cluster detections

In the previous chapters we described the evolution of structures and how they give rise to weak gravitational lensing and therefore it is possible to detect them through their lensing signal.
Several methods have been proposed, but how reliably can dark-matter halos be detected by means of weak lensing, and what selection function in terms of mass and redshift can be expected?
This questions are important to be addressed as ongoing and expecially future wide field optical surveys start providing such observational data.

The subject of detecting dark matter halos covers several scientific questions, in particular as to how the non-linear growth of sufficiently massive structures proceeds throughout cosmic history, whether galaxy-cluster detection based on gas physics agrees with or differs from lensing-based detection, whether dark-matter concentrations exist which emit substantially less light than usual or none at all, what cosmological information can be obtained by counting dark-matter halos, and so forth.

Due to increasing performance of lensing surveys which cover substantial fractions of the sky, such as the CFHTLS survey, the upcoming Pan-STARRS surveys, or the planned surveys with the DUNE or SNAP satellites, automatic searches for dark-matter halos will routinely be carried out, see for example Erben et al. (2000) and Erben et al. (2000). It is

important to study what they are expected to find.

Several different methods for identifying dark-matter halos in weak-lensing data have been proposed in recent years. They can all be considered as variants of linear filtering techniques with different kernel functions. Particular examples are the aperture mass with the radial filter functions proposed by Schneider et al. (1998) and modified by Schirmer et al. (2004) and Hennawi & Spergel (2005), and the filter optimised for separating the weak-lensing signal of dark-matter halos from that of the large-scale structures (LSS) they are embedded in (Maturi et al., 2005).

The non-negligible contamination by the large-scale structure was already noted by Reblinsky & Bartelmann (1999) and White et al. (2002), and Hoekstra (2001) quantified its impact on weak-lensing mass determinations. Hennawi & Spergel (2005) showed that the redshift of background galaxies can be used to improve the number of reliable detections. An approach alternative to matched filters is based on the peak statistics of convergence maps (Jain & Van Waerbeke, 2000), e.g.õbtained with the Kaiser-Squires inversion technique (Kaiser & Squires, 1993; Kaiser et al., 1995) or variants thereof.

We evaluate three halo-detection filters in terms of their performance on simulated large-scale structure data in which the dark-matter halos are of course known. One of the filters is specifically designed to optimally suppress the LSS contamination (Maturi et al., 2005). This allows us to quantify the completeness of the resulting halo catalogues, the fraction of spurious detections they contain, and the halo selection function they achieve. In particular, we compare the performance of the three filters mentioned in order to test and compare their reliability under a variety of conditions.
We describe the numerical simulation in Section 5.1; the weak-lensing filters are discussed in Section 5.2 and in Section 5.3 we present the result of the statistical analysis. Section 5.4 is dedicated to the comparison of suitably adapted simulation results to the GaBoDS data and we summarise in Section 5.5.

5.1 The numerical simulation

The time evolution of large-scale structures and galaxy clusters is impossible to solve analitycally, so numerical techniques must be used. To do so, *N*-body simulation codes are intensively used. More details on *N*-body codes are given in the appendix A.

5.1.1 The cosmological box

The cosmological simulation used in this study is the result of a hydrodynamical, *N*-body simulation, carried out with the code GADGET-2 (Springel, 2005, for the details of the implementation of the code). It has been described and used in several previous studies (Murante et al., 2004; Roncarelli et al., 2006). We only briefly summarise here some of its characteristics. A more detailed discussion can be found in the paper by Borgani et al. (2004).

The simulation represents a concordance ΛCDM model, with matter density parameter $\Omega_m = 0.3$ and a contribution from the cosmological constant $\Omega_\Lambda = 0.7$. The Hubble parameter is $h = H_0/100 = 0.7$ and a baryon density parameter $\Omega_{bar} = 0.04$ is assumed. The normalisation of the power spectrum of the initial density fluctuations, given in terms of the *rms* density fluctuations in spheres of $8\,h^{-1}$Mpc, is $\sigma_8 = 0.8$, in agreement with the most recent constraints from weak lensing and from the observations of the Cosmic Microwave Background (e.g. Hoekstra et al., 2006; Spergel et al., 2007).

The simulated box is a cube with a side length of $192\,h^{-1}$Mpc. It contains 480^3 particles of dark matter and an equivalent number of gas particles. The Plummer-equivalent gravitational softening is set to $\varepsilon_{Pl} = 7.5kpc/h$ comoving between redshifts two and zero, and chosen fixed in physical units at higher redshift.

The evolution of the gas component is studied including radiative cooling, star formation and supernova feedback, assuming zero metalicity. The treatment of radiative cooling assumes an optically thin gas composed of 76% hydrogen and 24% of helium by mass, plus a time-dependent, photoionising uniform UV background given by quasars reionising the Universe at $z \approx 6$. Star formation is implemented using the hybrid multiphase

model for the interstellar medium introduced by Springel & Hernquist (2003b), according to which the ISM is parameterised as a two-phase fluid consisting of cold clouds and hot medium.

The mass resolution is $6.6 \times 10^9 M_\odot/h$ for the cold dark matter particles, and $8.9 \times 10^8 M_\odot/h$ for the gas particles. This allows resolving halos of mass $10^{13} h^{-1} M_\odot$ with several thousands of particles.

Several snapshots are obtained from the simulation at scale factors which are logarithmically equidistant between $a_{ini} = 0.1$ and $a_{fin} = 1$. Such snapshots are used to construct light-cones for the following ray-tracing analysis.

5.1.2 Construction of the light-cones

Aiming at studying light propagation through an inhomogeneous universe, we construct light-cones by stacking snapshots of our cosmological simulation at different redshifts. Each snapshot consists of a cubic volume containing one realization of the matter distribution in the ΛCDM model at a given redshift. However, since they are all obtained from the same initial conditions, these volumes contain the same cosmic structures in different stages of their evolution. Such structures are approximately at the same positions in each box. Hence, if we want to stack snapshots in order to build a light-cone encompassing the matter distribution of the universe between an initial and a final redshift, we cannot simply create a sequence of consecutive snapshots. Instead, they must be randomly rotated and shifted in order to avoid repetitions of the same cosmic structures along one line-of-sight. This is achieved by applying transformations to the coordinates of the particles in each cube. When doing so, we consider periodic boundary conditions such that a particle exiting the cube on one side re-enters on the opposite side.

One additional problem in stacking the cubes is caused by the fact that, as they were written at logarithmically spaced scale factors, consecutive snapshots overlap with each other by up to two-thirds of their comoving side-length (at the lowest redshift). Thus, we have to make sure to count the matter in the overlapping regions only once. For doing so, we chose to remove particles from the later snapshot. The choice of the particles to

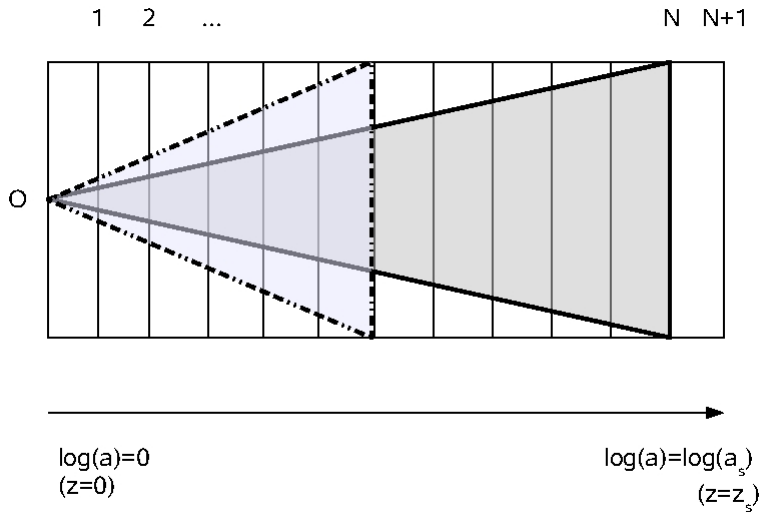

Figure 5.1: Sketch illustrating the construction of the light cones. A sequence of N lens planes (vertical lines) is used to fill the space between the observer (O) and the sources on the $(N+1)$-th plane. The aperture of the light cone depends on the distance to the last lens plane. At low redshifts, only a small fraction of the lens planes enters the light-cone (dark-gray shaded region). This fraction increases by reducing the redshift of the sources, increasing the aperture of the light cone (light-gray shaded region).

remove from the light cone is not critical, since snapshots are relatively close in cosmic time. Several tests have confirmed this expectation. Hence, the light-cone to a given source redshift z_s is constructed by filling the space between the observer and the sources with a sequence of randomly rotated and shifted volumes. If the size of the volumes is small enough, we can approximate the three-dimensional mass distribution in each volume by a two-dimensional mass distribution as explained in chapter 4. This is done by projecting the particle positions on the mid-plane through each volume perpendicular to the line-of-sight. Such planes will be used as lens planes in the following ray-tracing simulations. The opening angle of the light-cone is defined by the angle subtending the physical side-length of the last plane before the source plane. For sources at $z_s = 1$ and $z_s = 2$, this corresponds to opening angles of 4.9 and 3.1 degrees, respectively. In principle, tiling snapshots at constant cosmic time allows the creation light-cones of arbitrary opening angles. However, this is not necessary for the purposes of the present study.

If the size of the light-cone is given by the last lens plane, increasingly smaller fractions of the remaining lens planes will enter the light cone as it approaches $z = 0$ ($a = 1$, see Fig.5.1).

5.1.3 Halo catalogues

Each simulation box contains a large number of dark-matter halos. For our analysis, it is fundamental to know the location of the halos as well as some of their properties, such as their masses and virial radii. Thus, we construct a catalogue of halos for each snapshot. The procedure is as follows. We first run a friends-of-friends algorithm to identify the particles belonging to a same group. The chosen linking length is 0.15 times the mean particle separation. Then, within each group of linked particles, we identify the particle with the smallest value of the gravitational potential. This is taken to be the centre of the halo. Finally, we calculate the matter overdensity in spheres around the halo centre and measure the radius that enclosing an average density equal to the virial density for the adopted cosmological model, $\rho_{\rm vir} = \Delta_c(z)\rho_{\rm crit}(z)$, where $\rho_{\rm crit}(z)$ is the critical density of the universe at redshift z, and the overdensity $\Delta_c(z)$ is calculated as described in Eke et al. (2001).

We end up with a catalogue containing the positions, the virial masses and radii, and the redshifts of all halos in each snapshot. The positions are given in comoving units in the coordinate system of the numerical simulation. They are rotated and shifted in the same way as the particles during the construction of the light-cone. The positions of the halos in the cone are finally projected on the corresponding lens plane.

In Fig.5.2, we show the mass functions of the dark-matter halos normalised to one square degree and contained in the light-cones corresponding to $z_{\rm s} = 1$ (solid line) and $z_{\rm s} = 2$ (dashed line). Obviously the light-cones contain a large number of low-mass halos ($\sim 10^{11} - 10^{13}\,h^{-1}M_{\odot}$) which are expected to be undetectable through weak lensing. On the other hand, a much lower number of halos with mass $M \gtrsim 10^{13}\,h^{-1}M_{\odot}$ are potential lenses. We note that the numbers of haloes with masses larger than $5 \times 10^{13}M_{\odot}$ are approximately equal in both light cones, because such haloes are mainly contained in the

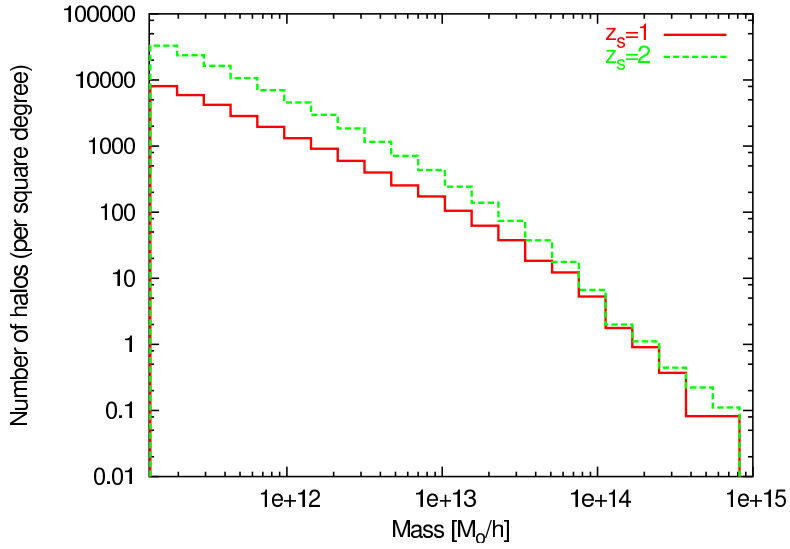

Figure 5.2: Number of halos per mass bin per square degree. The red and green curves show the halo mass distribution for sources at $z_s = 1$ and $z_s = 2$, respectively.

low-redshift portion of the volume which is common to both light cones.

We ignore the intracluster gas here because it contributes about one order of magnitude less mass than the dark matter and therefore does not significantly affect the weak-lensing quantities.

5.1.4 Ray-tracing simulations

The multiple-plane lensing simulations are carried out using standard ray-tracing techniques. Starting from the observer, we trace a bundle of 2048×2048 light rays through a regular grid covering the first lens plane. Then, we follow the light paths towards the sources, taking the deflections on each lens plane into account.

In order to calculate the deflection angles, on each lens plane, the particle positions are interpolated on regular grids of 2048×2048 cells using the triangular-shaped-cloud (TSC) scheme, this allows to avoid sudden discontinuities in the lensing mass distributions, that would lead to anomalous deflections of the light rays (Meneghetti et al., 2000; Hamana & Mellier, 2001).The resulting projected mass maps, M^i_{lm}, where $l, m = 1, ..., 2048$ and

$i = 1, ..., N$, are then converted into maps of the projected density contrast,

$$\delta_{lm}^{proj,i} = \frac{M_{lm}^{i}}{A_i \bar{\rho}} - L_i \, , \tag{5.1}$$

where A_i and L_i are the area of the grid cells on the i-th plane and the depth of the i-th volume used to build the light cone, respectively.

The lensing potential at each grid point, ψ_{lm}^{i}, is then calculated using the following equation

$$\nabla_{\vec{x}}^2 \psi_i(\vec{\theta}) = \frac{8\pi G \bar{\rho}}{3c^2} \delta_i^{proj}(\vec{\theta}) = 3\Omega \left(\frac{H_0}{c} \right)^2 \delta_i^{proj}(\vec{\theta}) \, , \tag{5.2}$$

such that the deflection angle is

$$\hat{\vec{\alpha}}_i = \vec{\nabla}_{\vec{x}} \psi_i \, . \tag{5.3}$$

Owing to the periodic boundary conditions of the density-contrast maps, this is easily solvable using fast-Fourier techniques. Indeed, equation 5.2 becomes linear in Fourier space,

$$\hat{\psi}(\vec{k}) = -3\Omega \left(\frac{H_0}{c} \right)^2 \frac{\hat{\delta}^{proj}(\vec{k})}{k^2} \, , \tag{5.4}$$

where $\vec{k}$ is the wave vector and $\hat{\psi}$ and $\hat{\delta}^{proj}$ are the Fourier transforms of the lensing potential and of the projected density contrast, respectively. Using finite-differencing schemes, we finally obtain maps of the deflection angles on each plane, α_{lm}^{i} (Premadi et al., 1998).

The arrival position of each light ray on the source plane is computed using equation 4.59 which incorporates the deflections on all preceding N lens planes. However, the ray path intercepts the lens plane at arbitrary points, while the deflection angles are known on regular grids. Thus, the deflection angles at the ray position are calculated by bi-linear interpolation of the deflection angle maps. Again using finite differencing schemes, we employ equations 4.61 and 4.62 to obtain maps of the effective convergence and shear.

5.1.5 Testing our ray-tracing code

We test the reliability of the ray-tracing code by comparing the statistical properties of several ray-tracing simulations with the theoretical expectations for a ΛCDM cosmology. In these tests, we assume that all source redshifts are $z_s = 1.5$. For this source redshift, the light cone spans a solid angle of roughly $3.6^2 \simeq 13$ square degrees on the sky. We perform ray-tracing through 60 different light-cones in total.

In Fig. 5.3, we show in the upper panel the power spectra of the effective convergence and the shear and in the lower panel the power spectrum of the deflection angle, obtained by averaging over all different realizations of the light-cone. These are given by the solid and by the dotted lines, respectively. The theoretically expected power spectrum is shown as the dashed green line. As expected, the convergence and the shear power spectra are equal. We note that the numerical power spectra agree with the corresponding theoretical expectation over a limited range of wave numbers. Indeed, the effective convergence and shear power spectra deviate from the theoretical power spectrum for $k \lesssim 200$ and for $k \gtrsim 20000$, while the deflection angle power spectrum starts to deviate already at $k \approx 2000$. These values of the wave vector define the reliability range of these simulations and are determined by numerical issues. On angular scales $\gtrsim 1^\circ$, we miss power because of the small size of the simulation box, while on angular scales smaller than $\lesssim 1'$ we suffer from resolution problems due to the finite resolution of the ray and the mass grids.

The different behaviour of the power spectra of the effective convergence and of the deflection angle are explained through numerical issues due to the different weighting functions. From equations 4.59 and 4.61 we notice that the weighting functions for the deflection angle and for the effective convergence are

$$W_{\vec{\alpha}} = \frac{f_K(w_s - w_l)}{f_K(w_s)} \tag{5.5}$$

$$W_\kappa = \frac{f_K(w_l) f_K(w_s - w_l)}{f_K(w_s)}, \tag{5.6}$$

where w_s and w_l represent the comoving distance of the source and of the lense.

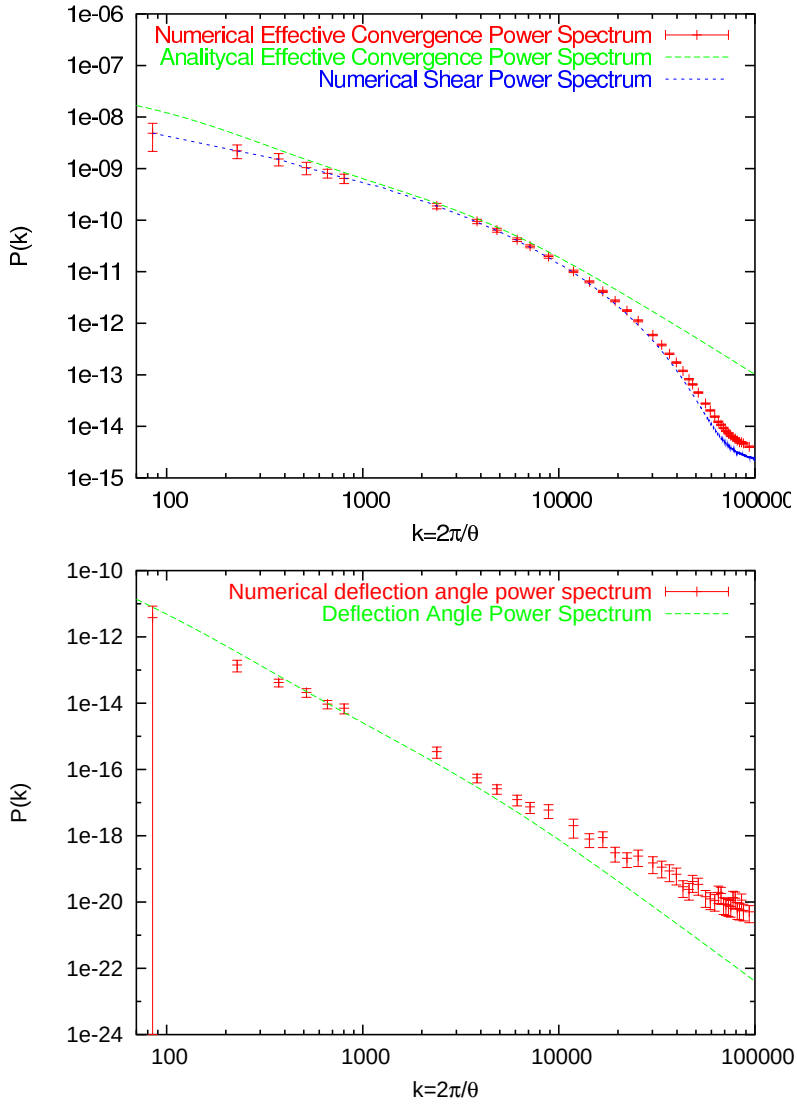

Figure 5.3: Numerical power spectra of the effective convergence (solid line) and of the shear (dotted line) (upper panel) and of the deflection angle (bottom panel) obtained by averaging over 60 different light cones corresponding to a solid angle of ~ 13 square degrees. The power spectrum expected for a ΛCDM model with the same cosmological parameters as the simulation is given by the dashed line. The errorbars are shown only for the effective convergence power spectrum, but are of equivalent size for the shear power spectrum.

As it appears clear in figure 5.4, for the deflection angle the major contribution comes from the lensing planes at low redshifts where the resolution is quite poor, while for the effective convergence the weighting function is represented by the effective lensing

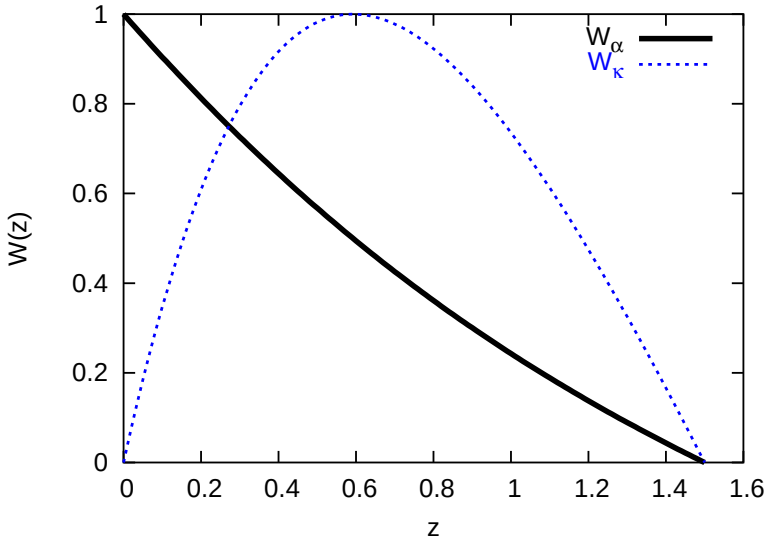

Figure 5.4: Weighting functions for the deflection angle (black solide curve) and for the effective convergence (blue dottoed line) for sources at redshift $z_s = 1.5$. Both curves are normalized to unity. The maximum of W_α is for small values, while W_κ reaches the maximum at intermediate redshifts between the observer and the source.

distance, so most of the contribution comes from the planes at intermediate where the resolution effects are not so important as for the case of the deflection angle.

5.1.6 Lensing of distant galaxies

Using the effective convergence and shear maps obtained from the ray-tracing simulations, we are now able to apply the lensing distortion to the images of a population of background sources. As already said in section 4.5.1, the distorsion to the galaxies shape can be inferred from the reduced shear g.

In order to generate a mock catalogue of lensed sources, galaxies are randomly placed and oriented on the source plane. Their intrinsic ellipticities are drawn from the distribution shown in equation 4.29. We assume a background galaxy number density of $n_g = 30$ arcmin^{-2}. Observed ellipticities are obtained from equation 4.28 by interpolating the effective convergence and shear at the galaxy positions. This procedure results in catalogues of lensed galaxies for each source redshift chosen, where galaxy positions and ellipticities are stored.

5.2 Weak lensing estimators

We investigate the performances of three weak-lensing estimators which have been used so far for detecting dark-matter halos through weak lensing. These are the classical aperture mass (Schneider, 1996; Schneider et al., 1998), an optimised version of it (Schirmer et al., 2004), and the recently developed, optimal weak-lensing halo filter (Maturi et al., 2005). More details on these three estimators are given below.

All of them measure the amplitude of the lensing signal A within circular apertures of size $\bar{\theta}$ around a centre $\vec{\theta}$. Generalisations are possible to apertures of different shapes. In general, A is expressed by a weighted integral of the tangential component of the shear relative to the point $\vec{\theta}$, γ_t. The weight is provided by a filter function Ψ, such that

$$A(\vec{\theta},\bar{\theta}) = \int d^2\theta' \gamma_t(\vec{\theta}',\vec{\theta})\Psi(|\vec{\theta}'-\vec{\theta}|)\,, \tag{5.7}$$

and the integral extends over the chosen aperture. The variance of the weak-lensing estimator is given by

$$\sigma^2 = \frac{1}{(2\pi)^2}\int |\hat{\Psi}(\vec{k})|^2 P_N(k)\, d^2k, \tag{5.8}$$

where $\hat{\Psi}(\vec{k})$ is the Fourier transform of the filter, and $P_N(k)$ the power spectrum of the noise.

5.2.1 Aperture Mass

The aperture mass was originally proposed by (Schneider, 1996) for measuring the projected mass of dark-matter concentrations via weak lensing. It represents a weighted integral of the convergence,

$$M_{APT}(\vec{\theta}) \;=\; \int d^2\vec{\theta}'\kappa(\vec{\theta}')U(|\vec{\theta}'-\vec{\theta}|)\,. \tag{5.9}$$

The weight function $U(\theta)$ is symmetric if the aperture is chosen to be circular, and it is compensated, i.e.

$$\int_0^{\theta} d\theta'\theta' U(\theta') = 0\,. \tag{5.10}$$

Since the convergence is not an observable, the aperture mass is more conveniently written as a weighted integral of the tangential shear,

$$M_{APT}(\theta) \;=\; \int d^2\vec{\theta}'\gamma_t(\vec{\theta}',\vec{\theta})\Psi_{APT}(|\vec{\theta}'-\vec{\theta}|)\;, \tag{5.11}$$

where the function Ψ_{APT} is related to the filter function U by the equation

$$\Psi(\theta) = \frac{2}{\theta^2}\int_0^\theta d\theta'\theta' U(\theta') - U(\theta)\;. \tag{5.12}$$

The variance $\sigma^2_{M_{APT}}$ of M_{APT} is defined as

$$\sigma^2_{M_{APT}} = \frac{\pi\sigma^2_{\varepsilon_s}}{n_g}\int_0^\theta d\theta'\theta'\Psi^2_{APT}(|\vec{\theta}'-\vec{\theta}|)\;, \tag{5.13}$$

which takes into account the shot noise due to the finite number and the intrinsic ellipticities of the sources (Bartelmann & Schneider, 2001).

The shape of the filter function Ψ is usually chosen to have a compact support and to suppress the halo centre because the lensing measurements are more problematic there. Indeed, the weak-lensing approximation may break down and the cluster galaxies may prevent the ellipticity of background galaxies to be accurately measured.

Schneider et al. (1998) propose the polynomial function

$$\Psi_{APT} = \frac{(1+l)(2+l)}{\pi\theta^2_{max}}x^2(1-x^2)^l H(1-x)\;, \tag{5.14}$$

where $H(x)$ is the Heaviside step function, and $x = \theta/\theta_{max}$ is the radial angular coordinate in units of the radius, θ_{max}, where Ψ_{APT} vanishes. l is a free parameter which is usually set to $l = 1$. Note that this filter function was designed especially for measuring cosmic shear. However, several authors have used it for searches for dark matter halos (Erben et al., 2000; Schirmer et al., 2004).

More recently, other filter functions Ψ have been proposed which maximise the signal-to-noise ratio $M_{APT}/\sigma_{M_{APT}}$. Schneider et al. (1998) show that this is the case if Q mimics the shear profile of the lens. For example, Schirmer et al. (2004) propose a fitting formula that approximates the shear profile of a Navarro-Frenk-White (NFW) halo (Navarro et al.,

1997). Their filter function is

$$\Psi_{OAPT}(x) = \frac{1}{1+e^{6-150x}+e^{-47+50x}} \frac{\tanh x/x_c}{x/x_c}, \tag{5.15}$$

where x_c is a parameter controlling the shape of the filter (see also Padmanabhan et al., 2003; Hetterscheidt et al., 2005). From now on, we will refer to this implementation of the aperture mass as to the "optimised aperture mass".

Hennawi & Spergel (2005) included the photometric redshifts of background sources, increasing the halo-detection sensitivity at higher redshifts and for smaller masses. Aiming at a comparison of different filters, we neglect this additional information here. We can therefore not apply their tomographic approach, which is based on an NFW fitting formula. They also suggested using a Gaussian profile which found application in actual weak-lensing surveys (see e.g. Miyazaki et al., 2002), but here we focus on the filter proposed by Maturi et al. (2005) whose shape is statistically and physically well motivated.

5.2.2 Optimal Filter

Maturi et al. (2005) have recently proposed a weak-lensing filter optimised for an unbiased detection of the tangential shear pattern of dark-matter halos. Unlike the optimised aperture mass, the shape of optimal filter is determined not only by the shear profile of the lens, but also by the properties of the noise affecting the weak lensing measurements.

The measured data D is composed of the signal from the lens S and by the noise N, and can be written as

$$D(\vec{\theta}) = S(\vec{\theta}) + N(\vec{\theta}) = A\tau(\vec{\theta}) + N(\vec{\theta}) \,, \tag{5.16}$$

where A is the total amplitude of the tangential shear and $\tau(\vec{\theta})$ is its angular shape. The noise N comprises several contributions that can be suitably modeled.

The optimal filter accounts for the noise contributions because it is constructed such as to satisfy two conditions. First, it has to be unbiased, i.e. the average error on the estimate of the lensing amplitude,

$$A_{\rm est}(\vec{\theta}) = \int d^2\theta' D(\vec{\theta}')\Psi(|\vec{\theta}' - \vec{\theta}|) \tag{5.17}$$

has to vanish:

$$b \equiv \langle A_{est} - A \rangle = A \left[\int \Psi(\vec{\theta}) \tau(\vec{\theta}) d^2\theta - 1 \right] = 0 \,. \tag{5.18}$$

Second, the noise

$$\sigma^2 \equiv \langle (A_{est} - A)^2 \rangle = b^2 + \frac{1}{(2\pi)^2} \int |\hat{\Psi}(\vec{k})|^2 P_N(k) d^2k \tag{5.19}$$

has to be minimal with respect to the signal.

The filter function Ψ satisfying these two conditions is found by combining them with a Lagrangian multiplier λ. The variation $L = \sigma^2 + \lambda b$ is carried out, and the filter function Ψ is found by minimising L. In Fourier space, the solution of this variational minimisation is

$$\hat{\Psi}_{OPT}(\vec{k}) = \frac{1}{(2\pi)^2} \left[\int \frac{|\hat{\tau}(\vec{k})|^2}{P_N(k)} \, d^2k \right]^{-1} \frac{\hat{\tau}(\vec{k})}{P_N(k)} \,, \tag{5.20}$$

where the hats denote the Fourier transform. The last equation shows that the shape of the optimal filter Ψ is determined by the shape of the signal, τ, and by the power spectrum of the noise, P_N.

Maturi et al. (2005) model the signal by assuming that clusters are on average axially symmetric and their shear profile resembles that of an NFW halo (see e.g. Bartelmann, 1996; Wright & Brainerd, 2000; Li & Ostriker, 2002; Meneghetti et al., 2003). Consequently, this filter is optimised for searching for the same halo shape as the optimised aperture mass, even if the filter profile is different.

The noise is assumed to be given by three contributions, namely the noise contributions from the finite number of background sources, the noise from their intrinsic ellipticities and orientations, and the weak-lensing signal due to the large-scale structure of the universe.

The first two sources of noise are characterised by the power spectrum

$$P_\varepsilon(k) = \frac{1}{2} \frac{\sigma_{\varepsilon_s}^2}{n_g} \,, \tag{5.21}$$

which depends on the dispersion of the intrinsic ellipticities of the sources, σ_{ε_s}, and on the number density of background galaxies, n_g.

The statistical properties of the noise due to the lensing signal from the large-scale structure of the universe are described by the power-spectrum of the effective tangential shear. This is related to the power-spectrum of the effective convergence by

$$P_\gamma(k) = \frac{1}{2} P_\kappa(k) \; . \tag{5.22}$$

Thus, the total noise power spectrum is

$$P_N(k) = P_\gamma(k) + P_\varepsilon(k) \; , \tag{5.23}$$

where P_γ is determined by the linear theory of structure growth. Using the linear instead of the non-linear power spectrum avoids suppressing a substantial fraction of the signal from the non-linear structures we are searching for. To further reduce any loss of signal in the filtering process, it would be possible to cut P_γ off at angular scales typical for galaxy clusters. Doing so, we found that this approach has a negligible impact on the final result.

In Fig. 5.5, we compare the filters studied here and in the literature. They are scaled in such a way as they are typically discussed or applied in the literature (see also the figure legend and caption for more detail). At first sight, the scales are surprisingly different. When the optimal filter is constructed including the linear matter power spectrum such as to best suppress the LSS contribution, it shrinks considerably. It is reassuring that the truncated NFW-shaped filter (THS) proposed and heuristically scaled by Hennawi & Spergel (2005) to yield best results almost exactly reproduces the optimal filter. They are therefore expected to perform similarly well. The optimised aperture-mass filter (OAPT) also peaks at fairly small angular scales, but shows the long tail typical for the NFW profile. The aperture mass has its maximum at comparatively large radii, explaining why the APT filter yields results most severely affected by the LSS.

For completeness we report the truncated NFW-shaped filter proposed by Hennawi & Spergel (2005):

$$\Psi_{THS} = \left(\frac{2\ln(1+x)}{x^2} - \frac{2}{x(1+x)} - \frac{1}{(1+x)^2} \right) \exp\left(\frac{\theta^2}{2\theta_{out}^2} \right) , \tag{5.24}$$

where $x = \theta/\theta_s$.

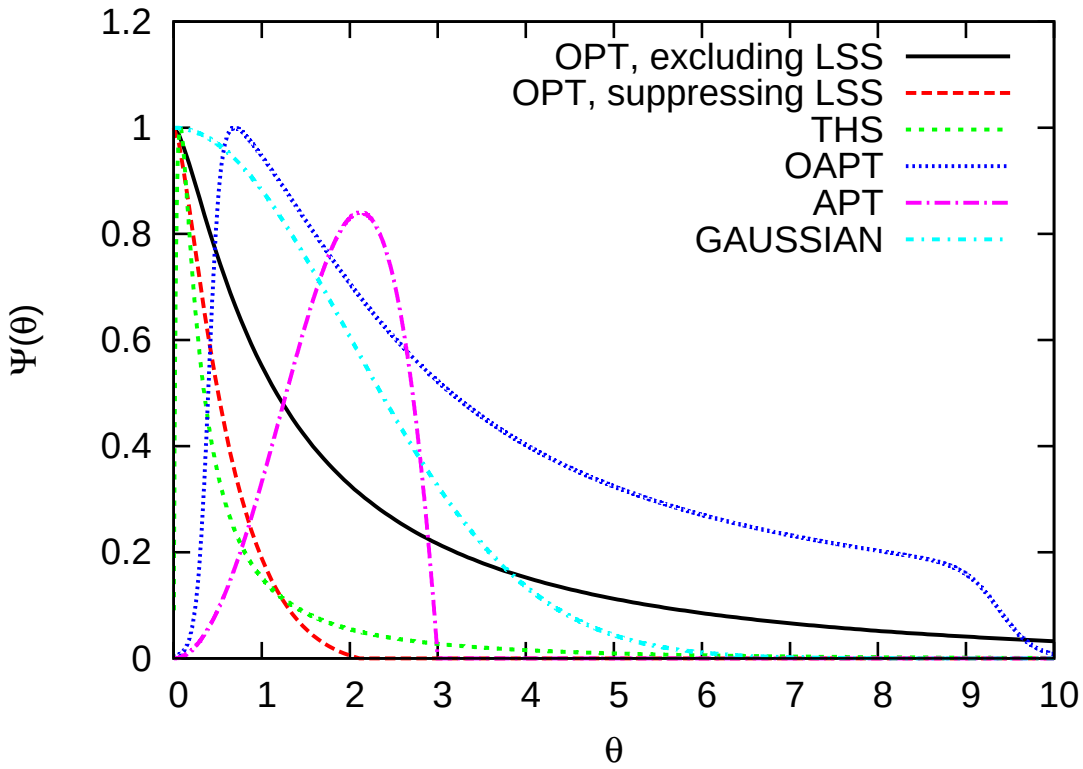

Figure 5.5: Comparison of the different filter shapes used here and in the literature. The filter scales r_s are those typically used in the literature. Note how the optimal filter (black solid curve) shrinks when the linear matter power spectrum is used to suppress the LSS contribution (red dashed curve). Interestingly, Hennawi & Spergel (2005) found experimentally that the truncated NFW-shaped filter (cyan curve) performs best when scaled to the green curve (THS), which approximates the optimal filter (OPT, red curve) almost precisely. The advantage of the optimal compared to the other filters is that its shape and scale are physically and statistically well motivated such that it needs not be experimentally rescaled.

5.3 Statistics of halo detections

5.3.1 Signal-to-noise maps

We now use the above-mentioned weak-lensing estimators to analyse our mock catalogues of lensed galaxies.

In practice, the integral in equation 5.7 is replaced by a sum over galaxy images. Moreover, since the ellipticity ε is an estimator for γ, we can write

$$A_{est}(\vec{\theta}) = \frac{1}{n_g}\sum_i \varepsilon_{ti}(\vec{\theta}_i)\Psi(|\vec{\theta}_i - \vec{\theta}|)\ , \tag{5.25}$$

where $\varepsilon_{ti}(\vec{\theta}_i)$ is the tangential component of the observed ellipticity of the galaxy at $\vec{\theta}_i$, with respect to the point $\vec{\theta}$. Similarly, the noise estimate in A_{est} is given by

$$\sigma^2(A_{est})(\vec{\theta}) = \frac{1}{2n_g^2}\sum_i |\varepsilon_i(\vec{\theta}_i)|^2 \Psi^2(|\vec{\theta}_i - \vec{\theta}|). \tag{5.26}$$

Computing A_{est} and $\sigma^2(A_{est})$ on a grid covering our simulated sky, we produce maps of the signal-to-noise ratio for all the weak lensing estimators. We use three different filter sizes for each estimator in order to test the stability of the results achieved. These have been calibrated among the different filters to allow the optimal detection of similar objects. For the optimal filter, we used sizes of $1'$, $2'$ and $4'$. These correspond to $2.75'$, $5.5'$ and $11'$ for the aperture mass, for the optimised aperture mass we used the values $5'$, $10'$ and $20'$ that are widely used in literature.

In Fig. 5.6 we show examples of the signal-to-noise iso-contours of the weak lensing signal, superimposed on the corresponding effective convergence maps of the underlying projected matter distribution for sources at redshift $z_s = 1$ (left panels) and $z_s = 2$ (right panels). The iso-contours start at $S/N = 4$ with a step of 3. From top to bottom, the maps refer to the results obtained using the aperture mass (APT), the optimised aperture mass (OAPT) and the optimal filter (OPT) with sizes of $11'$, $20'$ and $4'$, respectively. The circles identify halos with mass $M \geq 7 \times 10^{14} h^{-1} M_{\odot}$ present in the field-of-view. The side length of each map is one degree.

The images show that, for sources at high redshift, all three estimators can successfully detect the weak-lensing signal from clusters in the mass range considered. However, spurious detections, corresponding to high signal-to-noise peaks not associated with any halo, also appear. Their significance and spatial extent is larger in the case of the APT and the OAPT filters. This confirms the results of Maturi et al. (2005).

For lower-redshift sources, the OPT detects five out of the seven halos present in the field, while the APT and the OAPT detect substantially fewer halos. For the OPT, the number of spurious detections is roughly the same or slightly smaller than for sources at higher redshift, while it is strongly reduced for the APT and the OAPT. The natural explanation of these results is that the detections with the APT and the OAPT are strongly

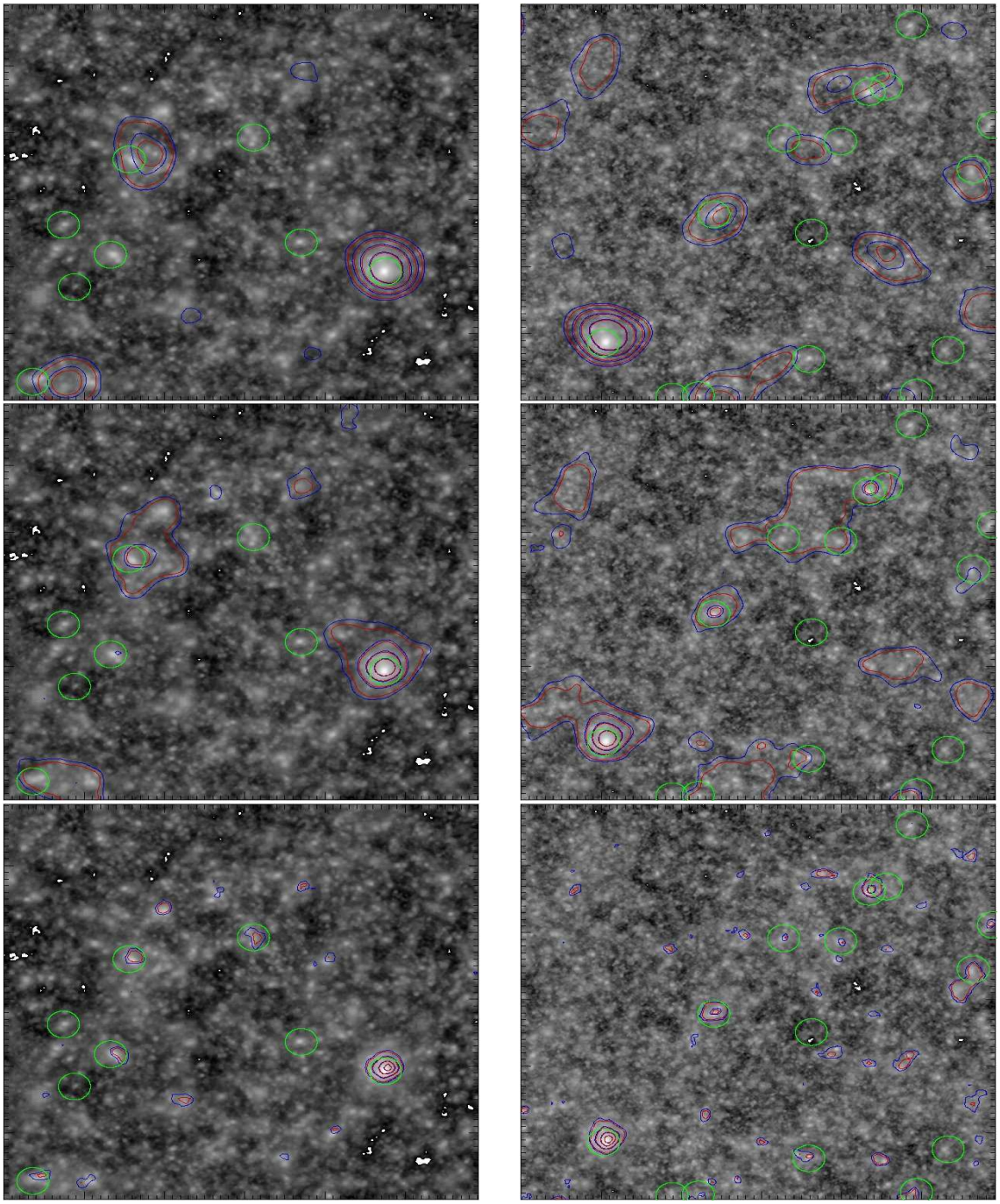

Figure 5.6: Maps of the effective convergence for sources at redshift $z_s = 1$ (left panels) and $z_s = 2$ (right panels) for a region of simulated sky. Superimposed are the iso-contours of the signal-to-noise ratio of the weak-lensing signal measured with three estimators, namely the APT (top panels), the OAPT (middle panels) and the OPT (bottom panels). The iso-contours start from $S/N = 4$ with a step of 3. The positions of the halos contained in the field-of-view having mass $M > 7 \times 10^{13} h^{-1} M_{\odot}$ are identified by circles. The filter sizes are $11'$, $20'$ and $4'$ for the APT, the OAPT and the OPT, respectively.

contaminated by the noise from large-scale structure lensing, which becomes increasingly important for sources at higher redshift. This noise is efficiently filtered out by the OPT.

5.3.2 True and spurious detections

In the following, we call a *detection* a group of pixels in the S/N maps above a threshold S/N ratio. Its position in the sky is given by the most significant pixel, i.e. that with the highest S/N ratio.

A true detection is obviously a detection that can be associated with some halo in the simulation. A spurious detection is instead mimicked by noise, in particular by cosmic structures aligned along the line-of-sight.

The association between weak-lensing detections and cluster halos is established by comparing their projected positions on the sky. This causes a problem, because the simulation boxes contain plenty of low-mass halos that are not individually detectable through lensing but happen to be projected near the line-of-sight towards a detection. Thus, spurious detections could easily be erroneously associated with these low-mass halos on the basis of the projected position only.

As pointed out earlier, we describe the lensing effect of the matter contained in the light cone with a stack of lens planes. Cluster halos are localised structures, i.e. their signal originates from a single lens plane. Thus, any detection should disappear when its plane is removed from the stack. Conversely, spurious detections are not caused by localised structures and should remain even after removing an individual lens plane. This is illustrated by the S/N maps shown in Fig. 5.7. The map in the left panel includes all lens planes, while one plane was removed for the right panel. Both maps were obtained with the OAPT estimator with a filter size of $20'$ and a source redshift of $z_s = 1$. Clearly, the highest peak in the left panel, which is in fact produced by a massive halo, disappears in the right panel, after removing the lens plane from the stack which contains the halo. All other features in the left upper map remain unchanged.

This allows us to verify the reliability of detections associated with some halo in the catalogue. For each positive match, we estimate the lensing signal before and after re-

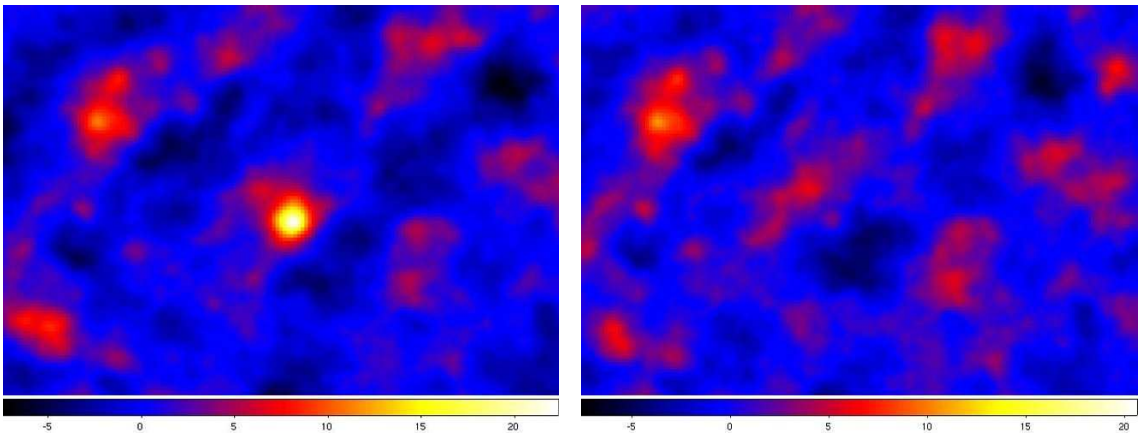

Figure 5.7: Map of the S/N ratio corresponding to a region of 3 square degrees. The map was created using the OAPT estimator, with a filter scale of $20'$ and assuming a source redshift of $z_s = 1$. The left panel shows the S/N ratio map including all lens planes, while the right panel shows the same map obtained after removing the lens plane containing the cluster responsible for the highest S/N peak in the left panel.

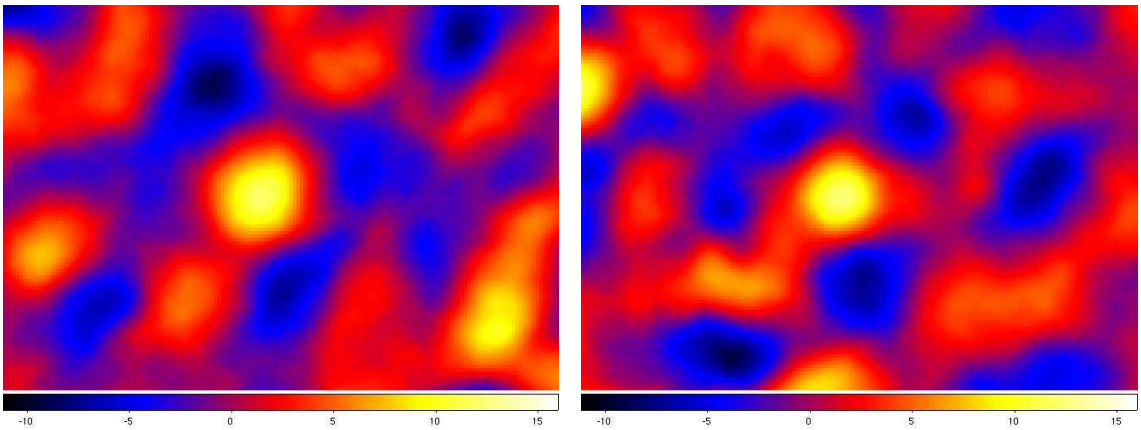

Figure 5.8: Maps of the S/N ratio corresponding to a region of 3 square degrees. The maps were created with the APT estimator, with a filter scale of $11'$ and assuming a source redshift of $z_s = 2$. The left panel shows a true detection, while the right panel shows a spurious detection.

moving the plane containing the candidate lensing halo from the lens-plane stack. If this causes a significant decrease in the S/N ratio, we classify the detection as true, and otherwise as spurious. We estimate through several checks of detections associated to the halos that S/N fluctuations of order 25% of the initial value are possible due to different properties of the noise. Thus, we set this limit as our threshold for discriminating between

true and spurious detections.

This method also shows its power when pixels identifying a true detection are compared with pixels associated to a spurious detection. This is shown in Fig. 5.8. The map in the left panel represents a true detections, while the map on the right panel shows a spurious detections. The maps refer to different regions of a S/N map created with the APT estimator with a filter size of $11'$ and a source redshift of $z_s = 2$. As it is clearly seen, it is impossible a priori to distinguish which of the two is spurious.

5.3.3 Statistical analysis of the detections

In Fig. 5.9, we show the number of detections per square degree in S/N ratio bins, ignoring for now the distinction between true and spurious detections. Left and right panels refer to simulations with sources at redshifts $z_s = 1$ and $z_s = 2$, respectively. From top to bottom, we show the results for the APT, the OAPT and the OPT estimators. In each panel, we use solid, dashed and dotted lines to display the histograms corresponding to increasing filter sizes.

For low source redshifts and small filter sizes, the APT and the OPT estimators lead to similar numbers of detections. Instead, for the OAPT, the number of detections is larger by up to a factor of two for $S/N \gtrsim 4$. Increasing the filter size, the number of detections generally increases for all estimators, especially for large S/N ratios and in particular for the OPT.

We notice, however, that for small S/N ratios, larger filters produce lower numbers of detections for the APT and for the OAPT. This behaviour is more evident for sources at higher redshifts. For example, we find that the number of detections with $S/N = 4$ drops by a factor of 4 for the APT and by a factor of ~ 7 for the OAPT, when increasing the filter size from $2.5'$ to $11'$ and from $5'$ to $20'$, respectively. Increasing the filter size, the weak-lensing signal is estimated by averaging over more background galaxies. Thus, high S/N peaks are smoothed, and some detections may be suppressed. This affects mainly the detections with the APT and the OAPT filters. On the other hand, the OPT filter shrinks in response to the noise introduced by the large scale structure, largely reducing this effect

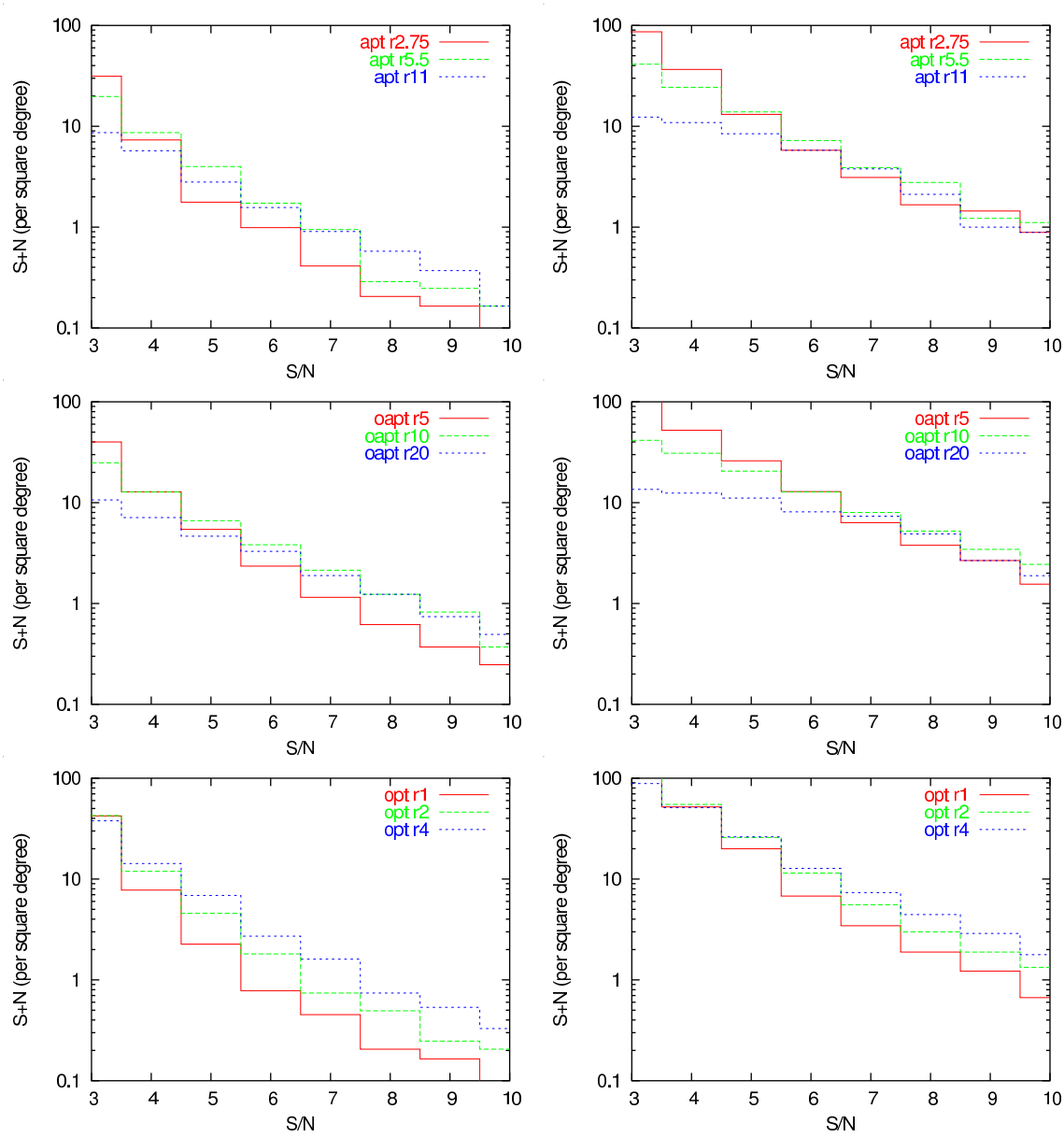

Figure 5.9: Number of detections as a function of the S/N ratio obtained by using the APT (top panels), the OAPT (middle panels) and the *OPT* weak lensing estimators. Results for sources at redshift $z_s = 1$ and $z_s = 2$ are shown in the left and in the right panels, respectively. Different line styles refer to three different filter sizes. For the OPT, these are $1'$, $2'$ and $4'$. They correspond to $2.75'$, $5.5'$, and $11'$ for the APT and to $5'$, $10'$ and $20'$ for the OAPT.

compared to the APT and the OAPT.

The fractions of spurious detections are shown in Fig. 5.10. Clearly, the OPT estimator

performs better than the APT and the OAPT. For sources at redshift $z_s = 1$ and $z_s = 2$, the fraction of spurious detections with the OPT is less than 20% and 30% at $S/N \sim 4$. This fraction decreases below 10% for $S/N \gtrsim 5$ and drops rapidly to zero for higher S/N ratios. Results are very stable against changes in the filter size. Conversely, the APT and the OAPT estimators yield similarly low fractions of false detections only for the smallest apertures.

Depending on the filter shape, its size and on the source redshift, a S/N threshold can be defined above which there are no spurious detections and thus all detections are reliable. For the OPT estimator, this minimal signal-to-noise ratio is between 5 and 8. It increases above 10 for the APT and the OAPT estimators if large filter sizes are used. These results agree with the results of Maturi et al. (2005), using numerical simulations, and of Maturi et al. (2007), regarding the analysis of the GaBoDS survey.

Here, we studied the contaminations by the LSS, the intrinsic ellipticity and the finite number of background galaxies all together. To gain an idea which of those is the main source for spurious detections, we used the APT with $r_s = 11'$ to analyse a catalogue of galaxies with intrinsic ellipticities set to zero. In this case, the S/N ratio is enhanced by a factor of four uniformly across the whole field, but the morphology of the map is not affected. The same should apply to the finite number of background sources. We thus conclude that the main source of spurious detections is the LSS, as already noted by Reblinsky & Bartelmann (1999) and White et al. (2002).

5.3.4 Sensitivity

We shall now quantify which halo masses the weak-lensing estimators are sensitive to.

Figure 5.11 shows the lowest mass detected in each redshift bin. This is defined as the mean mass of the ten least massive halos detected in this bin. Again, results are displayed for all weak-lensing estimators, for different filter sizes and for two source redshifts.

We note that the performance of the three filters is very similar for sources at redshift $z_s = 1$ (left panels). The OPT (bottom panels) is only slightly more efficient in detecting low-mass halos than the APT (top panels) and the OAPT (middle panels). The minimal

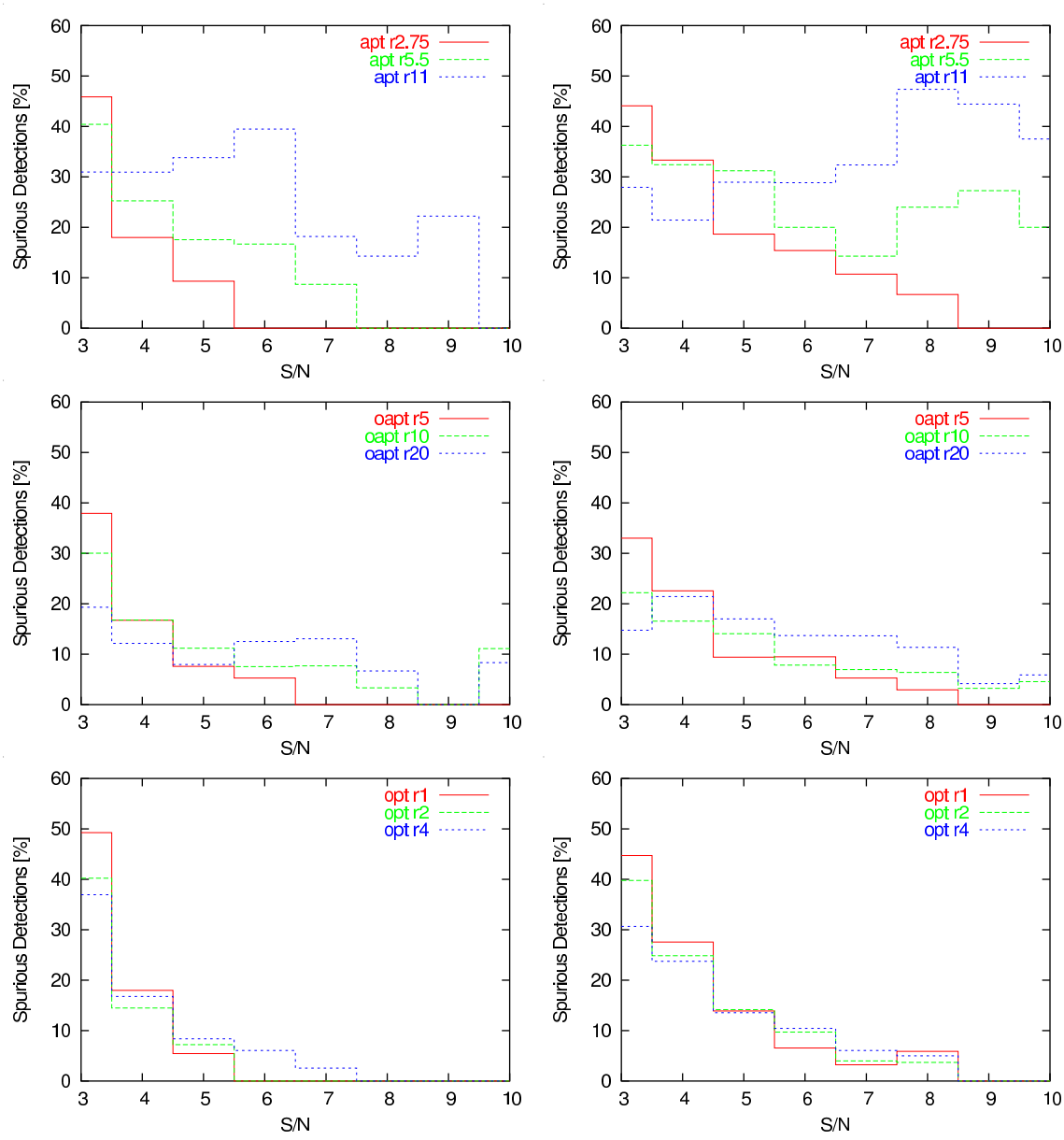

Figure 5.10: Fraction of spurious detections as a function of the S/N ratio obtained by using the APT (top panels), the OAPT (middle panels) and the *OPT* weak-lensing estimators. Results for sources at redshift $z_s = 1$ and z_s=2 are shown in the left and the right panels, respectively. Different line styles refer to three filter sizes. For the OPT these are $1'$, $2'$ and $4'$. They correspond to $2.75'$, $5.5'$, and $11'$ for the APT and to $5'$, $10'$ and $20'$ for the OAPT.

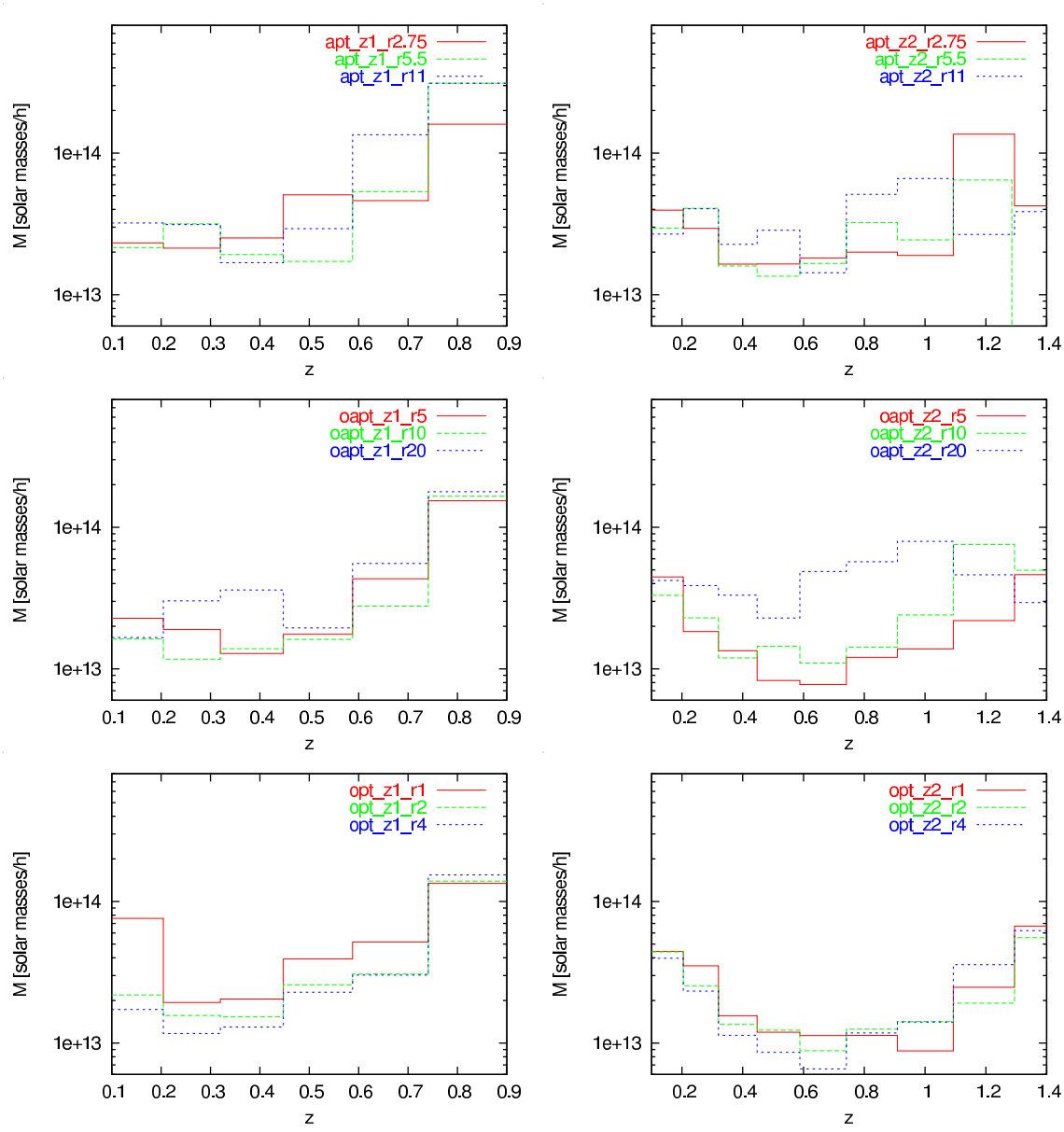

Figure 5.11: Minimum detected halo mass as a function of redshift for the APT (top panels), the OAPT (middle panels) and for the OPT (bottom panels) estimators. Results for sources at redshift $z_s = 1$ and $z_s = 2$ are shown in the left and in the right panels, respectively. Different line styles refer to three filter sizes. For the OPT, these are $1'$, $2'$ and $4'$. They correspond to $2.75'$, $5.5'$, and $11'$ for the APT and to $5'$, $10'$ and $20'$ for the OAPT. Results for each redshift bin are averaged between two planes.

mass detected depends on the lens redshift. All filters allow the detection of low-mass halos more efficiently if these are at redshifts between 0.2 and 0.5, i.e. at intermediate

distances between the observer and the sources. This obviously reflects the dependence of the geometrical lensing strength on the angular-diameter distances between the observer and the lens, the lens and the sources, and the observer and the sources. The lowest detected masses fall within $\sim 10^{13}h^{-1}M_{\odot}$ and $\sim 10^{14}h^{-1}M_{\odot}$ for the OPT estimator.

For sources at higher redshift, the region of best filter performance shifts to higher lens redshift, between 0.5 and 0.8. We note that due to the increasing importance of lensing by large-scale structures, the differences between the estimators are more significant. The OPT estimator allows the detection of halos with masses as low as $\lesssim 10^{13}h^{-1}M_{\odot}$, almost independently of the filter size. Similar masses are detected with the OAPT only for the smallest apertures. With the APT and the OAPT, the results are indeed much more sensitive to the filter size than with the OPT. Increasing the filter size pushes the detectability limit to larger masses. Again, as discussed in Sect. 5.3.3, this is due to the fact that the signal from low-mass halos is smeared out by averaging over an increasing number of galaxies entering the aperture. For example, the minimal mass detected with the OAPT filter at $z \sim 0.8$ changes by one order of magnitude by varying the filter scale from $5'$ to $20'$.

5.3.5 Completeness

We now discuss the completeness of a synthetic halo catalogue selected by weak lensing.

Figure 5.12 shows the fraction of halos contained in the light cone that are detected with different weak lensing estimators as a function of their mass. Again, we find that the OPT filter yields the most stable results with respect to changes in the filter size. This is particularly evident for sources at redshift $z_s = 2$ (right panels), while the differences are smaller for $z_s = 1$ (left panels). As discussed earlier, the APT and the OAPT become less efficient in detecting low-mass halos when the filter size is increased.

For the OPT estimator, the completeness reaches 100% for masses $M \gtrsim 3 \times 10^{14}h^{-1}M_{\odot}$ and $M \gtrsim 2 \times 10^{14}h^{-1}M_{\odot}$ for sources at redshift $z_s = 1$ and $z_s = 2$, respectively. For lower masses, the completeness drops quickly, reaching $\sim 50\%$ already at $M \sim 2 \times 10^{14}h^{-1}M_{\odot}$ for low-redshift sources, and at $M \sim 7 \times 10^{13}h^{-1}M_{\odot}$ for high-

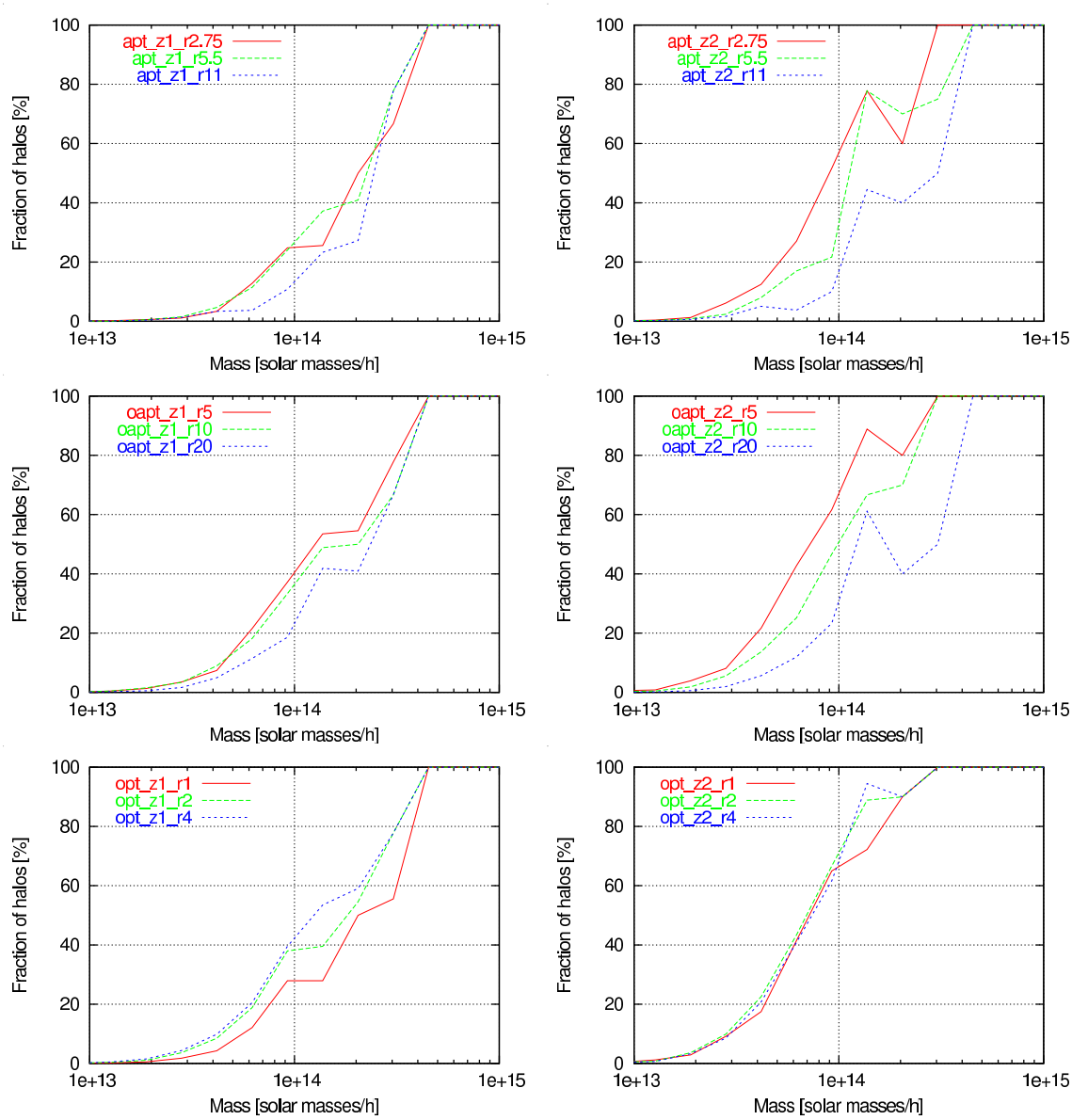

Figure 5.12: Fraction of detections as a function of the halo mass. Each plot contains results obtained with the three filter radii used in this work. The panels on the left show curves for sources at $z_s = 1$, the panels on the right for sources at $z_s = 2$. From top to bottom we have the APT, the OAPT and the OPT.

redshift sources. Similar results are obtained with the APT and the OAPT only for small apertures.

Figure 5.12 gives a global view of the halos detected, regardless of the their redshift.

In Fig. 5.13, we selected three mass bins ($M = 2.5 \times 10^{13} M_{\odot}/h$, $M = 5 \times 10^{13} M_{\odot}/h$, $M = 10^{14} M_{\odot}/h$) and determined the fraction of halos detected as a function of the redshift.

To reduce the noise, we binned together two lens planes as in Fig. 5.11. Yet, the results are still noisy, there is much variation for all the filters when the filter radius is changed, and the performance of the filters is quite similar in this respect. We see from the figure that the detected halos are preferentially located at low and moderate redshifts, due, as already said, to the geometry of the lensing strength.

5.3.6 Comparison with the peak statistics

The peak statistic counts peaks in convergence maps, e.g. obtained with the Kaiser-Squires inversion (see Kaiser & Squires, 1993; Kaiser, 1995), usually smoothed with a Gaussian kernel. Even though they used a different set of numerical simulations, we can safely compare our results with the peak-statistic analysis by Hamana et al. (2004), whose Gaussian kernel has a FWHM of 1 arcmin.

Fixing a detection threshold of $S/N > 4$ (5), Hamana et al. (2004) found $N \approx 6$ (2.5) detections per square degree, 60% (76%) of which correspond to real haloes with masses larger than $10^{13}\, h^{-1} M_{\odot}$. In our simulations, with the same S/N threshold and the optimal filter by Maturi et al. (2005), we found $N \approx 10$ (7), with an efficiency in detecting real haloes of 85% (95%). For halos with masses $M > 2 \times 10^{14}\, h^{-1} M_{\odot}$ ($M \approx 1 \times 10^{14}\, h^{-1} M_{\odot}$), the Hamana et al. (2004) sample is complete at the 70% (50%) level, which is virtually identical to the completeness of 70% $(50 - 60\%)$ achieved with the optimal filter.

5.4 Comparison with observations

The results outlined above show interesting differences between the performances of the filter functions. The discrepancies are particularly significant for high-redshift sources, indicating that the noise due to the LSS should become important only for deep observations. We can now attempt a quick comparison of our simulations with the observational results existing in the literature. In particular, we focus here on the searches for dark

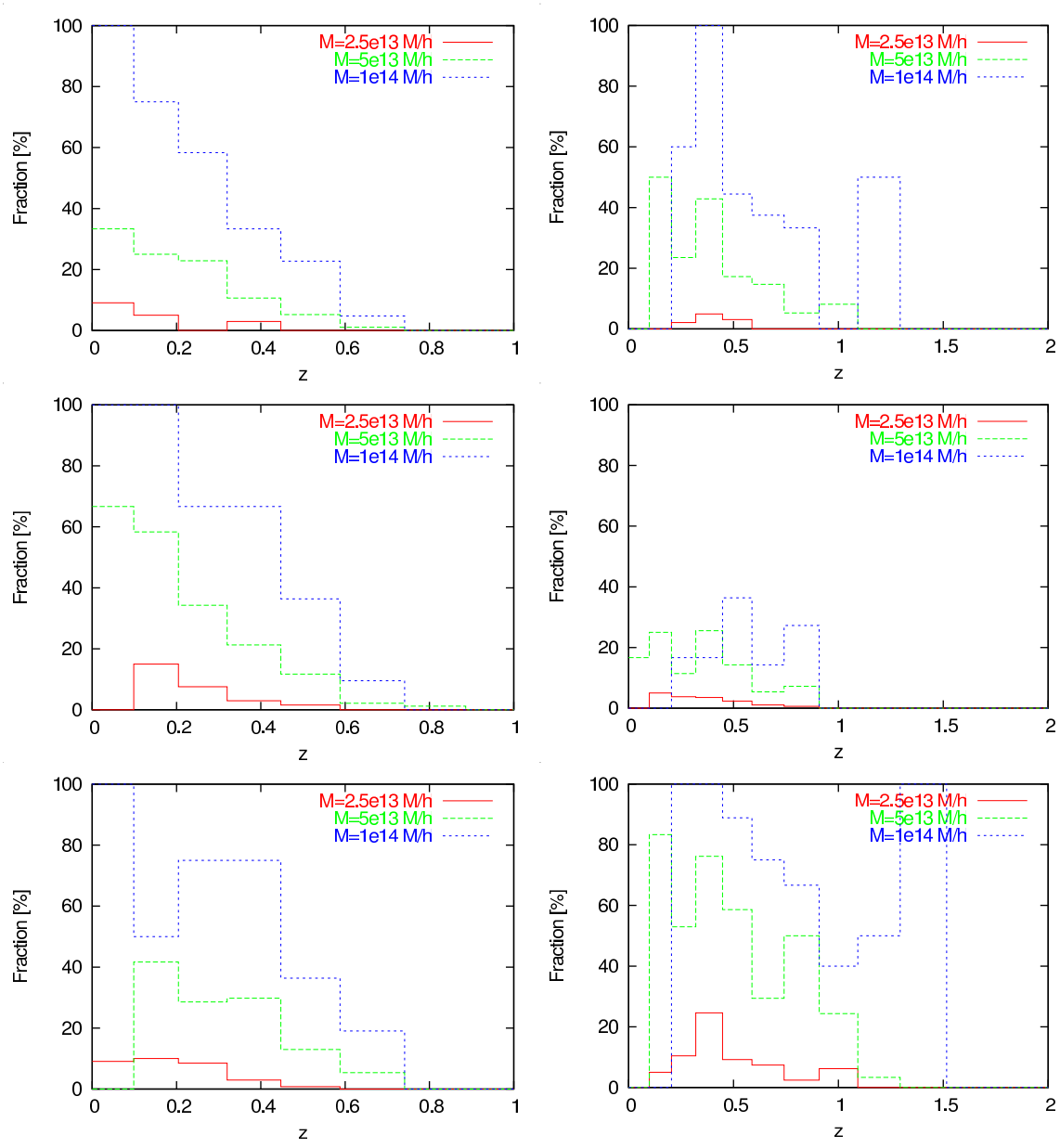

Figure 5.13: Fraction of halo detections with the APT, OAPT and OPT (from top to bottom) as a function of the halo redshift for three particular masses. The red line corresponds to a mass of $M = 2.5 \times 10^{13} M_{\odot}/h$, the green line to $M = 5 \times 10^{13} M_{\odot}/h$ and the blue line to $M = 10^{14} M_{\odot}/h$. The panels on the left show the results for sources at $z_s = 1$ and those on the right for sources at $z_s = 2$. From top to bottom, the filter radii are $r = 5.5'$ (for APT), $r = 10'$ (for OAPT) and $r = 2'$ (for OPT). Results for each redshift bin are averaged between two planes.

matter concentrations in the GaBoDS survey (Schirmer et al., 2003; Maturi et al., 2007).

To this goal, we perform a new set of ray-tracing simulations, where a realistic redshift distribution of the sources is assumed. In particular, we draw the sources from the probability distribution function

$$P(z) = N \exp[-(z/z_0)^{\beta}] \,, \tag{5.27}$$

where N is chosen such that

$$\int_0^{\infty} P(z)\, dz = 1 \,. \tag{5.28}$$

We adapt $P(z)$ to the redshift distribution of the sources in the GaBoDS survey by setting $z_0 = 0.4$ and $\beta = 1.5$ (Schirmer et al., 2003). In order to mimic the number density of galaxies in the GaBoDS observations, we assume $n_g = 10\,\mathrm{arcmin}^{-1}$.

By repeating the same analysis outlined above, we find results that are compatible with the results of Maturi et al. (2007). In particular, the number of detections with $S/N = 3.5$ per square degree in our GaBoDS simulations (in GaBoDS data) are $\simeq 5$ ($\simeq 4$) for the OPT with $r = 2'$, $\simeq 3$ ($\simeq 3$) for the OAPT with $r = 10'$ and $\simeq 1.5$ ($\simeq 2$) for the APT with $r = 5.5'$ ($r = 4'$) respectively. A comparison between the detections with different weak lensing estimators is shown in Fig. 5.14.

The fraction of spurious detections is large for all filters, but it is generally smaller for the OAPT and the OPT. As expected, the OAPT and the OPT estimators have similar performances, because of the small density of background galaxies. Indeed, the noise due to the intrinsic shape of the sources is dominant with respect to that due to the LSS and thus, according to Equation (5.20), the two filter functions have a very similar shape.

5.5 Summary and conclusion

We studied the performance of dark-matter halo detection with three different linear filters for their weak-lensing signal, the aperture mass (APT), the optimised aperture mass (OAPT), and a filter optimised for distinguishing halo signals from spurious signals caused by the large-scale structure (OPT). In particular, we addressed the questions how

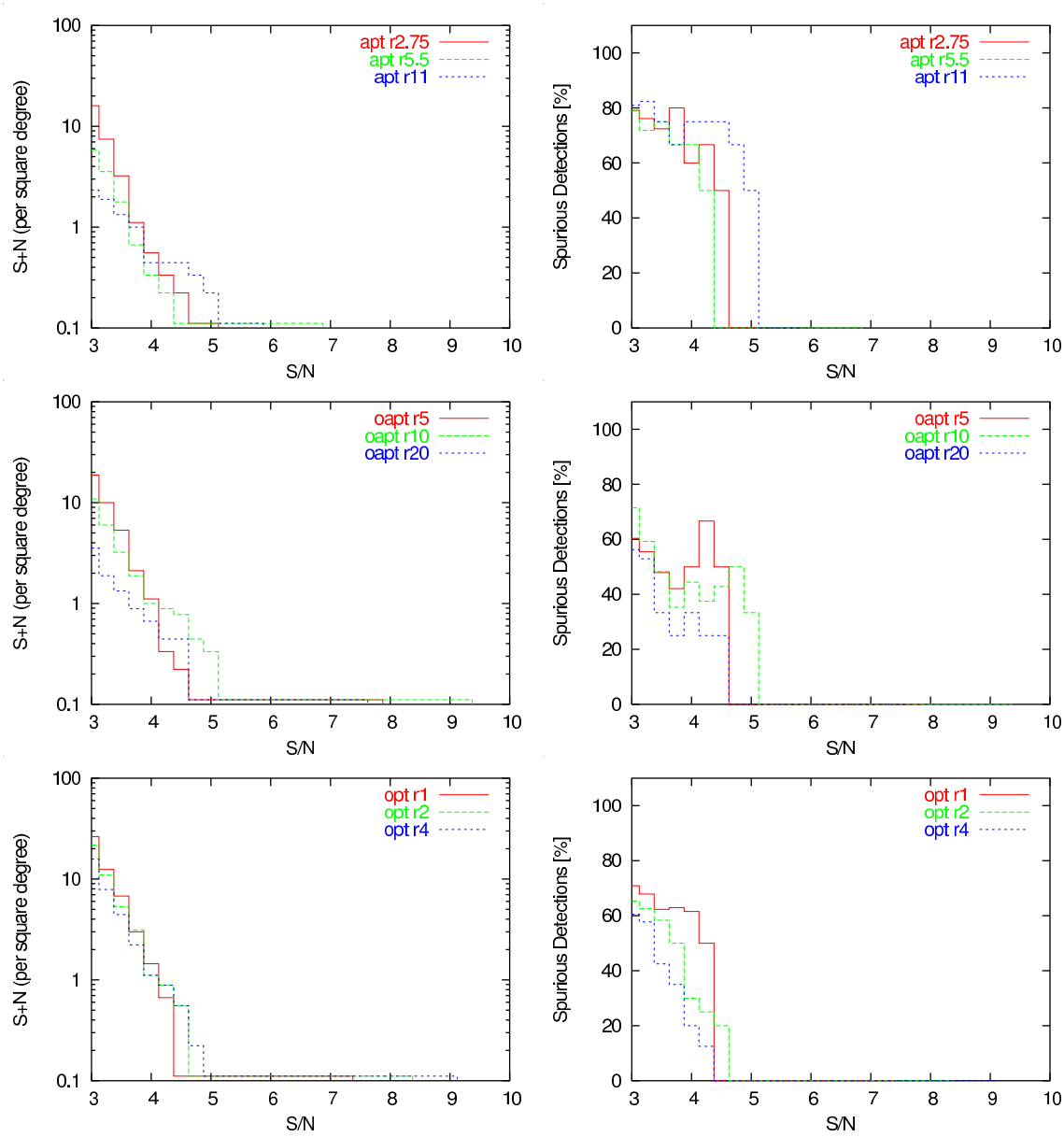

Figure 5.14: Total number of detections per square degree (left panels) and fraction of spurious detections (right panels) for sources distributed in redshift as in the GaBoDS survey (Schirmer et al., 2003). From top to bottom, we show the APT (for $r = 2.75'$, $r = 5.5'$ and $r = 11'$), the OAPT ($r = 5'$, $r = 10'$ and $r = 20'$) and the OPT ($r = 1'$, $r = 2'$ and $r = 4'$).

the halo selection function depends on mass and redshift, how the number of detected halos and of spurious detections depends on parameters of the observation, and how the filters compare.

To this end, we used a large N-body simulation, identified the halos in it and used multiple lens-plane theory to determine the lensing properties along a fine grid of light rays traced within a cone from the observer to the source redshift. Halos were then detected as peaks in the filtered cosmic-shear maps. By comparison with the known halo catalogue, spurious peaks could be distinguished from those caused by real halos. Our main results are as follows:

- We confirm that among those tested, the optimised filter (OPT) proposed by Maturi et al. (2005) performs best in the sense that its results are least sensitive to changes in the angular filter scale, it produces the least number of spurious detections, and it has the lowest mass limit for halo detection (cf. Figs. 5.10, 5.11 and 5.12).

- With the OPT filter, the fraction of spurious detections is typically $\lesssim 10\%$ for a signal-to-noise threshold of $S/N \approx 5$. It increases with source redshift due to the larger contamination by large-scale structure lensing (cf. Fig. 5.10).

- The number of halos detected per square degree by the OPT filter with $S/N \gtrsim 5$ is a few if the sources are at redshift $z_s = 1$, and ~ 20 for $z_s = 2$ (cf. Fig. 5.9).

- The minimum detectable halo mass starts at a few times $10^{13}\,h^{-1}\,M_\odot$ at redshifts ~ 0.1, drops to $\sim 10^{13} h^{-1}\,M_\odot$ near the optimal lensing redshift and increases towards $\sim 10^{14} h^{-1}\,M_\odot$ approaching the source redshift (cf. Fig. 5.11).

- The fraction of halos detected reaches $\sim 50\%$ at $\sim 2\times 10^{14} h^{-1}\,M_\odot$ and 100% at $\sim 4.5\times 10^{14} h^{-1}\,M_\odot$ with sources at $z_s = 1$. With more distant sources at $z_s = 2$, half of the halos with $\sim 7\times 10^{13} h^{-1}\,M_\odot$ are found, and all halos above $\sim 3\times 10^{14} h^{-1}\,M_\odot$ (cf. Fig. 5.12).

- Adapting parameters to the GaBoDS survey (Schirmer et al., 2003), and distributing sources in redshift, our simulation yields a number of significant detections per square degree which is in good agreement with what was found applying the OPT filter to the real GaBoDS data (Maturi et al., 2007).

Thus, the OPT filter, optimised for suppressing contaminations by large-scale structures, allows the reliable detection of dark-matter halos with masses exceeding a few times $10^{13}\,h^{-1}\,M_{\odot}$ with a low contamination by spurious detections.

Chapter 6

Statistical properties of SZ and X-ray cluster detections

Galaxy clusters provide a unique tool for cosmology. They trace efficiently the structure of the Universe on large scales (Eisenstein et al., 2005; Hütsi, 2006) and their mass function strongly depends on cosmological parameters (Weller & Battye, 2003; Sefusatti et al., 2007; Fang & Haiman, 2007). They can be studied at different frequencies, ranging from microwaves to X-rays and via weak and strong gravitational lensing (Clowe et al., 2004; Hennawi & Spergel, 2005; Tang & Fan, 2005). In particular, in the last years a strong effort has been devoted to study the SZ effect. SZ clusters can be observed up to high redshifts as the SZ effect is essentially redshift-independent. The physics behind this effect is well known. SZ observations can be carried out up to large distances from the cluster centers and are less sensitive than observations in the X-ray to the physical processes affecting the gas, like cooling, feedback, metal enrichment and so on (Carlstrom et al., 2002).

In the literature many different methods have been proposed to detected clusters through the SZ effect. Diego et al. (2002) used a method designed for Planck based on SExtractor (Bertin & Arnouts, 1996) while López-Caniego et al. (2006) and Herranz et al. (2002a,b) used a Scale Adaptive Filter. Methods based on wavelet filtering (Pierpaoli et al., 2005) or Monte Carlo Markov chains (Hobson & McLachlan, 2003) were also suggested. Schäfer et al. (2006) generalized scale adaptive and matched filters on the

sphere to apply them to Planck data.

The statistical properties of SZ detections in simulated maps have been investigated by several authors (López-Caniego et al., 2006; Melin et al., 2006; Vale & White, 2006; Schäfer & Bartelmann, 2006). All these works were based on semi-analytical models applied to cosmological $N-body$ simulations to trace the distribution of matter. However the gas physics was not included in past studies. This is known to affect several cluster properties, such as density profiles and shape (Kazantzidis et al., 2004; Puchwein et al., 2005).

X-ray surveys provide important information on the central regions of galaxy clusters and on the intracluster medium (ICM). They are also a good instrument to study the universe between $z = 0$ and $z = 1$, the period during which the expansion of the universe began to accelerate. Physical and statistical properties of galaxy clusters in the X-ray band are extensively studied employing hydrodynamical cosmological simulations where many gas-related physical effects are included.

In this chapter, we study the statistical properties of the detections of clusters in simulated maps via single- and multi-band matched filters. The multi-band filter is applied to SZ maps, while the single-band filter is applied to both SZ and X-ray maps. We study the completeness, the contamination and the sensitivity to the minimum detected mass of cluster catalogues. Then we cross correlate the cluster detections through both their X-ray and SZ signal.

In section 6.1 we describe the analytical model used to describe the signal, in section 6.2 we explain the procedure for creating SZ and X-ray maps and for adding noise. The single- and multi-band filter are described in section 6.3. In section 6.4 we analyze the properties of the synthetic catalogues for the single- and multi-bands filters while results on the correlation between SZ and X-ray detections are presented in section 6.5. Finally we summarize our main results in section 6.6.

6.1 A simple model for galaxy clusters: SZ and X-rays

To model the signal of galaxy clusters, we assume that the gas distribution follows a truncated King profile

$$\rho(x) = \frac{1}{1+x^2}\sqrt{\frac{|(r_t/r_c)^2 - x^2|}{1+x^2}} \text{ for } x \leq r_t \ , \tag{6.1}$$

where r_c is the core radius, r_t is the truncation radius defined as ten times the virial radius r_v and $x = r/r_c$. As described in Chapter 3, although based on the simple assumption that dark matter and gas follow a static and isothermal distribution, this profile is justified by simulations and X-ray observations.

The tSZ effect (equation 3.11) is proportional to the density ρ. It is normalized according to the integrated Compton parameter (equation 3.13) where the electron number is related to the cluster mass.

The X-ray luminosity is given by (Eke et al., 1998)

$$L_X \approx 1.2 \times 10^{-24} T^{1/2} n_P^2 V \ (erg/s), \tag{6.2}$$

where T is the gas temperature in keV, n_P the proton density in g/cm^3 and V the volume of the cluster in cm^3. As shown in Eq. 6.2, it is proportional to the square of the electron density and thus to the square of Eq. 6.1. It is normalized such that the bolometric luminosity follows the empirical relation by Kitayama & Suto (1997)

$$L_{X,bol} = 2.99 \times 10^{44} h^{-2} \left(\frac{T}{6\ keV}\right) \ erg/s \ , \tag{6.3}$$

where $T = T_{vir}(r_s)$ is the X-ray temperature. The luminosity in a given band is finally computed as

$$F_{band}^{[E_1,E_2]}(T) = \int_{x_{1,0}(1+z)}^{x_{2,0}(1+z)} C\, e^{-x} x^{-\gamma} dx \ , \tag{6.4}$$

where $x = E/(kT)$ ($E = h\nu$) and C is a normalization constant defined such that $\int_0^\infty C\, e^{-x} x^{-\gamma} dx = 1$. The subscript 0 in the integration boundaries means that the band

limits are taken in the observer rest-frame. The $1+z$ term is required for the K-correction. The function F_{band} represents the fraction of the flux in a given energy (frequency) interval.

6.2 The simulations

6.2.1 The cosmological simulation

To create a fairly realistic mock catalogue of SZ and X-ray halos, we use the outputs of a hydrodynamical cosmological simulation carried out using the code GADGET-2 (Springel, 2005). The SZ effect and X-ray properties of objects identified in this simulation have been studied in several works (e.g. Diaferio et al., 2005; Roncarelli et al., 2007; Ettori et al., 2004; Murante et al., 2004; Rasia et al., 2005; Roncarelli et al., 2006). The main characteristics of the simulation were described in Chapter 5. Here we briefly describe the implemented gas physics that turns out to be relevant for this study.

In order to study gas particles evolution, the simulation takes into account not only gravity, but also several physical processes that influence the physics of the intracluster medium. The implemented physics consists of:

- an hybrid multiphase model for the star formation in the interstellar medium that is parametrized as a two-phase fluid consisting of cold clouds and hot medium (Springel & Hernquist, 2003a);
- radiative cooling within an optically thin gas consisting of 76% hydrogen and 24% of helium by mass;
- supernova feedback to model galactic outflows;
- heating by a time-dependent, photoionising uniform UV background given by quasars reionising the Universe at $z \approx 6$ (Haardt & Madau, 1996).

The adopted supernova feedback includes the generation of metals from Type-II Supernova explosions. It is assumed that metals are instantaneously released during the

formation of new stars. Thus the effect of stellar life-times is neglected (for more details see Tornatore et al., 2004).

The output of the simulation consists of one hundred snapshots, logarithmically equi-spaced in redshift between $z_{ini} = 19$ and $z_{fin} = 0$. We use these snapshots to create our simulated light-cones.

To create a catalogue of halos from all snapshots, we run a friend-of-friend algorithm with a linking length of 0.15 times the mean particle separation. The complete description of the procedure was already given in Chapter 5.

To build a realistic three-dimensional distribution of matter, we construct several light cones stacking the snapshots of our cosmological simulation at different redshifts. Doing this, we pay attention to two aspects that were largely discussed in Chapter 5. Here we only summarize the most important points.

First of all we shift and rotate each snapshot to make it completely independent from the others. Second, since contiguous snapshots partially overlap in redshift, we resize the boxes such as to avoid to include the matter from more than one snapshot.

To create the maps, we proceed in two steps. We first project gas particles on a two dimensional grid and then we stack the resulting planes summing the contribution from each individual plane to get the final map. The opening angle of the light-cone is determined by the last plane of the stack. We consider light cones including matter up to redshift $z = 1$ and $z = 2$, corresponding to opening angles of 4.9 and 3.1 degrees, respectively.

To project gas particles on a regular grid, we use a method that takes into account the smoothing length of each particle and the SPH interpolating kernel used in the simulation. The method will be described in detail in appendix B. As the number of pixels onto which a particle is projected is not constant, the map has a smooth distribution and it is also consistent with the SPH formulation used in the N-body code. This same algorithm was applied by Puchwein et al. (2005) to study the impact of gas physics on strong lensing by clusters and by da Silva et al. (2000) to create simulated SZ-maps.

We construct our light-cones as done in Chapter 5, e.g. projecting all the box on a

regular grid and then selecting only the portion of plane embedded in the light cone. In other words, our planes have all the same number of pixels with constant comoving size, but the pixels contributing to the final map are only those entering the light cone. Thus the closest planes contribute very little. Other authors (see e.g. da Silva et al., 2000; Roncarelli et al., 2006), construct the light-cones keeping constant the angular resolution of the pixels, so each plane contributes the same amount of pixels, but in this way, due to the high number of pixels (2048×2048) the map resolution would exceed the physical resolution of the cosmological simulation.

As explained above, the SZ effect does ideally not depend on redshift, thus clusters can be observed up to moderately high redshifts through this effect. The X-ray luminosity of massive clusters ($M \sim 10^{15} M_{\odot}/h$) is of the order of $10^{44} \div 10^{45}$ erg/s, thus these emitters can be observed up to intermediate redshifts.

To create a map for the SZ effect we convert the integrals along the line of sight of Eq. 3.11 and 3.12 into a sum over gas particles. The contribution to the tSZ and kSZ effects of the i-th particle is thus

$$y_i = \frac{1}{L_{pix}^2} \frac{k_B \sigma_T}{m_e c^2} n_{e,i} T_i \tag{6.5}$$

$$b_i = \frac{1}{L_{pix}^2} \frac{\sigma_T}{c} n_{e,i} v_{r,i} \, , \tag{6.6}$$

where L_{pix} is the physical length of the pixel at the distance of the particle from the observer. We approximate the radial velocity $v_{r,i}$ with the velocity component along the z-direction and relate the temperature of gas particles T (in Kelvin) to their internal energy per unit of mass (U in km^2/s^2), by assuming that they form a monoatomic perfect gas

$$T = 10^6 \times \frac{2}{3k_B} m_p \mu U \, , \tag{6.7}$$

where m_p is the proton mass, $y_{He} \approx 0.08$ represents the mass ratio between the helium

and the hydrogen and the mean molecular weight is

$$\mu = \frac{1+4y_{He}}{1+y_{He}+n_e} \,. \tag{6.8}$$

The SZ contribution from each particle is given by Eq. 6.5 and 6.6. We project it using the same SPH kernel of the simulation (Monaghan & Lattanzio, 1985):

$$W(x) = \frac{40}{7\pi h^2} \begin{cases} 1-6x^2+6x^3, & 0 \leq x \leq 0.5, \\ 2(1-x)^3, & 0.5 < x \leq 1, \\ 0, & x > 1, \end{cases} \tag{6.9}$$

where $x = r/l$ is the ratio between the distance (r) from the center of the particle and particle smoothing length (l).

We create the light-cone maps for the X-ray emission in the following three bands: soft ($0.5 \div 2$ keV), hard ($2 \div 4$ keV) and hardest ($4 \div 10$ keV). We model the contribution from each particle to the X-ray emission in the soft and hard band with the MeKaL model (Mewe et al., 1995), as implemented in XSPEC. For the hardest band we use the model described in Borgani et al. (1999): since the influence from metal lines in the hardest band is negligible, a simple power-law parametrization is a good approximation. The MeKaL model parametrizes the emission spectrum from the hot diffuse gas and it is particularly suited for the soft band where the influence of the metal line emission is important. Using this model, the X-ray luminosity is

$$L_{X,i} = (m_p \mu)^{-2} m_i \rho_i x_e \Lambda(T_i, Z_i, E_1', E_2') \,, \tag{6.10}$$

where $x_e = n_e/n_H$ is the ratio between the number density of free electrons and hydrogen nuclei. The cooling function Λ depends on the particle temperature, on the metallicity and on the energy band interval $[E_1, E_2]$.

The model described in Borgani et al. (1999) parametrizes the band function given in Eq. 6.4 for each particle so that the i-th particle X-ray luminosity in the hardest band is

$$L_{X,i}^{hardest} \approx 1.7 \times 10^{42} \frac{m_i \rho_i \sqrt{T_i}}{\mu^2} \text{ erg/s} \,, \tag{6.11}$$

where m_i, ρ_i and T_i are the mass, the density and the temperature (in keV) of the i-th particle and μ is the mean molecular weight given in Eq. 6.8.

For each gas particle, the X-ray flux is defined as

$$I_{X,i} = \frac{L_{X,i}}{4\pi d_L(z)^2} \text{ erg/s/cm}^2 , \tag{6.12}$$

with $d_L(z)$ being the luminosity distance of the particle from the observer. As for the SZ maps, we project the X-ray flux on a regular grid using the same SPH kernel.

We repeated this procedure for each snapshot of the simulation, and then we sum up the contributions from all planes to obtain the final map. We create eleven different maps including matter up to redshift $z = 1$ and $z = 2$ with a resolution of 2048×2048 pixels. Indicating with p_i the value of a given quantity (SZ effects or X-ray flux) on each plane, the integrated value along the line of sight is $\sum_{i=1}^{N} p_i$, where N is the number of planes.

6.2.2 Simulating observations

We simulate observations with the Atacama Cosmology Telescope (ACT) for the SZ effect and with the space telescopes XMM-*Newton* and Chandra for the X-ray emission. We assume two different integration times, 30 ks and 100 ks.

Noise inclusion for the SZ map

In Fig. 6.1 we show the function $g_\nu(x)$ describing the frequency dependence of the tSZ effect. The crosses indicate the three frequencies at which ACT works. The $\nu = 225GHz$ channel is close to the frequency where the function $g_\nu(x)$ vanishes, so the major source of the signal will be due to the kSZ effect.

The noise in tSZ observations is given by three terms: the CMB radiation, the instrumental noise and the kSZ effect. The noise due to the CMB primary anisotropies and to the instrument are modelled as two independent Gaussian random fields. We used the CMB power spectrum as computed with the package CMBEASY (Doran, 2005) and the

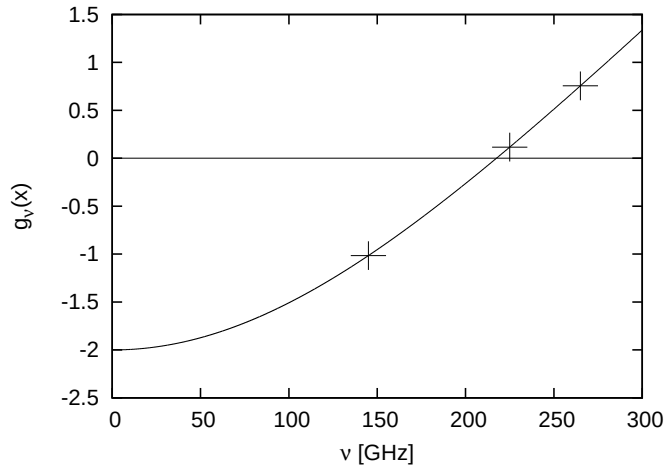

Figure 6.1: Frequency dependence of the tSZ effect. The three crosses show the frequencies at which ACT works. The frequency at which the tSZ effect is null is given by the interception between the horizontal line and the function $g_\nu(x)$.

instrumental noise power spectrum as given by

$$C_l^{noise} = w^{-1} \exp\left[\frac{l(l+1)FWHM^2}{8\ln 2}\right], \tag{6.13}$$

where $FWHM$ is the full width at half maximum of the instrument in arcmins, l is the multipole order and $w^{-1} \equiv (\Delta T/T\ FWHM)^2$. $\Delta T/T$ gives the sensitivity of the instrument on the scale of the beam (Knox, 1995). Finally the maps are convolved with the instrumental beam. Table 6.1 summarizes some parameters used to mimic observations with ACT.

Band (GHz)	FWHM (')	ΔT/beam (μK)
145	1.7	2
225	1.1	3.3
265	0.93	4.7

Table 6.1: Parameters used to mimic observations with ACT. In the first column we show the frequencies at which ACT works. In the second and in the third column we list the corresponding FWHM and sensitivity.

In the left panel of Fig. 6.2 we show a simulated tSZ map. In the right panel we

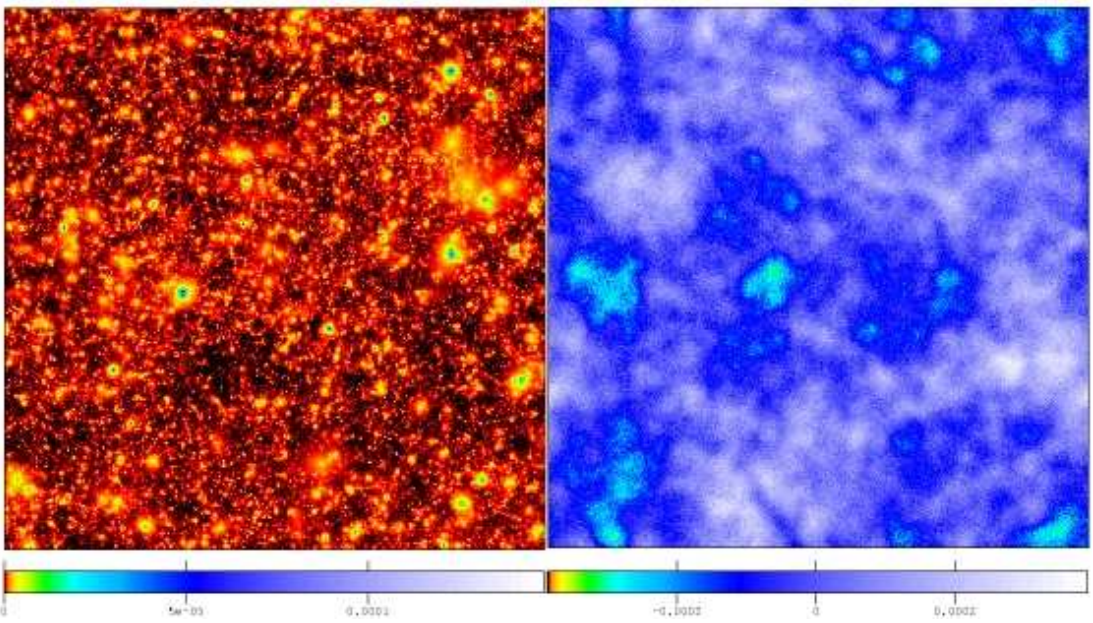

Figure 6.2: Maps of the SZ effect including cosmic structures up to redshift $z = 1$. On the left, we show the simulated map of the tSZ effect. On the right we show the same field as observed with ACT in the 145 GHz channel, including the kSZ effect, the CMB and the instrumental noise.

display the simulated observation with ACT in the $\nu = 145$ GHz channel, including the kSZ effect, the instrumental noise and the CMB primary fluctuations.

Noise inclusion for the X-ray maps

In order to transform our X-ray flux maps into X-ray count-rates, we first multiply the flux maps by the energy conversion factor of the instrument. For each energy band, the energy conversion factor is computed by assuming a spectral model, consisting of a thermal bremsstrahlung with $k_B T = 4\ keV$. The spectral model is then convolved with the response matrices of the EPIC-PN detector on board of the X-ray telescope XMM-*Newton* and the ACIS-I array on board of *Chandra*. By assuming a certain exposure time (30 and 100 ks), we transform our count-rate maps into count maps. The background of a X-ray observation is given by the sum of the detector noise and the unresolved X-ray background. We added this quantity to the photon count maps. Finally we convolved the resulting maps with the point spread function (PSF) of the instrument (5 and 0.5 arcsec

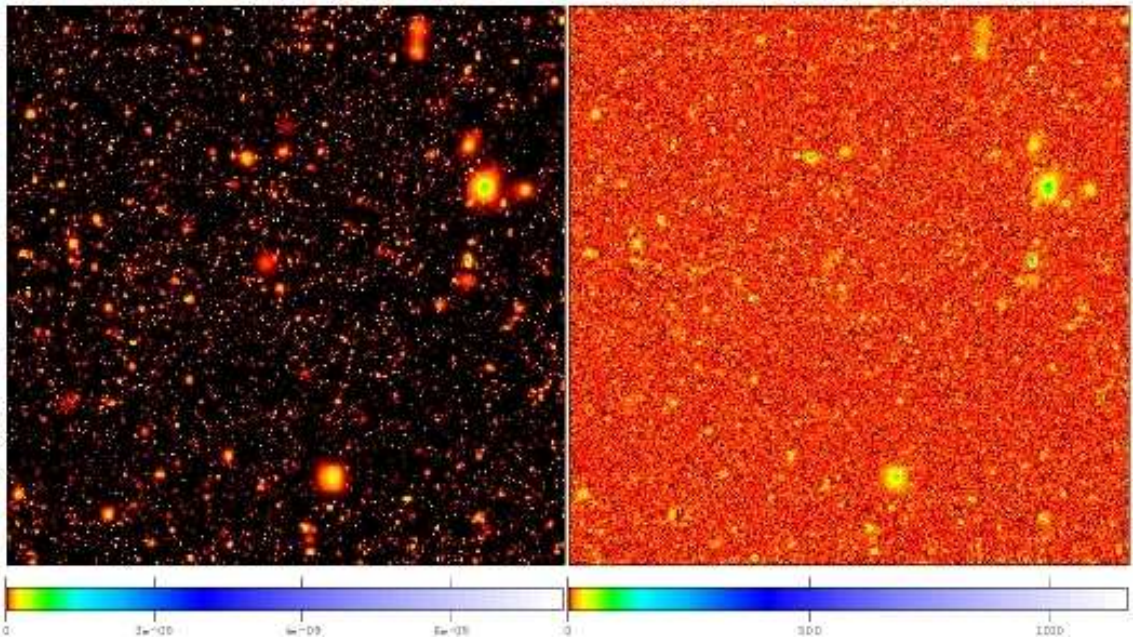

Figure 6.3: Left panel: map of the X-ray flux in the soft band for the same structures shown in Fig. 6.2. Right panel: simulated observation with XMM-*Newton*, assuming an exposure time of 30 ks.

for XMM-*Newton* and Chandra, respectively). In order to reproduce the noise of the observations, we added Poissonian noise.

In table 6.2 we summarize the noise levels used in the simulated observations with XMM-*Newton* and Chandra.

Instrument	Band	Noise (counts/sec/deg^2)
XMM-*Newton*	Soft	24.624
	Hard	11.
	Hardest	19.64
Chandra	Soft	2.96
	Hard	2.47
	Hardest	7.4

Table 6.2: XMM-*Newton* and Chandra noise levels.

A simulated X-ray map for the soft band is shown in the left panel of Fig. 6.3. The simulated observation with XXM-*Newton*, including background, instrumental and Pois-

sonian noise is shown in the right panel. An exposure time of 30 ks is assumed. The maps assume the same underlying mass distribution as in Fig. 6.2.

6.3 Filtering method

In this section we describe the matched filter used to detect clusters in the simulated maps. In the X-ray observations, the noise in a given band is not correlated with the noise in other bands or with the noise in SZ observations, therefore the multi-band filter will be applied only to the SZ observations.

6.3.1 Single-band filter

The single-band filter we use is analogous to the optimal filter described in section 5.2.2. Here we only give the basics concepts.

As in Eq. 5.16 we suppose that the observed data $D(\vec{\theta})$ is given by the signal from the source $S(\vec{\theta}) = A\hat{\tau}(\vec{\theta})$ and the noise $N(\vec{\theta})$. The estimate of filtered signal is given by Eq. 5.17. The optimal filter has to satisfy two conditions: it has to be unbiased (Eq. 5.18) and the variance, defined in Eq. 5.19, has to be minimal with respect to the signal. The filter is given as solution of a variational problem with the two previous described constraints (see Haehnelt & Tegmark, 1996):

$$\hat{\Psi}(\vec{k}) = \frac{1}{(2\pi)^2}\left[\int \frac{|\hat{\tau}(\vec{k})|^2}{P_N(k)}\, d^2k\right]^{-1} \frac{\hat{\tau}(\vec{k})}{P_N(k)}\,, \tag{6.14}$$

where the hats denote the Fourier transform. Eq. 6.14 shows that the shape of the filter Ψ is determined by the shape of the signal, τ, and by the power spectrum of the noise, P_N. Eq. 6.14 is completely analogous to Eq. 5.20.

6.3.2 Filter dependence on the template

In Fig. 6.4 we show the profile of the filter used in the SZ observations at 145 GHz (upper panels) and in the X-ray observations for the soft band (lower panels). In the left plot, we assume a template with mass $M = 10^{13}\ M_{\odot}/h$ and we show the filter dependence on

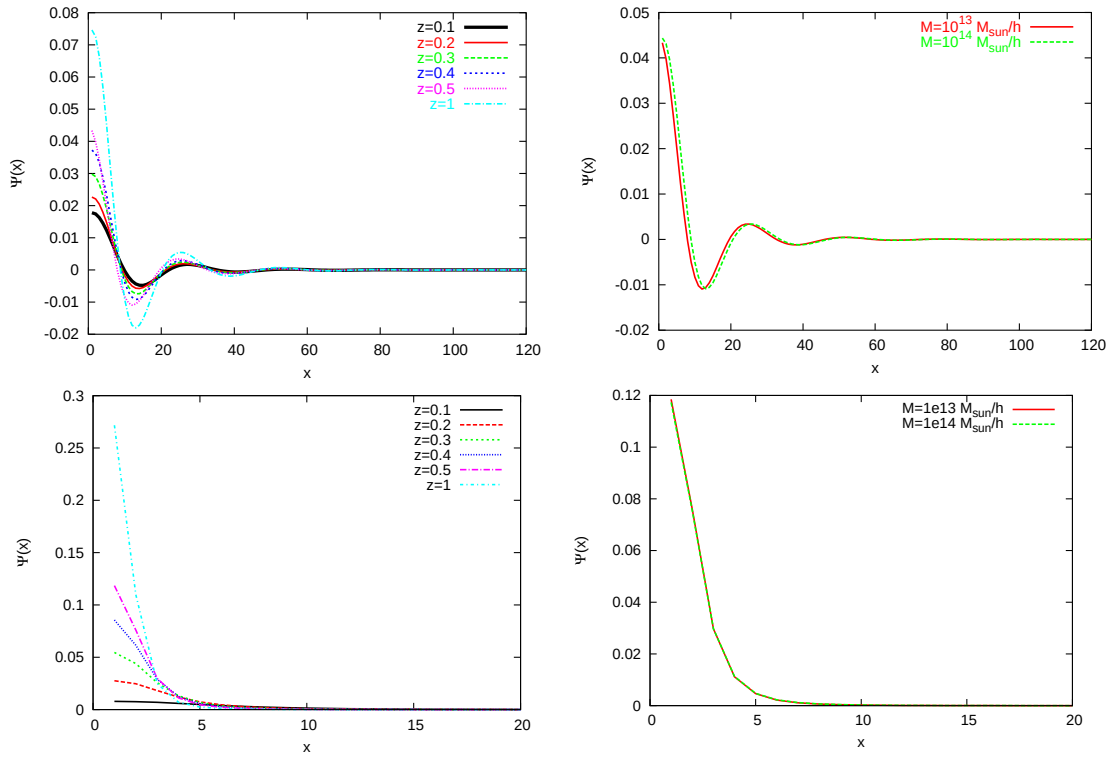

Figure 6.4: In the left figure we show the profile of the matched filter for different redshifts assuming a fixed mass of the template of $M = 10^{13}\ M_{\odot}/h$. The right figure shows the profile of the filter for different masses $M = 10^{13}\ M_{\odot}/h$ (red line) and $M = 10^{14}\ M_{\odot}/h$ (green line) of the template, assuming a fixed redshift of $z = 0.5$.

the cluster redshift. In the right panel, we fix the redshift of the template at $z = 0.5$ and we show the profile of the filter for two different masses: $M = 10^{13}\ M_{\odot}/h$ (red line) and $M = 10^{14}\ M_{\odot}/h$ (green line). The upper right panel shows that the profile of the SZ filter is insensitive to the mass of the template, while the left panel shows that the amplitude of the damped oscillations increases by increasing of the cluster redshift, although its shape remains essentially the same. This implies that the filter shape, and thus its sensitivity, are independent on the particular choice of the template.

This property depends on the shape of the power spectrum of the noise, which is due to the instrument and to the CMB. Since their power spectra are both redshift- and mass-independent, the minimum of the noise (and therefore the maximum of the filter)

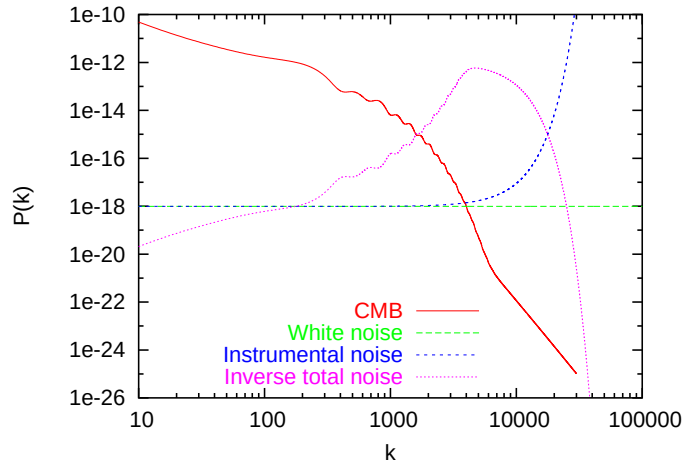

Figure 6.5: Noise power spectra. The red curve shows the CMB power spectrum, the green line the white noise, the blue line the instrumental noise and the violet curve the inverse of the total noise (opportunely scaled), given by the sum of the CMB noise and of the instrumental noise. The filter is proportional to the inverse of the total power spectrum.

is always at the same wave number, as shown in Fig. 6.5. Consequently the filter selects these frequencies for each cluster model assumed.

Differently from the SZ filter, the X-ray filter (lower panels in Fig. 6.4) is proportional to the template because the noise is white. Thus, changing the template, the filter changes more dramatically.

6.3.3 The multi-band matched optimal filter

In this section we briefly describe our multiband matched filter. This filter allows to combine information from different bands. For a more complete derivation we refer to Schäfer et al. (2006) and Melin et al. (2006) and references therein. Generalizing the single-band case, the data obtained at a given frequency ν are written as

$$D_\nu(\vec{\theta}) = S_\nu(\vec{\theta}) + N_\nu(\vec{\theta}) \,, \tag{6.15}$$

where $S_\nu(\vec{\theta})$ and $N_\nu(\vec{\theta})$ are the signal and the noise component at the band ν. The signal is modelled as

$$S_\nu(\vec{\theta}) = A f_\nu \tau_\nu(\vec{\theta}) \,, \tag{6.16}$$

where A is the (band independent) amplitude, f_ν is the frequency dependence of the amplitude and $\tau_\nu(\vec{\theta})$ is the spatial profile normalized to unity. The index ν runs from one to M, where M is the number of available bands. We assume that the background noise has zero mean in each band and that its statistical properties are fully characterized by the correlation function

$$C_{\nu_1\nu_2} = \langle \hat{n}_{\nu_1}(\vec{k}) \hat{n}_{\nu_2}(\vec{k}')^* \rangle = (2\pi)^2 \delta(\vec{k} - \vec{k}') P_{l,\nu_1\nu_2}(k) \,, \tag{6.17}$$

where $P_{l,\nu_1\nu_2}(k)$ is the cross-power spectrum.

To measure the signal amplitude A, we define a linear estimator for each band

$$A_{\mathrm{est},\nu}(\vec{\theta}) = \int d^2\theta' D_\nu(\vec{\theta}') \Psi_\nu(|\vec{\theta}' - \vec{\theta}|) \,, \tag{6.18}$$

so that the final estimate is given by

$$A_{\mathrm{est}} = \sum_{\nu=1}^{M} A_{\mathrm{est},\nu}(\vec{\theta}) \,. \tag{6.19}$$

Here $\Psi(\vec{\theta}) = \left[\Psi_\nu(\vec{\theta})\right]$ is the optimal filter which is constructed such that the estimated variance

$$\sigma_u = \langle (A_{\mathrm{est}} - \langle A \rangle)^2 \rangle \,, \tag{6.20}$$

is minimal and such that the estimated amplitude is unbiased, i.e. the average error on the estimate amplitude must vanish

$$b \equiv \langle A_{est} - A \rangle = 0 \,. \tag{6.21}$$

When deriving the filter we define vectors where each band corresponds to a vector element. We thus define the filter vector $\bar{\Psi} = \left[\Psi_\nu(\vec{\theta})\right]$ and the signal vector $\bar{\mathbf{F}} = [F_\nu]$. We further define the cross power spectrum matrix $\mathbf{C} = [C_{\nu_1\nu_2}]$.

The filter which satisfies these conditions is the one which minimizes the Lagrangian $L = \sigma^2 + \alpha b$

$$\Psi = \alpha \mathbf{C}^{-1}\mathbf{F}\,, \tag{6.22}$$

where $\mathbf{C}^{-1}$ is the inverse of the matrix $\mathbf{C}$ and α is a Lagrangian multiplier given by

$$\alpha^{-1} = \mathbf{F}^{\mathrm{T}}\mathbf{C}^{-1}\mathbf{F}\,. \tag{6.23}$$

The estimate variance is given by

$$\sigma^2 = \int \frac{d^2k}{(2\pi)^2}\Psi^{\mathrm{T}}\mathbf{P}\Psi\,. \tag{6.24}$$

Eq. 6.22 shows that the matched filter depends on the noise, taking advantage of its correlation between all the bands. In the particular case $P_{\nu_1\nu_2} = P_{\nu_1}\delta(\nu_1 - \nu_2)$, i.e. in the case of non correlated noise, the matrix $\mathbf{C}$, and therefore its inverse, is diagonal and the optimal filter for each band would have the same shape of the single-band filter defined in Section 6.3.1. Only the normalization would differ.

6.4 Statistics of the detections

We now analyze a set of eleven SZ and X-ray simulated maps with the single-band and the multi-band filters described in section 6.3.1 and 6.3.3, respectively and we perform a statistical analysis of the obtained sample.

In analogy with Chapter 5, we define a *detection* as a group of pixels in the SN map whose values are above a certain threshold. The position of the detection on the sky is associated to the most significant pixel. A true detection is a detection that can be associated to a halo of the Λ-CDM simulation, while a spurious detection is a detection caused by noise due to the LSS, to the CMB or the to X-ray background.

Again we distinguish the true from the spurious detections by searching for those detections that are caused by mass concentrations confined on a single plane (see Chapter 5 for more details).

6.4.1 SZ single-band detections

Due to the oscillatory behaviour of the single band filter (see upper panels in Fig. 6.4), detections consist of positive SN peaks surrounded by negative and positive ring-like structures. Typically, those rings are fragmented by noise and show up as secondary SN peaks surrounding the most prominent detections. These secondary peaks can be easily confused with true detections. Some examples can be seen in the upper left panel of Fig. 6.6. Consequently we need to model and include in our noise estimate these correlated noise structures. This is possible because we can easily estimate their expected shape and amplitude, which results from the convolution of the signal with the oscillatory pattern of the filter (see Fig. 6.4).

The noise map is thus obtained with an iterative approach. First we compute the SN maps by applying the filter and estimating the noise through Eq. 5.19. Second we detect the most prominent detection, compute the correlated noise pattern as explained and include it in the noise map. Then we use this new noise estimate to compute the updated SN map, detect the second most prominent detection and reiterate the procedure. The noise map resulting from this procedure is shown in the lower panel of Fig. 6.6. The upper right panel of Fig. 6.6 shows the same detections displayed in the left panel after removing the filter artifacts.

In upper panel of Fig. 6.7 we show the total number of detections per square degree in our ACT simulations. Results are shown in all three channels and for both the light-cone limiting redshifts. The fractions of spurious detections are shown in the bottom panels. Results are averaged over eleven maps corresponding to $24.5\,deg^2$ and $9.5\,deg^2$ for limiting redshifts $z = 1$ and $z = 2$ respectively.

As expected, at $\nu = 225$ GHz we find few detections. At this frequency, the tSZ effect is indeed very modest, while the kSZ dominates the signal. As the SZ effect does ideally

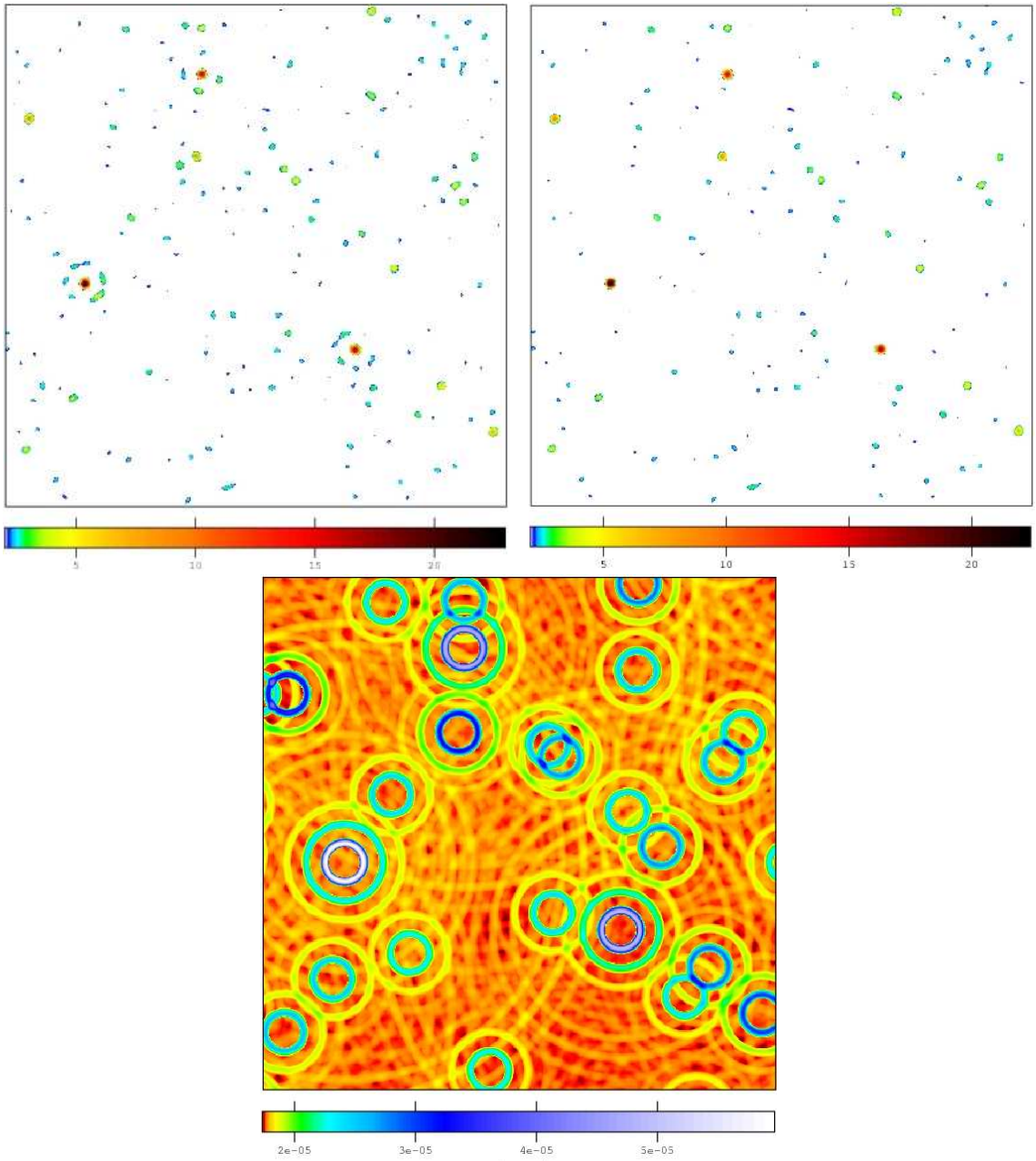

Figure 6.6: SN ratio maps (upper panels) and noise (lower panel) illustrating the procedure to suppress artificial structures from the filtered SZ maps. The upper left panel shows detections at $SN \geq 2$ as obtained by the filter and the upper right panel shows the same SN map after the removal of the spurious ring artifacts. The lower panel shows the resulting noise map that takes into account the damped oscillations of the filter. The side of the maps 2.5 degrees.

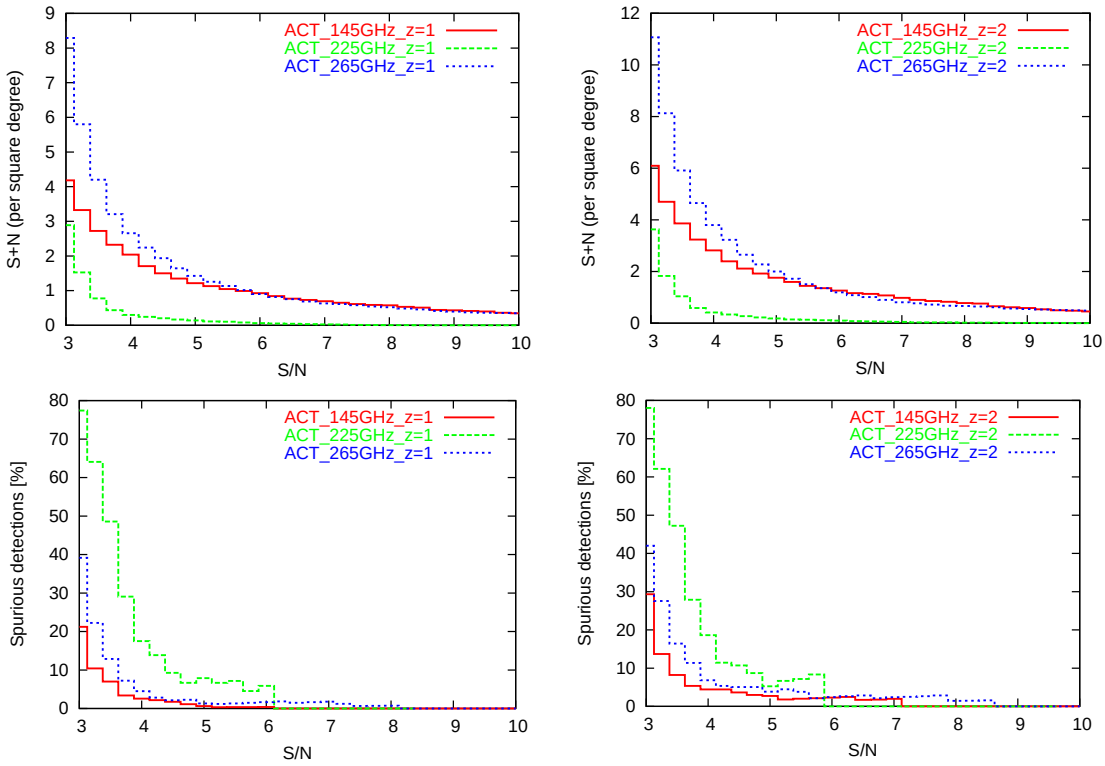

Figure 6.7: Number of total detections per square degree (upper panels) and fraction of spurious detections (bottom panels) as a function of the S/N ratio. Results are shown for redshift $z = 1$ (left panels) and $z = 2$ (right panels). Different line styles refer to the different bands used, $\nu_1 = 145$ GHz, $\nu_2 = 225$ GHz, $\nu_3 = 265$ GHz. The plots are obtained averaging over eleven maps.

not depend on redshift, but only on the time evolution of the sources, we also see that we find more objects for a light-cone extending up to redshift $z = 2$ than for a light-cone with objects till redshift $z = 1$. At frequencies $\nu = 145$ GHz and $\nu = 265$ GHz we find at least 30% more detections in the deepest light-cone. The major differences in these two bands are for low signal-to-noise ratios, where we notice that more structures are detected in the highest-frequency band. This is due to the higher sensitivity of the instrument. For $S/N \geq 5$, the number of detections is similar in both bands.

Because of the small tSZ effect amplitude, the fraction of spurious detections at $\nu = 225$ GHZ is very high ($\approx 80\%$ for $SN \approx 3$), practically independent from the limiting redshift of the light-cone. For the maps at $\nu = 145$ GHz and $\nu = 265$ GHz at $z = 1$ ($z = 2$)

we find that respectively 20% and 40% (30% and 40%) of the detections at $S/N \approx 3$ are spurious. Once again, for relatively high SN ratios, the two bands perform similarly. For $S/N > 4$, the fraction of spurious detections is of the order of few percent. Including matter up to redshift $z = 2$ in the light-cone, the slightly higher fraction of spurious detections increases due to the overlapping of structures not resolved. In addition, the number of large S/N detections does not increase with the depth of the light cone (as the massive structures responsible for the them are localized at low redshifts), but the number of small S/N detections is enhanced (up to a factor of five for the least massive halos).

In Fig. 6.8 we show the fraction of halos in the light cone detected in different bands as a function of the mass (upper panels) and the sensitivity of the catalogue, i.e. the minimum mass detected at each redshift (lower panels). In the left and in the right panel we show the results for light-cones up to $z = 1$ and $z = 2$, respectively. The values given are averaged over eleven realizations. The sensitivity is computed by combining two planes together to reduce the noise. It is defined as the mean mass of the ten least massive halos detected in the redshift bin.

As the SZ effect does ideally not depend on the redshift on the source, the completeness for detections up to $z = 1$ and $z = 2$ is essentially the same. The two channels at 145 GHz and 265 GHz perform equally well, while for the channel at 225 GHz the completeness is much lower. The minimum detected mass is $M \simeq 7 \times 10^{13} M_{\odot}/h$ and the completeness reaches 100% for masses $M \simeq 3 \times 10^{14} M_{\odot}/h$. The slope of the curve is quite steep, therefore the degree of completeness decreases rapidly. Already for masses of $M \simeq 1.5 \times 10^{14} M_{\odot}/h$ the completeness is approximately 50%.

The sensitivity (lower panels of Fig. 6.8) reflects the fact that the SZ effect does not depend on the object redshift, in fact the minimum mass detected is basically redshift independent. The results on the sensitivity agree with those on the completeness, as expected, at 225 GHz the method is less sensitive than in the other two channels. In addition we see that the filter finds halos with a lower mass at 265 GHz than for the filter at 145 GHz (blue and red curve respectively), explaining the larger completeness of the former

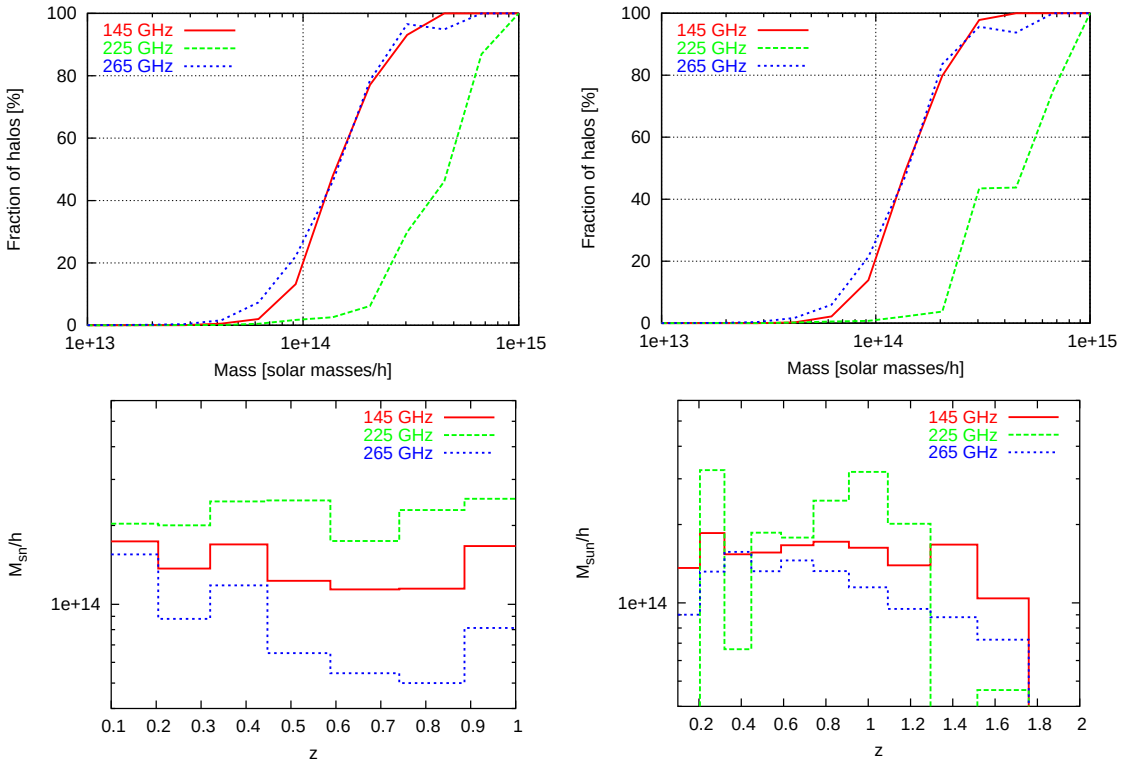

Figure 6.8: Upper panels: Fraction of detected halos as a function of the halo mass. Bottom panels: sensitivity of the method. The panels on the left and on the right refer to the results for limiting redshifts of the light-cones of $z = 1$ and $z = 2$, respectively. Different curve styles refer to the three different band of ACT. The curves are averaged over eleven maps.

band.

Similar results were found by López-Caniego et al. (2006) using the same approach to detect clusters in simulated Planck observations. For low detection limits (corresponding to low S/N ratios), López-Caniego et al. (2006) found a very high fraction of spurious detections, that decreases quite fast by increasing the flux limit. The comparison of the results can be done only in a statistical sense, since the instrument and the frequencies are very different. In particular, only two channels used by López-Caniego et al. (2006) have a frequency range close to those of ACT. Moreover, we consider S/N ratios and not fluxes, and we include in the noise map the correlated ring patterns due to the oscillatory filter behaviour.

6.4.2 Statistics of SZ multi-band detections

We discuss now the application of the multi-band filter described in Section 6.3.3 to the simulated observations in the three channels of ACT.

In Fig. 6.9 we show the S/N maps obtained by applying each component of the multi-band filter to the three channels at 145 GHz (upper left panel), 225 GHz (upper right panel) and 265 GHz (bottom left panel). The final result is obtained by combining them using Eq. 6.19 to give the S/N map in the bottom right panel.

Compared to the results from using a single band filter, the S/N ratios are now enhanced by at least a factor of three.

The S/N peaks in the map have been identified using SExtractor (Bertin & Arnouts, 1996), that allows to easily deblend nearby detections. We analyze the results similarly to what done for the single band filter. First, we count the detections above a minimal S/N ratio, starting from $S/N_{min} = 3$. The number counts per squared degree as a function of the minimal S/N are shown in the upper left panel of 6.10. The solid and the dashed lines refer to the simulations including matter up to $z = 1$ and $z = 2$, respectively. Comparing with the previous results, the multi-band filter performs similarly to the single-band filter in the 265 GHz channel. The number of detections is only slightly less ($\sim 15\%$). This might be caused by the larger area of the multi-filter detections which cause a larger blending which is not entirely removed by SExtractor and by the fact that the sample contamination is lower as we are going to see. Similar results are found for the two redshift limits of the light cones.

In the top-right panel of Fig. 6.10, we show the fraction of spurious detections in the final catalog. Comparing again with the previous results with the single band filter, we clearly see the great advantage of combining multiple observations. While the fraction of spurious detections in the 265 GHz channel is $\sim 40\%$ at $S/N = 3$ and was dropping to $\sim 5\%$ at $S/N \sim 5$, by filtering the observations simultaneously in the three channels, the fraction of spurious detection is now at the level of few percent already at very low S/N ratios. Thus, the vast majority of the detections in the top-right panel are true.

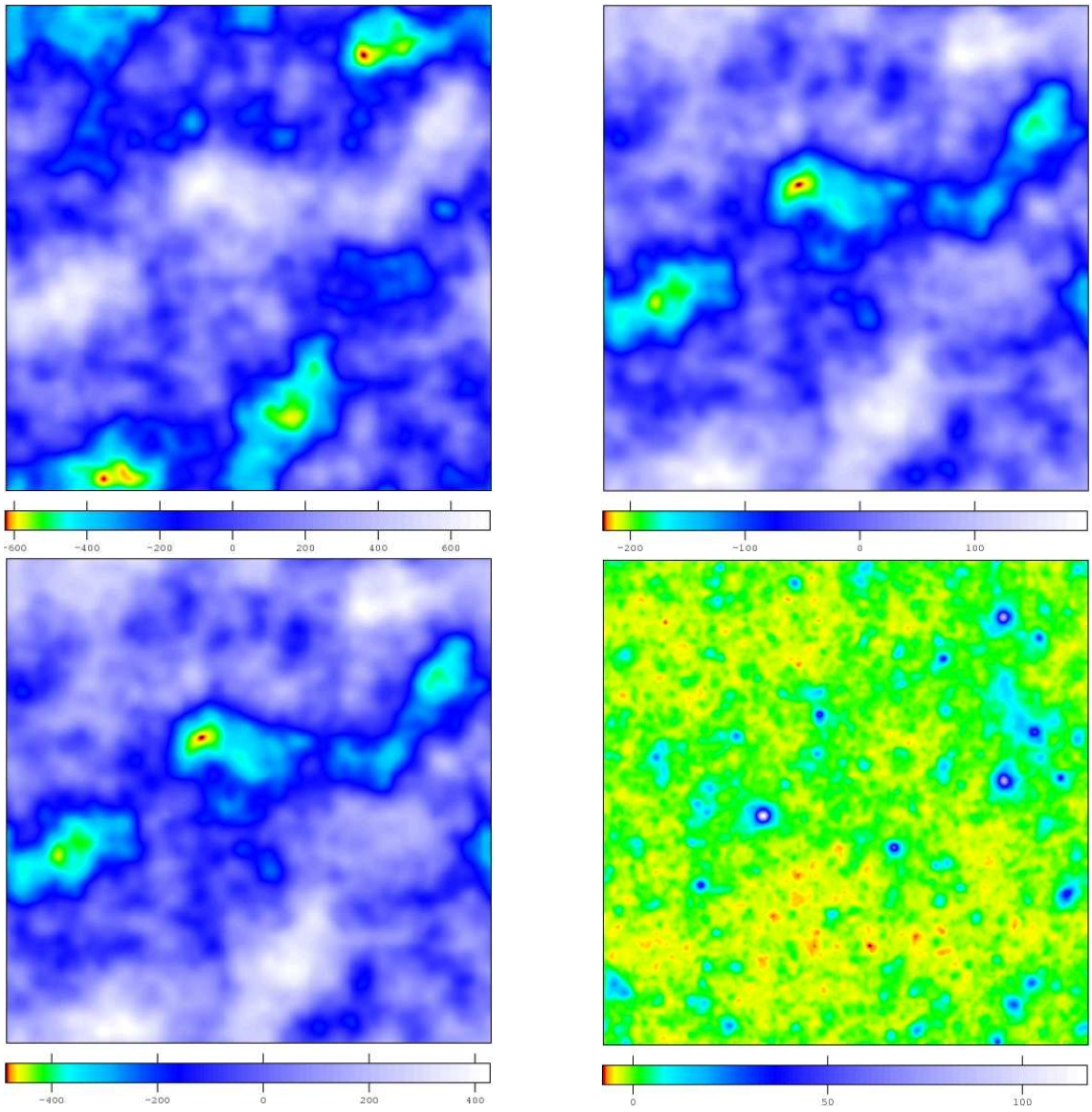

Figure 6.9: Example of the reconstruction of a SN map for the matched filter starting from the noisy map. The upper panels show the filtered maps for the frequency of 145 GHz (left panel) and 225 GHz (right panel). The lower panels show the filtered map at 265 GHz (left panel) and the final SN map, obtained summing together the other three maps. The region of sky shown here is the same as in Fig. 6.2 and 6.3.

The completeness of the catalogue is shown in the bottom left panel of Fig. 6.10. We find that 20%, 50% and 80% of the halos of mass larger than $7 \times 10^{13} M_{\odot}/h$, $\sim 10^{14} M_{\odot}/h$ and $2 \times 10^{14} M_{\odot}/h$ contained in the light cones are detected by the multi-band

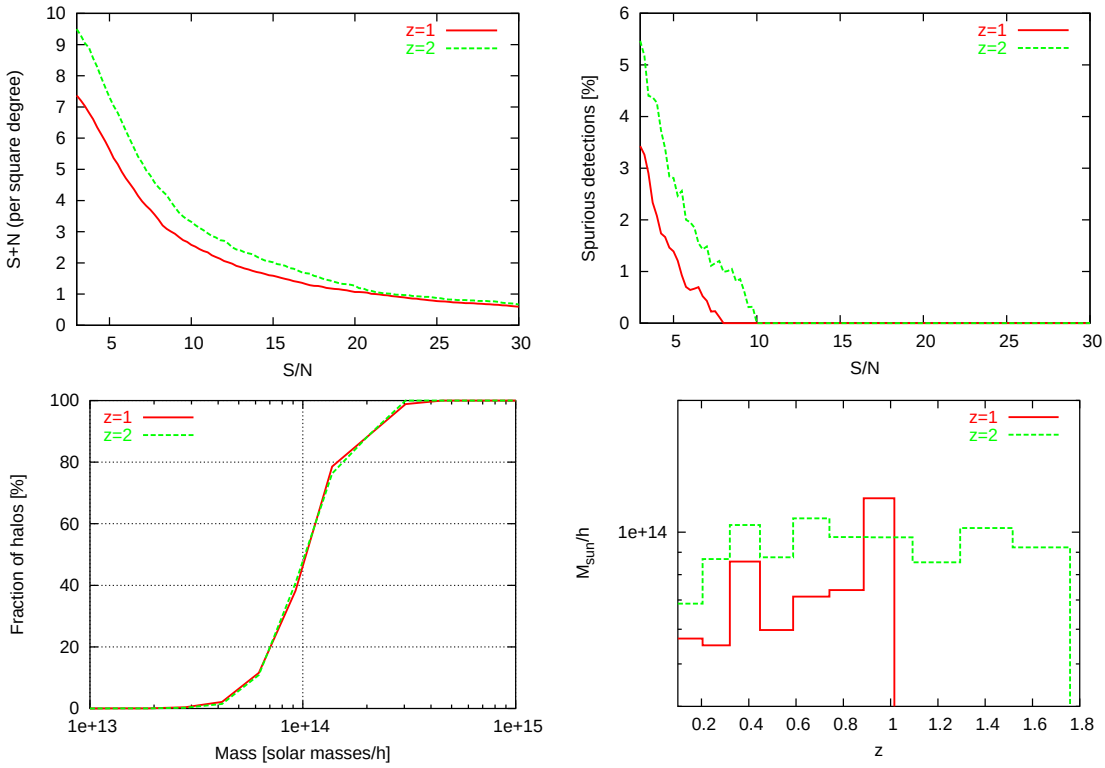

Figure 6.10: Upper-left panel: total number of detections per square degree as a function of the minimal S/N ratio, using the multi-band filter. Upper-right panel: fraction of spurious detections as a function of the minimal S/N. Bottom left panel: fraction of detected halos as a function of their minimal mass. Bottom right panel: minimal mass detected as a function of redshift. The red and the green curves shows the results for light cones extending to $z = 1$ and $z = 2$ respectively.

filter, respectively. In contrast, in the previous analysis based on the single-band filter, we were able to detect only $\sim 20\%$ of the halos with mass larger than $10^{14} M_{\odot}/h$ in the 145 GHz and in the 265 GHz channels.

White & Kochanek (2002) used a dark matter-only cosmological simulation to model the spatial distribution of clusters and the galaxies they look for are added according to a variant of the halo model. A luminosity drawn from a Schechter function is associated to each galaxy. This was done so that galaxies could trace the cluster distribution. White & Kochanek (2002) found that their catalogues are complete for masses above $M \sim 2 \times 10^{14} M_{\odot}/h$ using in addition information based on photometric redshifts. The matched filter we used shows better performance as we found similar values but without

any additional information.

Finally, the minimal masses that could be detected using the multi-band filter are shown as a function of redshift in the bottom right panel of Fig. 6.10. As expected, the curves show a very weak dependence on redshift, although the values seem to increase weakly until redshift one. The minimal mass per redshift bin ranges between $\sim 6 \times 10^{13} M_{\odot}/h$ at $z = 0$ and $\sim 9 \times 10^{13} M_{\odot}/h$ at $z = 1.8$. We notice again that using a multi-band filter also improves the sensitivity of the method. Indeed, using a single-band filter, masses larger than $5 \times 10^{13} M_{\odot}/h$ could be detected only in the 265 GHz channel.

We conclude this section by comparing our results to an other independent work employing multi-band filtering. Melin et al. (2006) used a multi-band matched filter for analyzing Monte-Carlo simulations. Assuming to observe the SZ effect with the South-Pole-Telescope (SPT), they made a statistical study of the detections similar to the one we described above. Since the frequencies at which the SPT works and the FHWM of its beam are similar to those of ACT, a fair comparison between our and their results can be attempted. They found 17 detections per square degree at $S/N > 3$ and 6 detections per square degree at $S/N > 5$, very close to the values we find (9.5 and 8 detections per square degree at $S/N > 3$ and $S/N > 5$, respectively). The smallest masses that they can detect is a factor of three larger than those found by our filter in the simulated observations by ACT. This is fully expected, given the larger noise level of SPT compared to ACT. Finally, the contamination by spurious detections in the catalogs by Melin et al. (2006) is similar to the one we measure in our catalogs of detections.

6.4.3 X-ray detections

We now analyze the statistical properties of the X-ray detections obtained with the single-band filter.

In Fig. 6.11 we show the total number of detections per square degree found in the simulated X-ray maps. Results for limiting redshifts of the light-cones of $z = 1$ and $z = 2$ are shown in the left and in the right panel, respectively. From top to bottom we report detections in the soft, hard and hardest bands. The results are averaged over eleven dif-

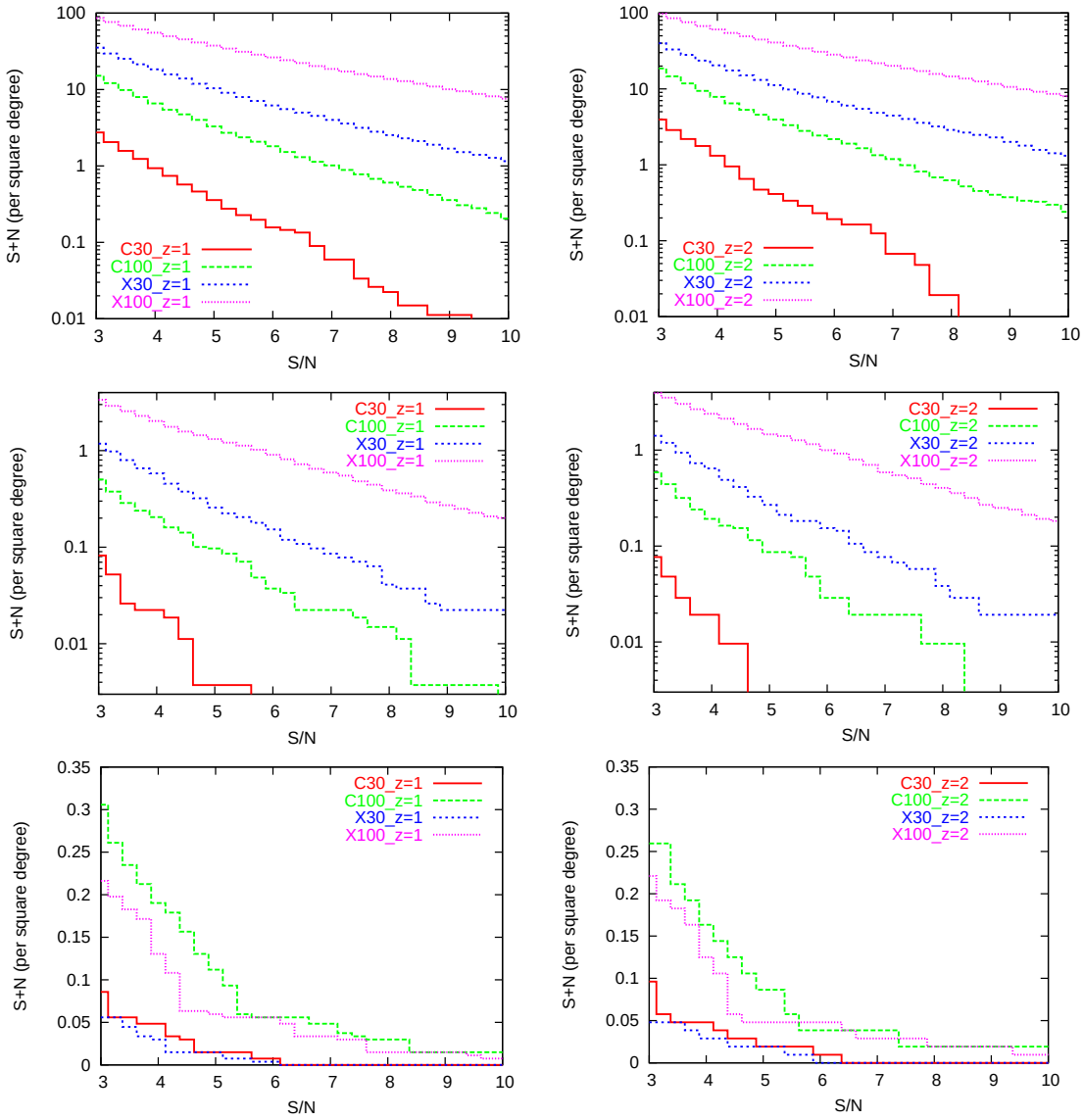

Figure 6.11: Total number of detections per square degree as a function of the S/N ratio obtained by filtering the Xray maps. Results are shown for three different bands analyzed: soft band (upper panels), hard band (middle panels) hardest band (bottom panels). Left and right panels refer to limiting redshifts of the light cones for $z = 1$ and $z = 2$, respectively. Different line styles refer to the two different instruments (XMM-*Newton* and Chandra) and to the two integration times (30 and 100 ks).In particular the red and green lines correspond to observations with Chandra of 30 and 100 ks, respectively; the blue and the violet line correspond to observations with XMM-*Newton* of 30 and 100 ks, respectively. The results are averaged over eleven realizations.

ferent realizations. The detections found simulating observations with XMM-*Newton* are at least a factor of five more numerous than for Chandra. Although XMM-*Newton* has a background level higher than Chandra, the better performance is due to the different effective area of the instrument. The number of detections decreases quite fast by the increasing of the minimal SN ratio. We find objects with high signal-to-noise ratios also in the high-energy band.

The fraction of spurious detections is presented in Fig. 6.12. We notice that the percentage of spurious detections below $S/N \approx 3$ is relatively small, always below 30% for all bands, and that it decreases to a constant value (about 5% independent on the integration time and the instrument).

In Fig. 6.13 we show the completeness of the detections which is only slightly dependent on the light-cone depth. For the soft and hard bands the detection catalogues obtained with XMM-*Newton* are always more complete that those obtained with Chandra. In the soft band the completeness as a function of the mass decreases much more slowly than for the higher frequencies bands. The completeness reaches 100% for masses $M \gtrsim 2 \times 10^{14}\ M_{\odot}/h$. It is $\sim 50\%$ at $M \sim 3 \times 10^{13}\ M_{\odot}/h$ for XMM-*Newton* with an exposure time of 100 ks (while for Chandra it is of the order of few percent). In the hard band with Chandra it is possible to detect only halos with mass $M > 2 \div 3 \times 10^{14}\ M_{\odot}/h$, the lower limit of detectability drops below by a factor four with XMM-*Newton*. A similar situation takes place for the soft band, but in this case, given the photons are less energetic, the lower limit to detect a halo is $M \approx 10^{13}\ M_{\odot}/h$. Indeed only halos with a mass larger than few times $10^{14}\ M_{\odot}/h$ are detected in the hardest band. In this band the completeness for Chandra is slightly larger than for XMM-*Newton* (for an integration time of 100 ks) because the background noise is almost three times smaller (see table 6.2).

In Fig. 6.14 we show the sensitivity for the X-ray detections. In the soft band we see that the sensitivity of Chandra is smaller than for XMM-*Newton*, consequently higher masses are needed to be detected. In the hard and in the hardest bands the sensitivity at low redshifts is essentially the same for both observatories, even if we notice that Chandra

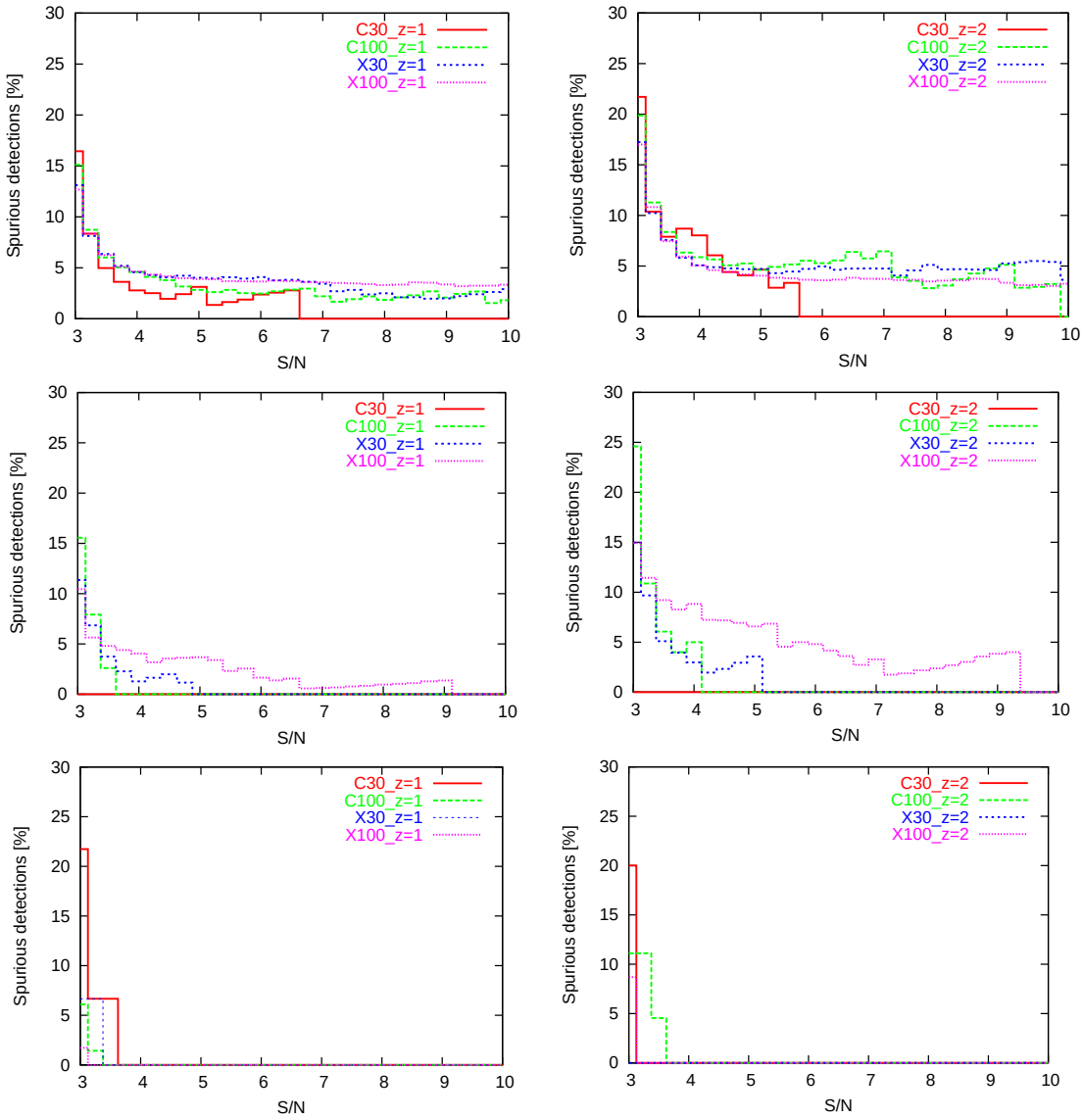

Figure 6.12: Fraction of spurious detection as a function of the S/N ratio for three different X-ray bands: soft band (upper panel), hard band (middle panel), hardest band (bottom panel). In the left and in the right panels we show results for limiting redshifts of the light-cones of $z = 1$ and $z = 2$, respectively. The values are obtained by averaging over eleven different realizations.

performs slightly better again due to the lower background noise. With Chandra, we can observe objects only up to $z \sim 0.4$ in the hard band, (for an integration time of 30 ks), while with XMM-*Newton* we can detect objects at $z \sim 0.9$. As expected only the most massive

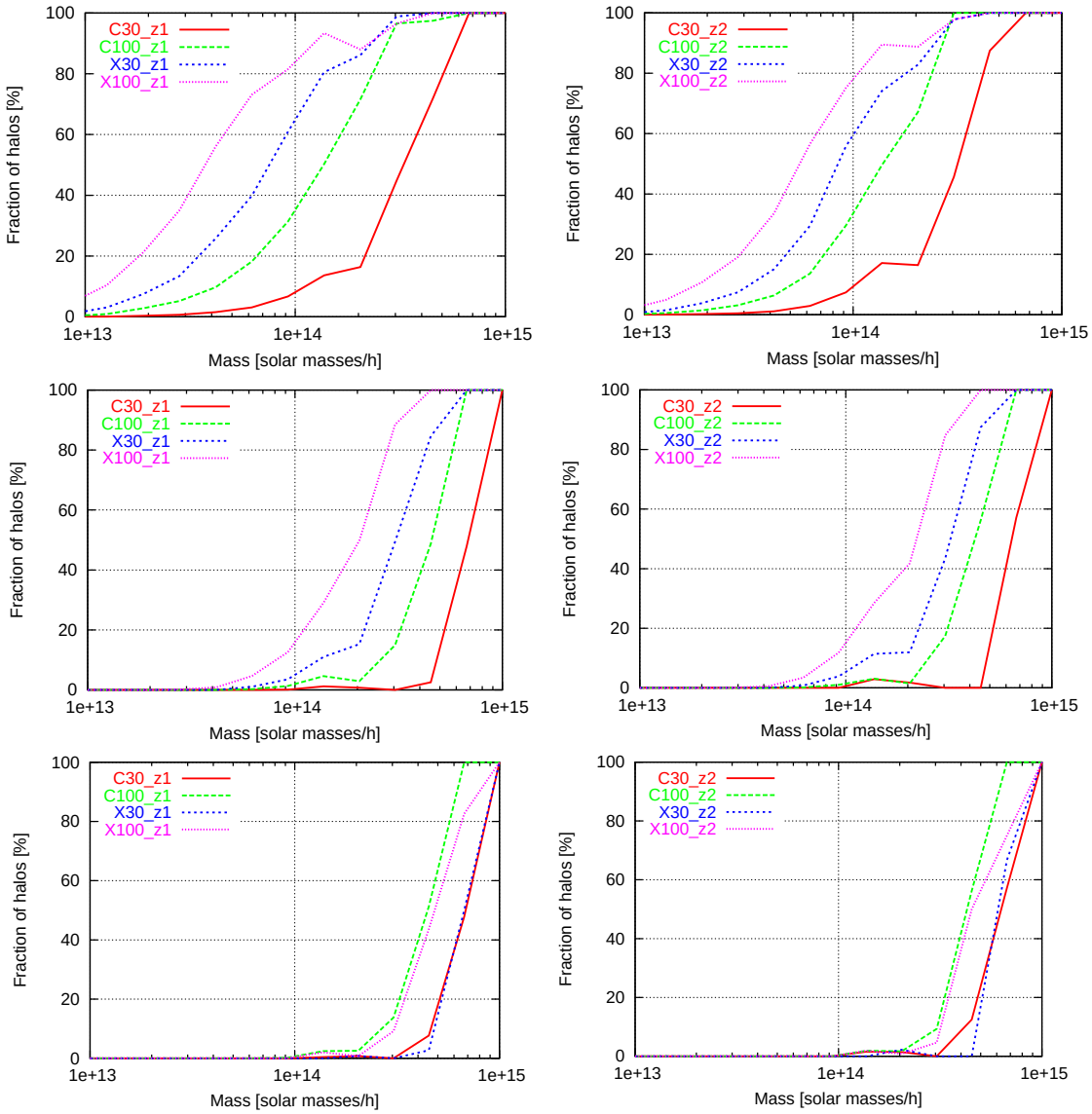

Figure 6.13: Fraction of detected halos as a function of the halo mass. The panel on the left and of the right show curves for limiting redshift of the light-cones up to $z = 1$ and $z = 2$, respectively. Different curve styles refer to different instruments and integration time. From bottom to top we show the soft band, the hard band and the hardest band. The curves are averaged over eleven maps.

clusters can be detected at high redshifts. In particular with Chandra, with an exposure time of 100 ks, the smallest masses detected are $10^{13} M_{\odot}/h$ at $z \sim 0.1$ and $10^{14} M_{\odot}/h$ at $z \sim 1$. With XMM-*Newton* halos of mass $M > 5 \times 10^{12} M_{\odot}/h$ and $M > 2 \times 10^{13} M_{\odot}/h$ can be detected at $z \sim 0.1$ and $z \sim 1$, respectively.

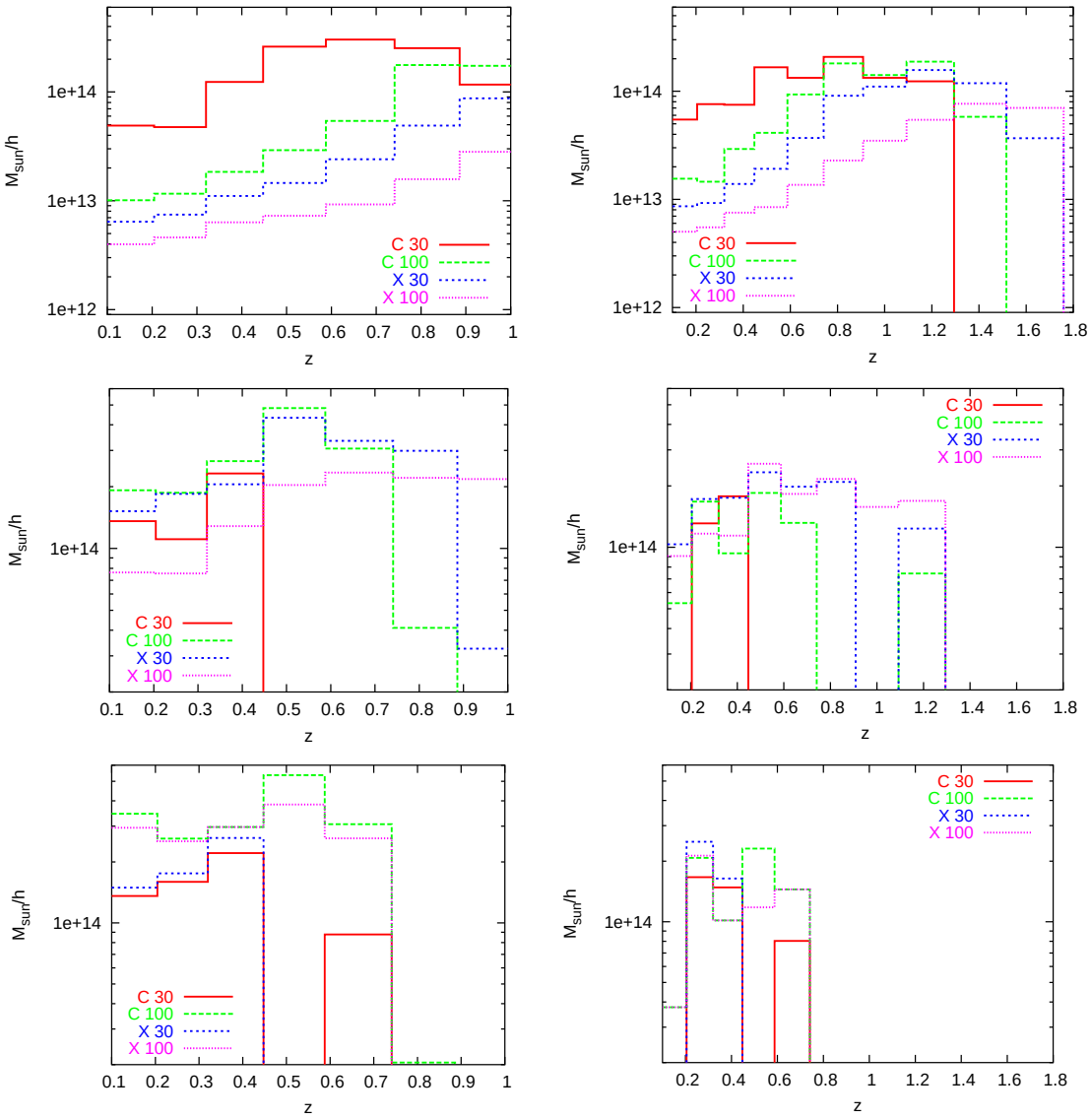

Figure 6.14: Sensitivity of the method for the X-ray detections. Results are shown for three different bands analyzed: soft band (upper panels), hard band (middle panels) hardest band (bottom panels). Left and right panels refer to limiting redshifts of the light cones for $z = 1$ and $z = 2$, respectively. Different line styles refer to the two different instruments (XMM-*Newton* and Chandra) and to the two integration times (30 and 100 ks).In particular the red and green lines correspond to observations with Chandra of 30 and 100 ks, respectively; the blue and the violet line correspond to observations with XMM-*Newton* of 30 and 100 ks, respectively. The results are averaged over eleven realizations.

6.4.4 Comparison with observations

We now compare our results with cluster detections in real observations. Finoguenov et al. (2006) analyzed the statistical properties of galaxy clusters in the COSMOS field, observed with XMM-*Newton*. In a field of view of 2.1 square degrees they identify 72 clusters in the soft band by using a wavelet scale-wise reconstruction of the image. The wavelet scale-wise reconstruction consists of a selection of the area with detectable flux on large angular scales and of the removal of the area where the flux can be explained by contamination of embedded point-like sources, using also optical identifications. More details can be found in Vikhlinin et al. (1998). Since our approach does not include optical identifications, we find more contamination in our sample than what expected with the wavelet scale-wise reconstruction. We found an amount of X-ray detections with $S/N > 3$ similar to the total number of photo-z galaxy concentrations (see Fig. 6 in Finoguenov et al. (2006)), taking into account the different integration time of our maps compared to the field of Finoguenov et al. (2006).

Vikhlinin et al. (2006) studied extensively 13 nearby clusters between $z \approx 0.01$ to $z \approx 0.23$ with Chandra. They derived their masses assuming hydrostatical equilibrium. The resulting masses enclosed in a radius where overdensities are 500 times the critical density of the universe at the redshift of the cluster range between $M \sim 7 \times 10^{13} M_{\odot}/h$ and $M \sim 10^{15} M_{\odot}/h$. The minimum mass we could detect with Chandra is $10^{13} M_{\odot}/h$ and $5 \times 10^{13} M_{\odot}/h$ for exposures of 100ks and 30 ks, respectively. We notice that our range is narrower of a factor approximately three compared to Vikhlinin et al. (2006).

6.5 Correlation between the X-ray and multi-band SZ detections

We now describe the spatial correlation between the detections in the X-ray and in the SZ maps. For the former, we consider the detections in the soft band, where the largest number of detections was found. For the latter, we use the results obtained by using the multi-band filter. A major difficulty is caused by the different angular scales of the detections in the maps. The X-ray detections have much smaller extension, since the X-

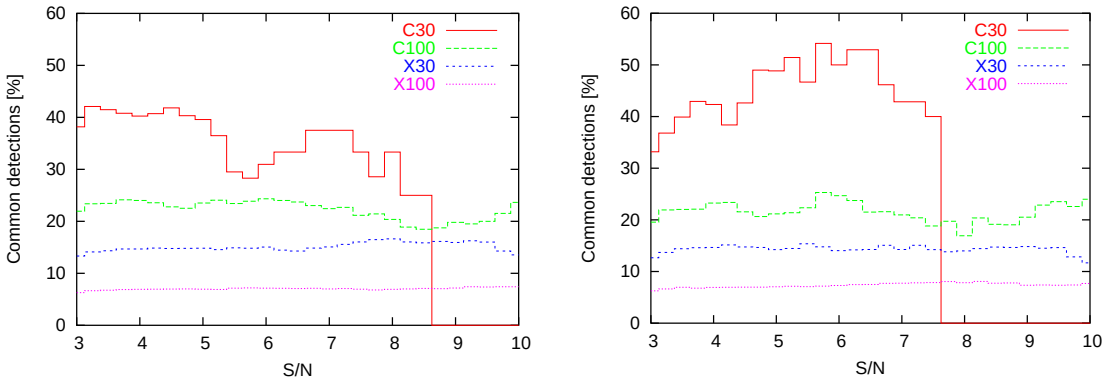

Figure 6.15: Fraction of common detections as function of the minimal S/N ratio. The red and the green line show the results for Chandra (30 and 100 ks of integration time, respectively), while the blue and the violet lines show results for XMM-*Newton* (30 and 100 ks of integration time, respectively).In the left and in the right panel we show results for limiting redshift of the light-cones of $z = 1$ and $z = 2$, respectively.

ray emission is more concentrated than the SZ effect. Consequently, several detections in the SZ maps overlap a large number of detections in the X-ray maps. For XMM-*Newton* with an integration time of 100 ks, we found that on average a SZ detection overlaps at least 10 X-ray detections. Therefore we correlated only the most significant X-ray detection of all the detections enclosed by the SZ detection. Moreover the number of detections in both the XMM-*Newton* and the Chandra observations strongly depends on the exposure time.

In Fig. 6.15 we show the fraction of common detections respect to the total number of X-ray detections as a function of the signal-to-noise ratio of the X-ray detections. Results are shown for limiting redshifts of the light-cones of $z = 1$ and $z = 2$ in the left and in the right panel, respectively and for XMM-*Newton* and Chandra with exposure times of 30 and 100 ks. The values are obtained averaging over eleven realizations.

Since Chandra has a low number of detections, we see, as expected, that the fraction of common detections is higher than for XMM-*Newton*. Moreover, as the number of X-ray detections increases with the exposure time, the corresponding fraction of common detections decreases. Surprisingly, the fraction of common detections is largely independent of the S/N ratio. We interpret this as due to the fact that the number of X-ray detections

is much higher than the one of SZ detections. When they are comparable (for example for Chandra with an exposure time of 30 ks), the scatter is much higher, of the order of 15%. For the same reason, we find very similar results for the two limiting redshifts for XMM-*Newton*, while for Chandra the scatter is enhanced.

In the top panels of Fig. 6.16 we show the correlation between a set of 11 X-ray and SZ maps directly obtained from the Λ-CDM simulation. On the x-axis we report the value of X-ray surface brightness and on the y-axis the Compton y-parameter. The contour levels enclose 50 to 99 per cent of the total number of pixels. We show results only in the soft band for XMM-*Newton* and for an exposure time of 100 ks. Since both the single-band and the multi-band filters returns an unbiased estimate of the y-parameter and of the X-ray surface brightness, we can repeat the same exercise by correlating the detection catalogues. This is shown in the middle panels of Fig. 6.16. The correspondence between the top and middle panels confirms that the filters do not introduce any bias in the estimates. The cut off at lower values of the Compton y-parameter and of the X-rays estimates reflects the combined sensitivity of the two observations. In the bottom panels of Fig. 6.16 we show the correlation between the X-ray and SZ maps using only the common detections in the two catalogues. Also in this case we note correspondence with the upper and middle panels.

In Fig. 6.17 we show the percentage of true detections in the X-ray observations that correspond to some detection in the SZ observations. We show the cumulative percentage as a function of the mass (top panels) and a differential distribution as a function of the redshift of the detected clusters (bottom panels). The left and the right panels refer to the two limiting redshifts of the light cones ($z = 1$ and $z = 2$, respectively). Different line styles correspond to different instruments in the X-ray observations and to different integration times. The curves are normalized to the total number of the clusters that are present in both the X-ray and the SZ catalogs.

The figures show two obvious results. First, the mass distribution of the common detections reflects the mass distribution of the clusters detected through the SZ effect (see

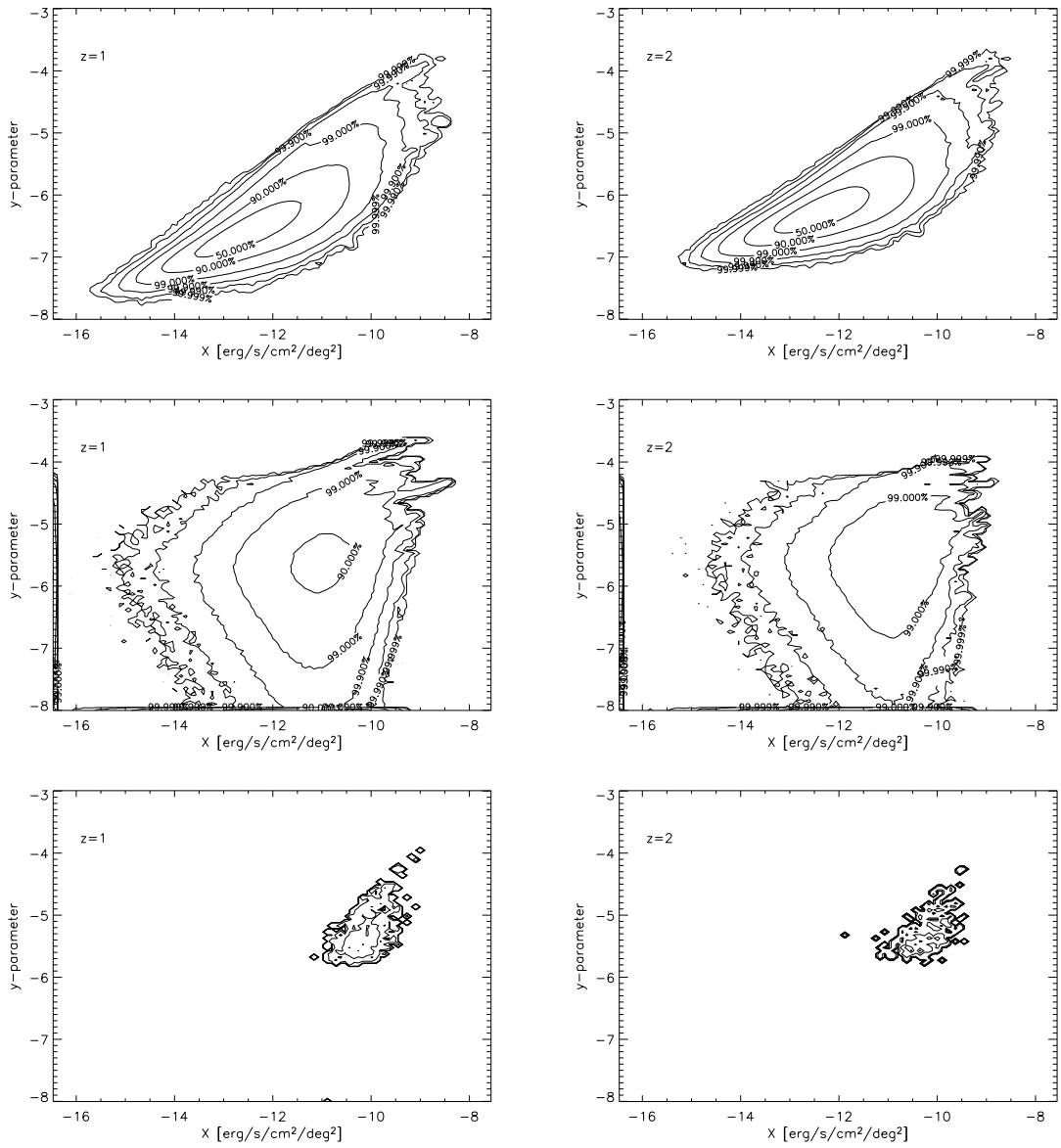

Figure 6.16: Distribution of the pixels values for X-ray (x-axis) and SZ (y-axis) maps. Upper panels show the distribution for the original maps, middle panels for the filtered maps, lower panels for the filtered map using only the common detections. In the left panel we show results for $z = 1$, in the right panel for $z = 2$.

Fig. 6.10). Indeed, many low mass halos that are detected in the X-ray maps, as shown in Fig. 6.14, are not detected in the SZ maps. Second, the redshift distribution of these clusters peaks at low redshifts. Indeed, high redshift clusters can not be detected through

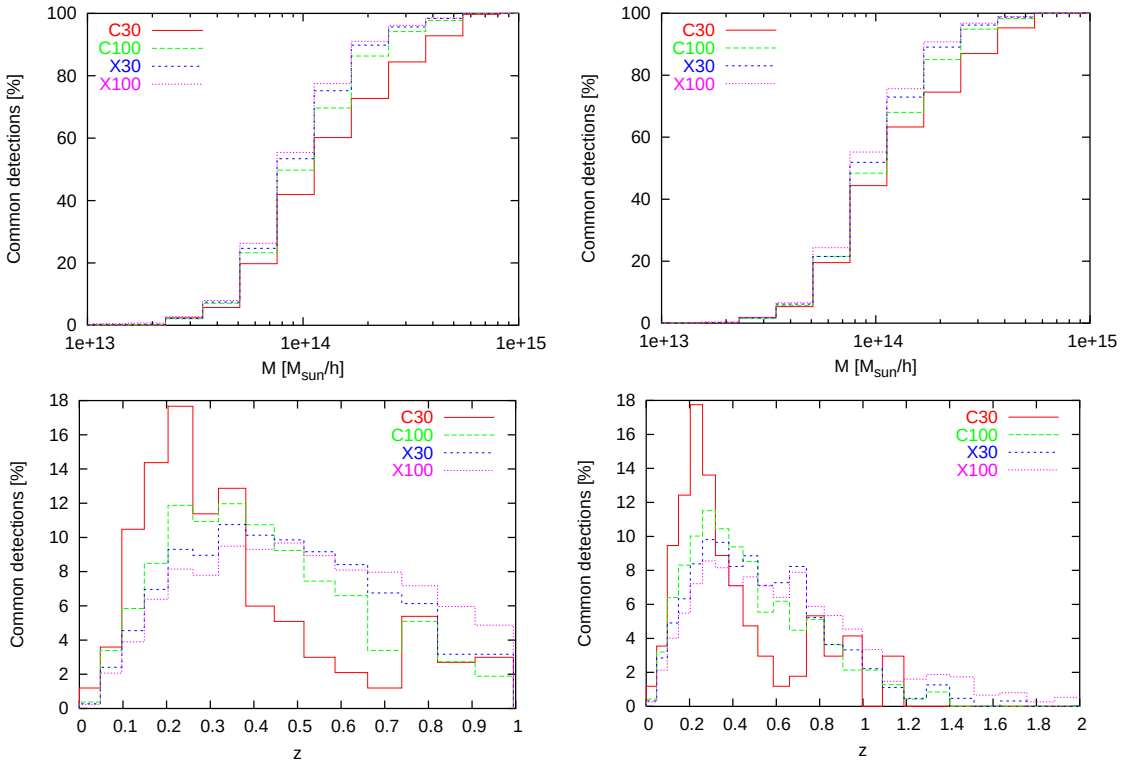

Figure 6.17: Top panels: cumulative mass distribution for halos detected in both the X-ray and the SZ maps. Results are shown for light cones up to $z = 1$ (left panels) and $z = 2$ (right panels). Bottom panels: redshift distribution for the same halos. The red and the green line show the results for Chandra (30 and 100 ks of integration time, respectively), while the blue and the violet lines show results for XMM-*Newton* (30 and 100 ks of integration time, respectively).

their X-ray emission.

6.6 Conclusions

We use a large N-body simulation for constructing light cones representing the distribution of matter in the universe up to a given redshift. This simulation is used to reproduce observations of the X-ray emission (XMM-*Newton* and Chandra) and of the SZ effect (ACT) produced by the matter contained in the light cones. Our simulations cover a total area of $\sim 264\ deg^2$ for limiting redshift $z = 1$ and $\sim 106\ deg^2$ for limiting redshift $z = 2$.

We use single-band and multi-band matched filters to detect galaxy clusters in the

simulated images. We detect halos as peaks in the filtered images and we compared the detections with the distribution of dark matter halos contained in the light cones. The halos are identified using standard friends-of-friends algorithms and SExtractor.

Regarding the detections in the SZ maps, we find that the use of the multi-band filter instead of the single-band filter strongly reduces the number of spurious detections and increases the fraction of halos in the light cones that are efficiently identified. In particular, 50% of the halos with masses $M \simeq 10^{14} M_{\odot}/h$ are found when using a multi-band filter against the 30% found with the single band filter. As expected, we do not notice a strong redshift dependence of the sensitivity of the method.

For the X-ray observations we found that the fraction of spurious detections is generally low, and it is largely constant (about 5%) over a large interval of signal-to-noise ratios. In general the X-ray catalogues are more complete than the SZ catalogues, even when multi-band filters are used. However, the redshift distribution of the halos detected through their X-ray emission is strongly peaked at low redshifts, since the X-ray luminosity is inversely proportional to the square of the luminosity distance. Thus, only massive halos can be detected at high redshift. This shows the complementarity of the two methods.

When studying the correlation of the SZ and X-ray detections, we found that the mass distribution of the common detections follows the mass distribution of the SZ detections, however the redshift distribution has a peak at low redshifts, as X-ray objects can not be detected at high redshifts.

Appendix A

Simulations

As said in chapter 5, in order to perform a realistic study of the formation and evolution of cosmic structures, N-body simulation codes are needed. In this section we briefly present the main characteristics of the different kinds of available codes.
Most N-body codes are based on the approximated description of the volume of the universe where the desired cosmic structures will form as a cubic box with N particles of mass M_i, position $\vec{x}_i$ and velocity $\vec{v}_i$. When hydrodynamics is not included, particles interact only via gravity, otherwise the baryonic particles will be subject to other physical effects.

The initial conditions are constructed in such a way that particles, initially distributed on a regular grid or following a glass distribution, are perturbed using the Zel'dovich approximation to reproduce the required initial power spectrum. The time and space evolution is obtained by solving, for each particle in the gravitational potential Φ, the usual equations of motion. The time evolution of this simulated volume of universe is discretised into finite time steps and for each one the force acting on the particles is computed and positions and velocities are updated according to the computed force.
Different N-body codes exist and they differ each other only for the method used to compute, at each time step, the gravitational force at the particle position.

A.1 The Particle-Particle (PP) method

In this case, the force per unit mass acting on the i-th particle is computed summing the contribution from all other particles

$$\vec{F}_i = \sum_{j \neq i}^{N} \frac{G m_j \vec{r}_{ij}}{(r_{ij} + \varepsilon_s)^3}, \tag{A.1}$$

where $\vec{r}_{ij}$ is the distance between the i-th and j-th particles and ε_s represents the so-called softening length, necessary for avoiding small-scale divergences in the force computation. In other words, the particles acquire a physical size.

The gravitational interaction is Newtonian only for $r_{ij} > \varepsilon_s$, while for smaller distances different expressions must be used. Usually the softening length is given in terms of the *Plummer softening length*, in practice the particle is replaced by a sphere following the Plummer density profile (Plummer, 1911):

$$\rho_{Plummer}(r) = \frac{3m}{4\pi\varepsilon_s^3 (1 + r^2/\varepsilon_s^2)^{5/2}}. \tag{A.2}$$

The PP method achieves a very high accuracy, but it requires an high computational time, being of the order of O(N^2), so it is used only for small particle numbers ($N \sim 10^{4 \div 5}$).

A.2 The Particle-Mesh (PM) method

In the PM method, density, gravitational potential and forces are computed on a regular *mesh* (grid of points). The actual values of these quantities at the particle positions are obtained adopting interpolation techniques that will be described in Appendix B. In this way the computation is faster, but the maximum resolution achieved correspond to the mesh size. Given the density at each mesh point, the potential can be easily computed via fast Fourier techniques, the Poisson equation is then solved in the Fourier space and the force is obtained by exploiting the properties of derivative in the Fourier domain. An inverse Fourier transform gives the force and the potential at each grid point in the real space and adopting the same interpolating schemes used to compute the density,

their values at the particle positions are derived. Due to the fast Fourier transform (FFT) technique, the required computational time is of the order of O($N \log N$), so it is suitable for systems of $\sim 10^{8 \div 9}$ particles.

A.3 The Particle-Particle-Particle-Mesh method P^{3}M

The P^{3}M method represents a combination of the two previously described methods. The total force experienced by the particle is given by two contributes: $\vec{F} = \vec{F}^{\rm sr} + \vec{F}^{\rm lr}$. The term $\vec{F}^{\rm sr}$ is the *short-range* contribution and it is computed using the PP method, while the term $\vec{F}^{\rm lr}$ represents the *long-range* contribution that is obtained with the PM method. A particle is included in the short-range regime if its distance from the particle the force is computed on is smaller than a given value. To improve the accuracy of the code, in the regions where the density is high, adaptive grids are often used.

A.4 The Tree code

Tree codes belong to the family of hierarchical codes, based on the multipole expansion and were introduced by Barnes & Hut (1986).

A group of distant particles exerts almost the same force as a particle having the total mass of the group and located at the center-of-mass of the group itself. This is equivalent to the use of monopole term only in the expansion. Better accuracy is achieved using higher multipoles. The region containing the particles is divided into cubes and each one is subdivided into eight subcubes (hence the name oct-tree). The division continues until the subcubes contain only one or zero particle and each subcube (leaf) can be reached walking through the tree starting from the root node. The force is computed by walking the tree and summing the contributions of the individual nodes.

If a node has size l and if r is the distance between its center-of-mass and the point where the force needs to be computed, then the multipole expansion is used if $l/r < \theta$, where θ is the opening angle and sets the accuracy of the calculation. When this condition is fulfilled, the walk along the branch of the node is stopped, otherwise it is opened and the

walk continues through the subnodes. The contributions from the nearest particles are computed with the PP method.
In this case the computation time scales as $N \log N$.

A.5 Hydrodynamical simulations

The codes described before are only gravity solvers and they can be applied properly when the dark matter component only is considered. But in the universe there are also baryons that undergo more complex physical phenomena, in particular the physics related to gas and intergalactic medium, like heating, cooling, energy feedback, etc. These phenomena are difficult to be implemented in numerical codes, due to their complexity and the crude knowledge of the details of the physics involved.
To appropriately describe the interparticle interactions, many methods have been suggested. Among them, a very powerful technique traces back to the work by Lucy (1977) and Gingold & Monaghan (1977) and it is called *Smoothed Particle Hydrodynamics* (SPH).
The fluid is discretised into particles and the field quantities are computed at position $\vec{r}$ by mean of a kernel function $W(\vec{r}-\vec{r}';h)$ where h represents the smoothing length, which is related to the number of particles used for the computation, usually between 30 and 50.
One of the most widely used kernel is the one proposed by Monaghan & Lattanzio (1985) (also used in the GADGET Tree-SPH code):

$$W(r,h) = \frac{8}{\pi} \begin{cases} 1-6u^2+6u^3 & 0 \leq u < 0.5 \\ 2(1-u)^3 & 0.5 \leq u \leq 1 \\ 0 & u > 1 \end{cases} \tag{A.3}$$

Higher order smoothing functions permit an higher accuracy.
More details on the SPH method can be found in the review by Monaghan (1992).

Appendix B

Interpolation schemes

Whenever a quantity defined on a mesh has to be evaluated on a point located between two grid points, an interpolation is necessary.
In literature, many different smoothing schemes have been described and differ mainly on the number of points used for the interpolation: obviously the higher is the number of points, the higher is the accuracy that can be reached. Nevertheless, usually no more than three points (per dimension) are used as the accuracy gained is too modest compared to the required increase of computational time.
If $w(x_i)_i$ represents the smoothing function in the i-th dimension, the total interpolating function can be written as simple product of all the functions, $W(\vec{x}) = \prod_{i=1}^{N} w(x_i)_i$; d represents the number of dimensions of the system.

The most widely adopted smoothing functions are, in increasing order of accuracy (Hockney & Eastwood, 1988):

- *Nearest Grid Point* (NGP), where the particle mass is assigned to one grid point only. The smoothing function is therefore

$$w = \begin{cases} 1 & \text{for } |\delta x| < \Delta/2 \\ 0 & \text{for } |\delta x| > \Delta/2. \end{cases} \tag{B.1}$$

- *Cloud-in-Cell* (CIC), where the particle mass is assigned to the 2^d nearest points. The smoothing function is

$$w = \begin{cases} 1 - |x|/\Delta & \text{for } |\delta x| \leq \Delta \\ 0 & \text{for } |\delta x| > \Delta. \end{cases} \tag{B.2}$$

Scheme	Order	Number of points	Scheme Shape	Force
NGP	0	1^d	δ	Stepwise
CIC	1	2^d	Π	Continuous piecewise linear
TSC	2	3^d	Λ	Continuous value and first derivative
PQS	3	4^d	$\Lambda * \Pi$	Continuous value, first and second derivatives

Table B.1: Table summarizing the characteristics of the different interpolation schemes. The first column refers to the name of the interpolating scheme; the second column to the order of the scheme; the third column to the number of points used for the interpolation; the fourth to the shape of the scheme and the fifth to the characteristics of the resulting computed force. Here δ is the delta function, Π the step function and Λ the triangular function and the asterisk represents the convolution of the functions. Table adapted from Hockney & Eastwood (1988).

- *Triangular Shape Cloud* (TSC), where the particle mass is assigned to the 3^d nearest points. The smoothing function is

$$w = \begin{cases} 3/4 - (\delta x/\Delta)^2 & \text{for } |\delta x| \leq \Delta/2 \\ (3/2 - |\delta x|/\Delta)^2/2 & \text{for } \Delta/2 \leq |\delta x| \leq 3\Delta/2 \\ 0 & \text{for } |\delta x| \leq 3\Delta/2. \end{cases} \tag{B.3}$$

where the smoothing functions are normalized such that the mass of the system is conserved. The described interpolation schemes can be extended to an arbitrary number of points, increasing thus the precision and the number of derivatives of the force that result continuous at the end. An example is the interpolation scheme PQS, that uses the nearest 4^d points.

In table B.1 we summarize the characteristics of the different interpolation schemes.

As clear from table B.1, a new scheme can be obtained iterating the smaller-order schemes. AS $\Lambda = \Pi * \Pi$, an interpolation scheme with order $n > 3$ can be obtained convolving the Π function n times.

A more suitable interpolation scheme for gas particles in simulations, is an SPH scheme, that takes into account the smoothing length of the particles. The number of points involved varies according to the smoothing length and the size of the grid; the smaller is the grid, the higher is the accuracy. With this scheme, the function and all the derivatives are continuous. The fraction of the particle associated to each grid point is given by the values of the smoothing kernel.

Conclusions

In this thesis we have discussed applications of filtering techniques to the study of detection of halos from numerical simulations.
Many weak-lensing observations showed that many, approximately half of the peaks in the shear field can not be associated to any optical or X-ray counterpart. With the improvements in the observational techniques that lead to precise cosmological studies, it is of fundamental importance to know what these dark peaks correspond to, either dark halos or LSS, because of the cosmological consequences one intends to infer.
Multi-band observations are always more common, because they allow to combine different pieces of information from the same object. The advantage of this is that on one side it is thus possible to have a better understanding of the objects under investigation, on the other side multiband observations are required to remove the strong degeneracy in the parameter space.

Exploiting that the masses and the positions of the clusters from the simulation are known precisely, it is possible to clearly identify whether a detection corresponds to a halo or if it is caused by some source of noise present in the simulated maps.
With hydrodynamical cosmological simulations, it is possible to perform realistic studies taking into account also very complex physical phenomena that baryonic matter experiences.
They are therefore required to have an accurate study of cluster emission that does not rely on too simplified assumptions.

The main goal of this thesis was to improve the study of filtering techniques employed to detect galaxy clusters.

We obtained the following results:

- We created realistic shear and convergence maps to simulate weak-lensing observations and we used them to study the performance of three different linear filters often used to detect halos from shear field in weak-lensing surveys. The filter tested are the aperture mass, the optimised aperture mass and the optimal filter, designed to distinguish halo signals from spurious signals caused by the large-scale structure. We showed that the optimised filter proposed by Maturi et al. (2005) successfully reduces the contribution of the large-scale structures, therefore it performs better than the aperture mass. In particular its results are largely insensitive to changes in the angular filter scale and the number of spurious detections is reduced. We also showed that, compared to the other filters analyzed, the halos detected have a lower mass limit.

- Two factors contribute to yield an appreciable lensing signal: the mass of a cluster and its relative position between the observer and the sources. We found that the minimum detectable mass is $\sim 10^{13}\ M_{\odot}/h$ where the lensing effective distance reaches the maximum (approximately half way between the observer and the sources) and that it increases approaching the observer (few times $10^{13} M_{\odot}/h$) or the source redshift ($\sim 10^{14}\ M_{\odot}/h$).

- A very important aspect of a survey is the degree of completeness it can reach. Detecting halos from raytracing simulations, we showed that the curve describing the completeness as a function of the mass is very steep and strongly depends on the mass of the object. We found that generally catalogues are complete only for masses above $\sim 4.5 \times 10^{14} M_{\odot}/h$ if sources are around $z_s = 1$ and for masses above $\sim 3 \times 10^{14} M_{\odot}/h$ for more distant sources at $z_s = 2$. For objects only twice smaller, the completeness has already dropped to 50%.

- We created SZ and X-ray maps from a large hydrodynamical simulation to detect halos in it with a matched filter and to study the properties of the common detections

between the SZ and X-ray catalogues. For the SZ we used a single-band and a multi-band matched filter, while for the X-ray analysis we used only the single-band filter.

- We found that using multi-band instead of single-band filters the number of spurious detections reduces strongly and more halos are identified. We found that 50% of the halos with masses $M \simeq 10^{14} M_{\odot}/h$ are found when using a multi-band filter.

- For the X-ray detections we found that the fraction of spurious detections is low and largely constant over a large interval of signal-to-noise ratios. X-ray catalogues are more complete than the multi-band SZ catalogues. We also found that the redshift distribution is peaked at low redshifts, therefore only massive halos can be detected at high redshift.

- Halos in common bwtween the SZ catalogues and the X-ray catalogues show the same mass distribution of the SZ detections, but the redshift distribution of the X-ray detections. This is due to the fact that halos detected with the SZ filter have higher masses than for halos detected with the X-ray filter and that X-ray objects can not be detected at high redshifts.

Acknowledgments

Finally I arrived to the end of the Thesis! It's very early in the morning and it is time to go to bed (I'm becoming like a vampire).
First of all I want to thank my parents who supported me during the years of university in Bologna and then also here in Heidelberg. Probably without their support I would never arrive to this point.

I want to thank my supervisor, Matthias, who patiently helped me during these three long years (ok a little bit more than three) with many useful suggestions and discussions and addressed my work always in the right direction. Thanks to him I learned many things about cosmology and lensing. I also would like to thank Matthias because he allowed me to discover my intrinsic incompatibility with every computer surrounding me.
Thanks also to Lauro, who had the nice idea to send me to Heidelberg, to get rid of me and to use me as a starting point for a new phase of Italian colonization in Germany.
Thanks also to Prof. Dr. Eva Grebel and Prof. Dr. Ralf Klessen to accept to be in my defense commission and in particular to Prof. Dr. Joachim Wambsganß who was so brave to accept to be my second referee.

Now to my colleagues.
First of all to Emanuel, that with endless patience avoided that cosmo3 or my laptop died completely for the inappropriate use I was doing or because of my powers. I also want to thank him for the long discussions about German language trying to convince me that despite everything, there is a logic, even if I am not so convinced and for his amazing capability in drinking beer so fast.
Thanks to cosmo3 and my laptop (back to life already twice) for enduring all this time

and allowing me to reach the end.
Many and sincere thanks to Matteo and Massimo who helped me during all my PhD and in particular in these last weeks to manage to finish in time all the work. I owe you some beers and dinners! Massimo good luck for the baby soon coming!
Many thanks to my office mates, Farid, Julian (the guy with very curly hair) and Ewald (the Austrian or Waldi according to me and The Machine according to himself) who incredibly enough survived to me and to my weird Italian way of speaking and behaving. I also want to thank Ewald for trying very hard to teach me swimming, even if I was not such a good student and not let me drown during the lessons.
Thanks to Gregor for useful discussions and for recovering my laptop when Emanuel was not around, to the two Peter (der Blonde and der Schwarze) for discussions over several stuffs and for the time spent playing table tennis. I want to thank Peter also because I could find very soon a new flat. Also thanks to Martin, for being so direct when he wants to express something and of course for the hard duels playing table tennis. He was a very good teacher regarding beer world.
I would like to thank Jean-Claude for the moral support during the work on the early dark energy simulation, for being available for a match to table tennis and for very useful discussions on bikes and training.
Thanks also to Irina for joining me during my bike trips or coming with me to the cinema to see some horror movie and to Ana who unfortunately left already the group, in particular for her funny way of laughing that let someone think she was a dog (I must add a Portuguese dog).
Thanks of course to the rest of the Italian community in the group: Cosimo for being always available in the institute, whatever day of the week and for accepting (nicely) to loose against my luck, to Claudia, for being always so nice, for cooking very delicious meal and for discussions on movies and to Marcello, the Sicilian guy, for the nice time spent here.
Thanks also to Gunter, for being now an institution of ITA, Uli for the power of beer on

increasing his chattiness and Svitlana for being so nice and sharing very often with me her food.
Last but not least, Christian, the mean guy with the beard, who despite the nickname, was so nice to translate the abstract into German as my version was totally incomprehensible. I also want to thank him for playing table tennis and pool, for many interesting discussions on David Lynch's movies and, I know that he will complain for sure, for being the source of so many nice and good-looking girls!

Now it's the turn of people outside university.
First of all I want to thank Antonio, for helping me with computers and discussing about physics and Monica, my preferred bleached blond, for the weird talks with aMSN and Laura for translating the necessary (?) documents for the defense.
Thanks also to Mauro, for helping me a lot while working on SZ and X-ray maps.
Thanks to Benedetta for the nice evening together and in particular for the cakes she used to bake to feed the group.
Many thanks to Fabio and Patrick who helped me moving and for being always available for at least one beer. In particular I would like to thank Patrick for the several German translations, for joining me in the summer during several bike trips and for sure for bringing me to the physician and not to the exorcist (Ich habe das Böse in meinem Knie).
Thanks also to Matthias, my former flat mate, for the nice period spent and for taking care of my bike so I could always come back home, but now he has to take care of his son and to my present flat mates, in particular Andi and Stefi for supporting me in this very stressing weeks.

Many special thanks to all my nice and beautiful German tandem partners, in particular Inga and Lisa, for the really nice time spent together especially when we were meeting for going out and for trying, I don't know how successfully, to teach me German. Now I should have more time to meet you again.
Thanks also to Franco and Mantizza, for guesting me several evenings in the restaurant and for all the tasting food and wine.

Finally, a very special thanks to Sanja for the really nice evenings spent together and for being patient when I have to say something in German. Thanks also for not disappearing when, without knowing it, I was saying very weird things and for joining to go to the cinema.

Now it's really time to conclude with a citation by Trapattoni that summarizes my German knowledge:

ICH HABE FERTIG!

Bibliography

Bacon, D. J., Goldberg, D. M., Rowe, B. T. P., & Taylor, A. N. 2006, MNRAS, 365, 414

Bardeen, J. M., Bond, J. R., Kaiser, N., & Szalay, A. S. 1986, ApJ, 304, 15

Barnes, J. & Hut, P. 1986, Nature, 324, 446

Bartelmann, M. 1996, A&A, 313, 697

Bartelmann, M., Doran, M., & Wetterich, C. 2006, A&A, 454, 27

Bartelmann, M. & Schneider, P. 1991, A&A, 248, 349

Bartelmann, M. & Schneider, P. 2001, PhysRep, 340, 291

Bernardeau, F., van Waerbeke, L., & Mellier, Y. 1997, A&A, 322, 1

Bertin, E. & Arnouts, S. 1996, A&AS, 117, 393

Birkinshaw, M. 1999, PhR, 310, 97

Bond, J. R., Cole, S., Efstathiou, G., & Kaiser, N. 1991, ApJ, 379, 440

Bond, J. R. & Myers, S. T. 1996, ApJS, 103, 1

Borgani, S., Murante, G., Springel, V., et al. 2004, MNRAS, 348, 1078

Borgani, S., Rosati, P., Tozzi, P., & Norman, C. 1999, ApJ, 517, 40

Bullock, J. S., Kolatt, T. S., Sigad, Y., et al. 2001, MNRAS, 321, 559

Caldwell, R. R. 2002, Physics Letters B, 545, 23

Caldwell, R. R., Dave, R., & Steinhardt, P. J. 1998, Physical Review Letters, 80, 1582

Carlstrom, J. E., Holder, G. P., & Reese, E. D. 2002, ARA&A, 40, 643

Carroll, S. M., Press, W. H., & Turner, E. L. 1992, ARA&A, 30, 499

Cavaliere, A. & Fusco-Femiano, R. 1976, A&A, 49, 137

Cavaliere, A. & Fusco-Femiano, R. 1978, A&A, 70, 677

Clowe, D., De Lucia, G., & King, L. 2004, MNRAS, 350, 1038

da Silva, A. C., Barbosa, D., Liddle, A. R., & Thomas, P. A. 2000, MNRAS, 317, 37

Diaferio, A., Borgani, S., Moscardini, L., et al. 2005, MNRAS, 356, 1477

Diego, J. M., Vielva, P., Martínez-González, E., Silk, J., & Sanz, J. L. 2002, MNRAS, 336, 1351

Doran, M. 2005, Journal of Cosmology and Astro-Particle Physics, 10, 11

Doran, M., Karwan, K., & Wetterich, C. 2005, Journal of Cosmology and Astro-Particle Physics, 11, 7

Doran, M. & Robbers, G. 2006, Journal of Cosmology and Astro-Particle Physics, 6, 26

Eisenstein, D. J. 1997, ArXiv Astrophysics e-prints

Eisenstein, D. J. & Loeb, A. 1995, ApJ, 439, 520

Eisenstein, D. J., Zehavi, I., Hogg, D. W., et al. 2005, ApJ, 633, 560

Eke, V. R., Cole, S., & Frenk, C. S. 1996a, MNRAS, 282, 263

Eke, V. R., Cole, S., Frenk, C. S., & Navarro, J. F. 1996b, MNRAS, 281, 703

Eke, V. R., Navarro, J. F., & Frenk, C. S. 1998, ApJ, 503, 569

Eke, V. R., Navarro, J. F., & Steinmetz, M. 2001, ApJ, 554, 114

Erben, T., Miralles, J. M., Clowe, D., et al. 2003, A&A, 410, 45

Erben, T., van Waerbeke, L., Mellier, Y., et al. 2000, A&A, 355, 23

Etherington, I. M. H. 1933, Philos. Mag., 15, 761

Ettori, S., Borgani, S., Moscardini, L., et al. 2004, MNRAS, 354, 111

Fang, W. & Haiman, Z. 2007, PhRvD, 75, 043010

Faraoni, V. 2005, Classical and Quantum Gravity, 22, 3235

Fassnacht, C. D., Xanthopoulos, E., Koopmans, L. V. E., & Rusin, D. 2002, ApJ, 581, 823

Fedeli, C. & Bartelmann, M. 2007, A&A, 461, 49

Ferreira, P. G. & Joyce, M. 1998, PhRvD, 58, 023503

Finoguenov, A., Guzzo, L., Hasinger, G., et al. 2006, ArXiv Astrophysics e-prints

Freedman, W. L., Madore, B. F., Gibson, B. K., et al. 2001, ApJ, 553, 47

Friedmann, A. 1922, Z. Phys., 10, 377

Friedmann, A. 1924, Z. Phys., 21, 326

Gingold, R. A. & Monaghan, J. J. 1977, MNRAS, 181, 375

Goldberg, D. M. & Bacon, D. J. 2005, ApJ, 619, 741

Gunn, J. E. 1967, ApJ, 150, 737

Haardt, F. & Madau, P. 1996, ApJ, 461, 20

Haehnelt, M. G. & Tegmark, M. 1996, MNRAS, 279, 545

Hamana, T. & Mellier, Y. 2001, MNRAS, 327, 169

Hamana, T., Takada, M., & Yoshida, N. 2004, MNRAS, 350, 893

Hamilton, A. J. S., Kumar, P., Lu, E., & Matthews, A. 1991, ApJL, 374, L1

Harrison, E. R. 1970, PhRvD, 1, 2726

Hawkins, E., Maddox, S., Cole, S., et al. 2003, MNRAS, 346, 78

Hennawi, J. F. & Spergel, D. N. 2005, ApJ, 624, 59

Herranz, D., Sanz, J. L., Barreiro, R. B., & Martínez-González, E. 2002a, ApJ, 580, 610

Herranz, D., Sanz, J. L., Hobson, M. P., et al. 2002b, MNRAS, 336, 1057

Hetterscheidt, M., Erben, T., Schneider, P., et al. 2005, A&A, 442, 43

Hobson, M. P. & McLachlan, C. 2003, MNRAS, 338, 765

Hockney, R. W. & Eastwood, J. W. 1988, Computer simulation using particles (Bristol: Hilger, 1988)

Hoekstra, H. 2001, A&A, 370, 743

Hoekstra, H., Mellier, Y., van Waerbeke, L., et al. 2006, ApJ, 647, 116

Horellou, C. & Berge, J. 2005, MNRAS, 360, 1393

Hütsi, G. 2006, A&A, 446, 43

Jain, B., Mo, H. J., & White, S. D. M. 1995, MNRAS, 276, L25

Jain, B. & Seljak, U. 1997, ApJ, 484, 560

Jain, B. & Van Waerbeke, L. 2000, ApJL, 530, L1

Jenkins, A., Frenk, C. S., White, S. D. M., et al. 2001, MNRAS, 321, 372

Jing, Y. P. & Suto, Y. 2000, ApJL, 529, L69

Johri, V. B. 2004, PhRvD, 70, 041303

Kaiser, N. 1992, ApJ, 388, 272

Kaiser, N. 1995, ApJL, 439, L1

Kaiser, N. & Squires, G. 1993, ApJ, 404, 441

Kaiser, N., Squires, G., & Broadhurst, T. 1995, ApJ, 449, 460

Kazantzidis, S., Kravtsov, A. V., Zentner, A. R., et al. 2004, ApJL, 611, L73

King, I. 1962, AJ, 67, 471

King, I. R. 1966, AJ, 71, 64

Kitayama, T. & Suto, Y. 1997, ApJ, 490, 557

Knox, L. 1995, PhRvD, 52, 4307

Kujat, J., Scherrer, R. J., & Sen, A. A. 2006, PhRvD, 74, 083501

Lacey, C. & Cole, S. 1993, MNRAS, 262, 627

Lacey, C. & Cole, S. 1994, MNRAS, 271, 676

Lahav, O., Lilje, P. B., Primack, J. R., & Rees, M. J. 1991, MNRAS, 251, 128

Li, L.-X. & Ostriker, J. P. 2002, ApJ, 566, 652

Limber, D. N. 1953, ApJ, 117, 134

López-Caniego, M., Herranz, D., González-Nuevo, J., et al. 2006, MNRAS, 370, 2047

Lucchin, F. & Matarrese, S. 1985, PhRvD, 32, 1316

Lucy, L. B. 1977, AJ, 82, 1013

Maor, I. 2006, ArXiv Astrophysics e-prints

Maor, I. & Lahav, O. 2005, Journal of Cosmology and Astro-Particle Physics, 7, 3

Mather, J. C., Fixsen, D. J., Shafer, R. A., Mosier, C., & Wilkinson, D. T. 1999, ApJ, 512, 511

Maturi, M., Meneghetti, M., Bartelmann, M., Dolag, K., & Moscardini, L. 2005, A&A, 442, 851

Maturi, M., Schirmer, M., Meneghetti, M., Bartelmann, M., & Moscardini, L. 2007, A&A, 462, 473

Melin, J.-B., Bartlett, J. G., & Delabrouille, J. 2006, A&A, 459, 341

Meneghetti, M., Bartelmann, M., & Moscardini, L. 2003, MNRAS, 340, 105

Meneghetti, M., Bolzonella, M., Bartelmann, M., Moscardini, L., & Tormen, G. 2000, MNRAS, 314, 338

Meszaros, P. 1974, A&A, 37, 225

Mewe, R., Kaastra, J. S., & Liedahl, D. A. 1995, Legacy, 6, 16

Minchin, R., Davies, J., Disney, M., et al. 2005, ApJL, 622, L21

Miyazaki, S., Hamana, T., Shimasaku, K., et al. 2002, ApJL, 580, L97

Monaghan, J. J. 1992, ARA&A, 30, 543

Monaghan, J. J. & Lattanzio, J. C. 1985, A&A, 149, 135

Moore, B., Governato, F., Quinn, T., Stadel, J., & Lake, G. 1998, ApJL, 499, L5+

Mota, D. F. & van de Bruck, C. 2004, A&A, 421, 71

Murante, G., Arnaboldi, M., Gerhard, O., et al. 2004, ApJL, 607, L83

Narayan, R. & Bartelmann, M. 1996, ArXiv Astrophysics e-prints

Navarro, J. F., Frenk, C. S., & White, S. D. M. 1997, ApJ, 490, 493

Pace, F., Maturi, M., Meneghetti, M., et al. 2007, A&A, 471, 731

Padmanabhan, N., Seljak, U., & Pen, U. L. 2003, New Astronomy, 8, 581

Peacock, J. A. & Dodds, S. J. 1996, MNRAS, 280, L19

Peacock, J. A. & Heavens, A. F. 1985, MNRAS, 217, 805

Peebles, P. J. & Ratra, B. 2003, Reviews of Modern Physics, 75, 559

Peebles, P. J. E. 1980, The large-scale structure of the universe (Research supported by the National Science Foundation. Princeton, N.J., Princeton University Press, 1980. 435 p.)

Peebles, P. J. E. & Ratra, B. 1988, ApJL, 325, L17

Peebles, P. J. E. & Yu, J. T. 1970, ApJ, 162, 815

Perlmutter, S., Aldering, G., Goldhaber, G., et al. 1999, ApJ, 517, 565

Pierpaoli, E., Anthoine, S., Huffenberger, K., & Daubechies, I. 2005, MNRAS, 359, 261

Plummer, H. C. 1911, MNRAS, 71, 460

Premadi, P., Martel, H., & Matzner, R. 1998, ApJ, 493, 10

Press, W. H. & Schechter, P. 1974, ApJ, 187, 425

Puchwein, E., Bartelmann, M., Dolag, K., & Meneghetti, M. 2005, A&A, 442, 405

Rasia, E., Mazzotta, P., Borgani, S., et al. 2005, ApJL, 618, L1

Ratra, B. & Peebles, P. J. E. 1988, PhRvD, 37, 3406

Reblinsky, K. & Bartelmann, M. 1999, A&A, 345, 1

Rephaeli, Y. 1995, ARA&A, 33, 541

Rephaeli, Y., Sadeh, S., & Shimon, M. 2005, in Background Microwave Radiation and Intracluster Cosmology, ed. F. Melchiorri & Y. Rephaeli, 57–+

Riess, A. G., Filippenko, A. V., Challis, P., et al. 1998, AJ, 116, 1009

Roncarelli, M., Moscardini, L., Borgani, S., & Dolag, K. 2007, MNRAS, 378, 1259

Roncarelli, M., Moscardini, L., Tozzi, P., et al. 2006, MNRAS, 368, 74

Sahni, V. 2005, in LNP Vol. 653: The Physics of the Early Universe, ed. K. Tamvakis, 141–+

Schäfer, B. M. & Bartelmann, M. 2006, ArXiv Astrophysics e-prints

Schäfer, B. M., Pfrommer, C., Hell, R. M., & Bartelmann, M. 2006, MNRAS, 370, 1713

Schirmer, M., Erben, T., Schneider, P., et al. 2003, A&A, 407, 869

Schirmer, M., Erben, T., Schneider, P., Wolf, C., & Meisenheimer, K. 2004, A&A, 420, 75

Schneider, P. 1996, MNRAS, 283, 837

Schneider, P., Ehlers, J., & Falco, E. E. 1992, Gravitational Lenses (Gravitational Lenses, XIV, 560 pp. 112 figs.. Springer-Verlag Berlin Heidelberg New York. Also Astronomy and Astrophysics Library)

Schneider, P., Kochanek, C. S., & Wambsganss, J. 2006, Gravitational Lensing: Strong, Weak and Micro, ed. G. Meylan, P. Jetzer, P. North, P. Schneider, C. S. Kochanek, & J. Wambsganss

Schneider, P., van Waerbeke, L., Jain, B., & Kruse, G. 1998, MNRAS, 296, 873

Sefusatti, E., Vale, C., Kadota, K., & Frieman, J. 2007, ApJ, 658, 669

Shapiro, I. I. 1964, Physical Review Letters, 13, 789

Sheth, R. K., Mo, H. J., & Tormen, G. 2001, MNRAS, 323, 1

Sheth, R. K. & Tormen, G. 1999, MNRAS, 308, 119

Sheth, R. K. & Tormen, G. 2002, MNRAS, 329, 61

Silk, J. 1967, Nature, 215, 1155

Smith, R. E., Peacock, J. A., Jenkins, A., et al. 2003, MNRAS, 341, 1311

Spergel, D. N., Bean, R., Doré, O., et al. 2007, ApJS, 170, 377

Springel, V. 2005, MNRAS, 364, 1105

Springel, V. & Hernquist, L. 2003a, MNRAS, 339, 289

Springel, V. & Hernquist, L. 2003b, MNRAS, 339, 312

Steinhardt, P. J., Wang, L., & Zlatev, I. 1999, PhRvD, 59, 123504

Sugiyama, N. 1995, ApJS, 100, 281

Sunyaev, R. A. & Zeldovich, I. B. 1980a, ARA&A, 18, 537

Sunyaev, R. A. & Zeldovich, I. B. 1980b, MNRAS, 190, 413

Sunyaev, R. A. & Zeldovich, I. B. 1981, Astrophysics and Space Physics Reviews, 1, 1

Sunyaev, R. A. & Zeldovich, Y. B. 1972, Comments on Astrophysics and Space Physics, 4, 173

Tang, J. Y. & Fan, Z. H. 2005, ApJ, 635, 60

Tegmark, M., Strauss, M. A., Blanton, M. R., et al. 2004, PhRvD, 69, 103501

Tegmark, M. & Zaldarriaga, M. 2002, PhRvD, 66, 103508

Tornatore, L., Borgani, S., Matteucci, F., Recchi, S., & Tozzi, P. 2004, MNRAS, 349, L19

Udomprasert, P. S., Mason, B. S., Readhead, A. C. S., & Pearson, T. J. 2004, ApJ, 615, 63

Vale, C. & White, M. 2006, New Astronomy, 11, 207

Viana, P. T. P. & Liddle, A. R. 1996, MNRAS, 281, 323

Vikhlinin, A., Kravtsov, A., Forman, W., et al. 2006, ApJ, 640, 691

Vikhlinin, A., McNamara, B. R., Forman, W., et al. 1998, ApJ, 502, 558

Wambsganss, J. 1998, Living Reviews in Relativity, 1, 12

Wang, L. & Steinhardt, P. J. 1998, ApJ, 508, 483

Weller, J. & Battye, R. A. 2003, New Astronomy Review, 47, 775

Wetterich, C. 1988, Nuclear Physics B, 302, 668

Wetterich, C. 2002, Space Science Reviews, 100, 195

Wetterich, C. 2004, Physics Letters B, 594, 17

White, M. & Hu, W. 2000, ApJ, 537, 1

White, M. & Kochanek, C. S. 2002, ApJ, 574, 24

White, M., van Waerbeke, L., & Mackey, J. 2002, ApJ, 575, 640

White, S. D. M., Efstathiou, G., & Frenk, C. S. 1993, MNRAS, 262, 1023

Wright, C. O. & Brainerd, T. G. 2000, ApJ, 534, 34

Zel'dovich, Y. B. 1964, Soviet Astronomy, 8, 13

Zel'dovich, Y. B. 1970, A&A, 5, 84